

# Time-dependent search for neutrino emission from Mrk 421 and Mrk 501 observed by the HAWC gamma-ray observatory with the ANTARES data

Mukharbek Organokov

IPHC, Universite de Strasbourg

April 3, 2019

## Abstract

The principles of a search for high energy neutrino emission in coincidence with very high energy (VHE; 0.1-100 TeV) gamma-ray flares from two bright extragalactic sources detected by HAWC observatory, based on the data collected over 17 months between November 26<sup>th</sup>, 2014 and April 20<sup>th</sup>, 2016 by the ANTARES neutrino detector, are presented. The ANTARES telescope observes with high duty cycle an instantaneous field of view of  $> 2\pi$  sr with neutrinos coming also from above the horizon. An instrument like HAWC is capable of long-term and continuous monitoring of the source with nearly 100% duty cycle. Markarian 421 (Mrk 421) and Markarian 501 (Mrk 501) are the brightest and the closest BL Lac objects known. In contrast to other types of active galactic nuclei (AGN), BL Lacs are characterized by rapid and large-amplitude flux variability. Such radio-loud AGNs with collimated jets aligned to the line of sight are candidate sources of the observed high energy cosmic rays and of accompanying neutrinos and gamma rays produced in hadronic interactions with the surrounding medium.

# Contents

<b>1</b>	<b>Introduction</b>	<b>1</b>
<b>2</b>	<b>The Data set</b>	<b>2</b>
2.1	DATA/MC . . . . .	2
<b>3</b>	<b>Blazars</b>	<b>7</b>
3.1	Markarian LCs . . . . .	8
<b>4</b>	<b>ANTARES Visibility</b>	<b>11</b>
<b>5</b>	<b>Search method</b>	<b>13</b>
5.1	Test statistics . . . . .	14
5.2	Pseudo-experiments . . . . .	14
5.3	Systematics . . . . .	14
<b>6</b>	<b>Ingredients</b>	<b>16</b>
6.1	Gamma-ray derived neutrino spectra . . . . .	17
6.1.1	EBL attenuation correction . . . . .	17
6.2	Background time PDF . . . . .	19
<b>7</b>	<b>Flares selection</b>	<b>21</b>
<b>8</b>	<b>Analysis</b>	<b>24</b>
8.1	Discovery signal . . . . .	24
8.2	Acceptance . . . . .	28
8.3	Discovery fluxes . . . . .	30
8.4	MDP . . . . .	34
8.5	Sensitivity fluxes . . . . .	35
<b>9</b>	<b>Sensitivities</b>	<b>37</b>
<b>Conclusion Intermediate</b>		<b>42</b>
<b>10</b>	<b>Analysis updates: HAWC 2014-2017</b>	<b>43</b>
10.1	Bayesian Blocks . . . . .	43
10.2	Signal time PDF . . . . .	47
10.3	The new Data set . . . . .	49
10.3.1	DATA/MC . . . . .	50
10.4	Results . . . . .	54
10.4.1	Discovery signal . . . . .	54
10.4.2	Acceptance . . . . .	56
10.4.3	Discovery fluxes . . . . .	58
10.4.4	MDP . . . . .	62
10.4.5	Sensitivities . . . . .	64
<b>Conclusion Final</b>		<b>70</b>

<b>Appendix</b>	<b>71</b>
<b>A HAWC 2014-2016</b>	<b>71</b>
A.1 OFF days . . . . .	71
A.2 Figures for 3 sigma . . . . .	72
<b>B HAWC 2014-2017</b>	<b>76</b>
B.1 Skymap plots with selected events . . . . .	76
<b>List of Figures</b>	<b>80</b>
<b>List of Tables</b>	<b>81</b>
<b>References</b>	<b>82</b>

# 1 Introduction

This note presents the analysis on the search of spatial/temporal correlation between neutrinos detected by ANTARES and  $\gamma$ -ray emission from flares detected by HAWC [1] from Mrk 421 and Mrk 501. As the nearest blazars to Earth, both are excellent sources to test the blazar-neutrino connection scenario, especially during flares where time-dependent neutrino searches may have a higher detection probability [2].

The ANTARES data set selected for this analysis is described in section 2 and DATA/MC stability is discussed in section 2.1. Neutrino candidate sources and light curves are accounted in section 3. The ANTARES neutrino telescope visibility of the sources is reported in section 4. An unbinned likelihood-ratio maximization method is used for a search (see section 5). Ingredients of the likelihood used in the analysis are described in section 6. Spectra selected for the analysis are reported in section 6, 6.1: generic  $E^{-2.0}$ ,  $E^{-2.5}$  as well as  $E^{-1.0} \exp(-E/1\text{PeV})$  for both sources and  $\gamma$ -ray derived neutrino spectrum  $E^{-2.25}$  for Mrk 501.

The analysis results are released in section 8 and section 9. The final sensitivities are reported in section 9. The influence of the peaks selection definition to the discovery fluxes obtained in the analysis and corresponding sensitivities on fluxes and fluences is discussed in section 8.3 and section 9 respectively.

The intermediate conclusion for HAWC 2014-2016 is done in section 9.

The analysis updated results for extended period up to January 1<sup>st</sup>, 2018 is discussed in section 10. The Bayesian blocks procedure evolved in the HAWC 2014-2017 analysis is discussed in section 10.1, and the new flare states selected is shown in section 10.2. The new ANTARES data set selected for the HAWC 2014-2017 analysis is described in section 10.3 and the corresponding new DATA/MC comparison plots is presented in section 10.3.1. The new analysis results are released in section 10.4 and the new sensitivities is discussed in 10.4.5. The additional skymaps for the selected track-like events w.r.t. different selection cuts can be found in Appendix B.1.

The final conclusion is discussed in section 10.4.5.

## 2 The Data set

The data set covers the period from the November 26<sup>th</sup>, 2014 and April 20<sup>th</sup>, 2016 (MJD: 56988-57497) leading to effective detector livetime (LT) of 503.7 days (1.379 years), covering the same period of observation as HAWC. The search relies on track-like event signatures, so only CC interactions of muon neutrinos are considered.

The DATA and Monte Carlo (MC) files were obtained from the following folders:

- Period [2014][2015]

The DATA files:

- /sps/km3net/users/antprod/data/Reprocessing\_2016\_05 [SPS]

The MC files:

- $\nu$  : /sps/km3net/users/antprod/mc/rbr\_v3\_QE/complete [SPS]
- $\mu$  : /sps/km3net/users/antprod/mc/rbr\_v3\_QE/complete [SPS]

- Period [2016]

The DATA files:

- /in2p3.fr/group/antares/SeaTray/prod\_2017-04-03/Line12/sea/2016/12 [HPSS]

The MC files:

- $\nu$  : /in2p3.fr/group/antares/mc/rbr/v4/reco/AntDST [HPSS]
- $\mu$  : /in2p3.fr/group/antares/mc/rbr/v4/reco/mu\_v3/AntDST [HPSS]

Runs are selected if the conditions below are fulfilled

- QualityBasic  $\geq 1$
- SCAN  $\neq 1$
- Sparking  $\neq 1$  (Additional sparking runs were observed and removed)

The MC production is selected to be complete, i.e. MUPAGE and all track-like (a)numu files were available. Besides, since not all DATA runs have a corresponding MC runs and MC complete runs give livetime of 332.8 days (0.911 years), rescaling of incomplete MC is required. Thus, rescale of available MC livetime up to livetime in DATA is applied. It is considered as an additional weight on the MC in order to take into account the livetime difference and done on a year-to-year basis  $\frac{LT_{year}^{DATA}}{LT_{year}^{MC}}$ .

The 2007-2015 data from Reprocessing\_2016\_05 inherently has a pre-selection cuts as a data reprocessed of old 2007-2015 data productions in order to include the TANTRA reconstruction, but 2016 year not. Therefore, since the analysis was started with this data set, but only track is used, then in order to unify 2014-2015 and 2016 years, the global cuts  $\Lambda > -6.0$  and  $\beta < 1.5$  and  $\cos(\theta) > -0.2$  applied on the whole period 2014-2016.

### 2.1 DATA/MC

In order to test the goodness of the ANTARES MC production for the period of the analysis, it is compared with measured data. The DATA/MC comparison plots for the energy estimator  $n_{hit}$  and for the  $\Lambda$ ,  $\cos(\theta)$ ,  $\beta$  cuts with non-normalized distributions and with indicated MC contributions (up-going atmospheric neutrinos and mis-reconstructed atmospheric muons) can be seen in Fig. 1- 4.

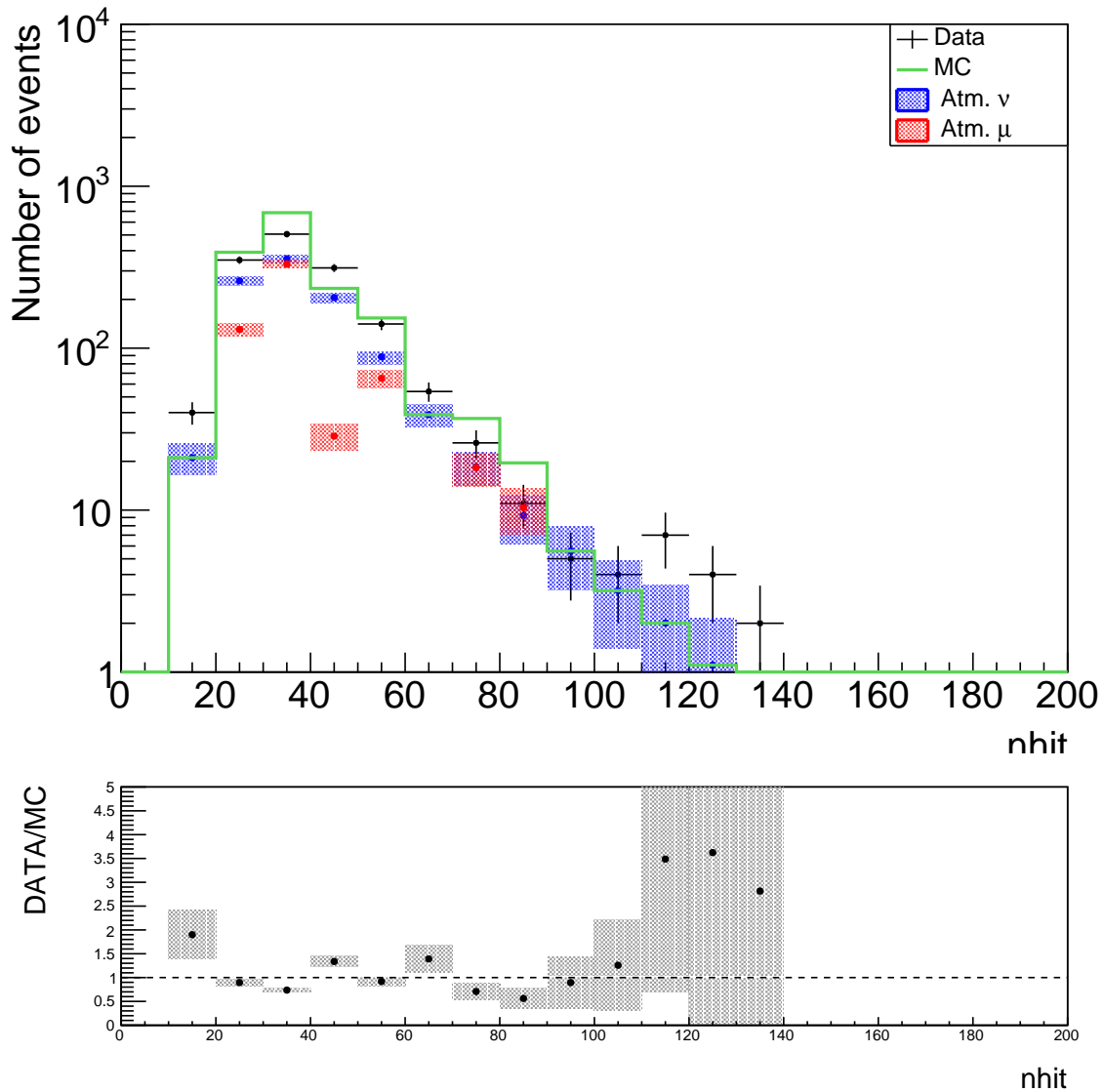


Figure 1: Comparison of the data with MC simulations as a function of the number of hits  $nhit$ . The figure corresponds to the energy PDF distribution after applying a cut on the quality parameter  $\Lambda > -5.3$  (the global cuts on  $\beta < 1.0^\circ$ , and  $\cos(\theta) > -0.1$  applied). The blue dots show the simulated up-going atmospheric neutrinos with the errors as a dashed area, the red dots show the mis-reconstructed atmospheric muons with the errors as a dashed area, the green line is the sum of both contributions, and the black crosses show the data. The bottom plot shows the data to MC ratio, where the number of MC events is the sum of neutrinos and atmospheric muons.

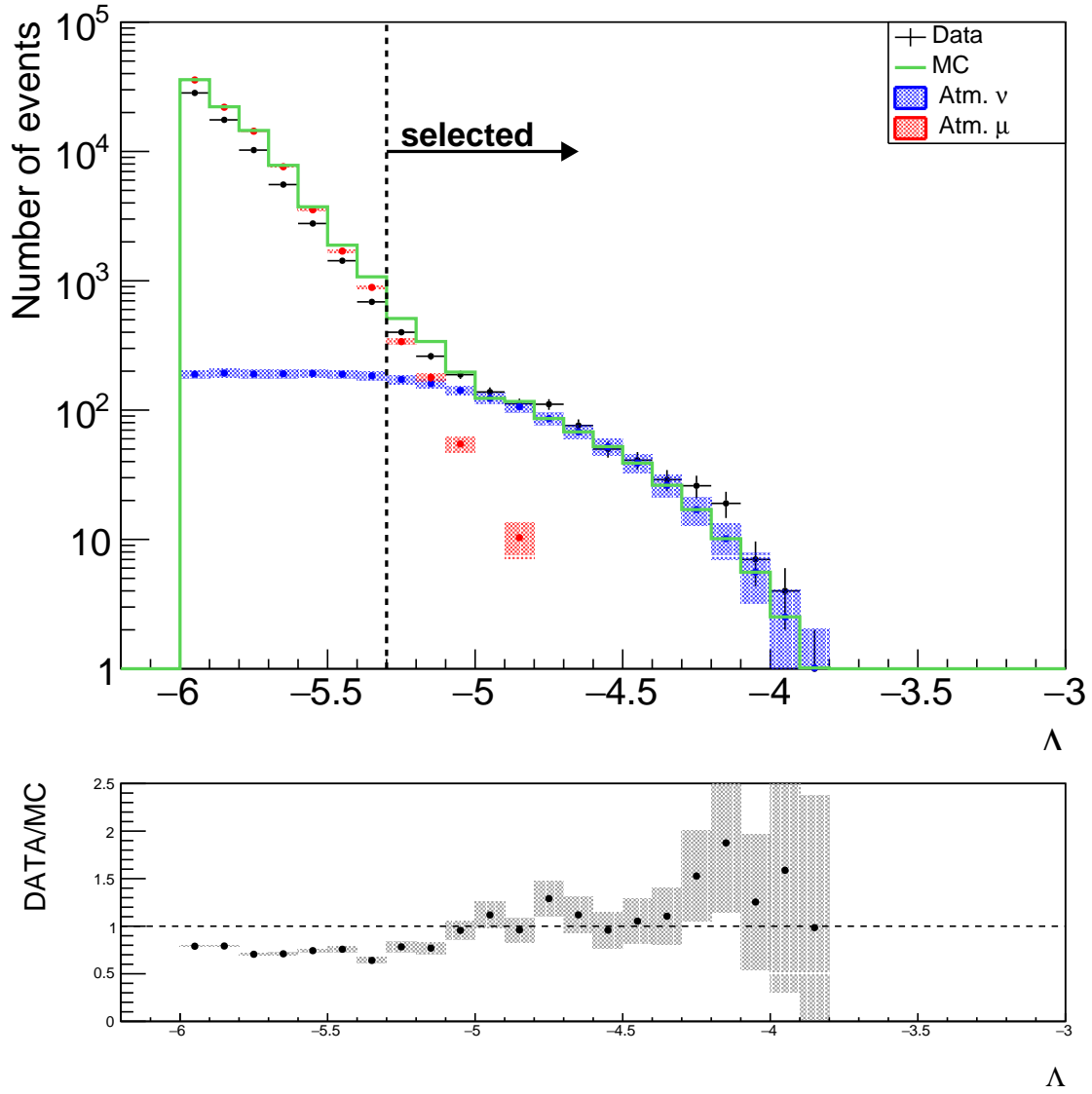


Figure 2: Comparison of the data with MC simulations as a function of the quality parameter of the reconstruction of muon track  $\Lambda$ . The figure corresponds to the event distribution after applying the global cuts on  $\beta < 1.0^\circ$ ,  $\cos(\theta) > -0.1$ , and  $\Lambda > -6.0$ . The blue dots show the simulated up-going atmospheric neutrinos with the errors as a dashed area, the red dots show the mis-reconstructed atmospheric muons with the errors as a dashed are, the green line is the sum of both contributions, and the black crosses show the data. The vertical dotted line with the arrow shows where the optimized selection cuts stand for the various tested spectra of both sources. The bottom plot shows the data to MC ratio, where the number of MC events is the sum of neutrinos and atmospheric muons.

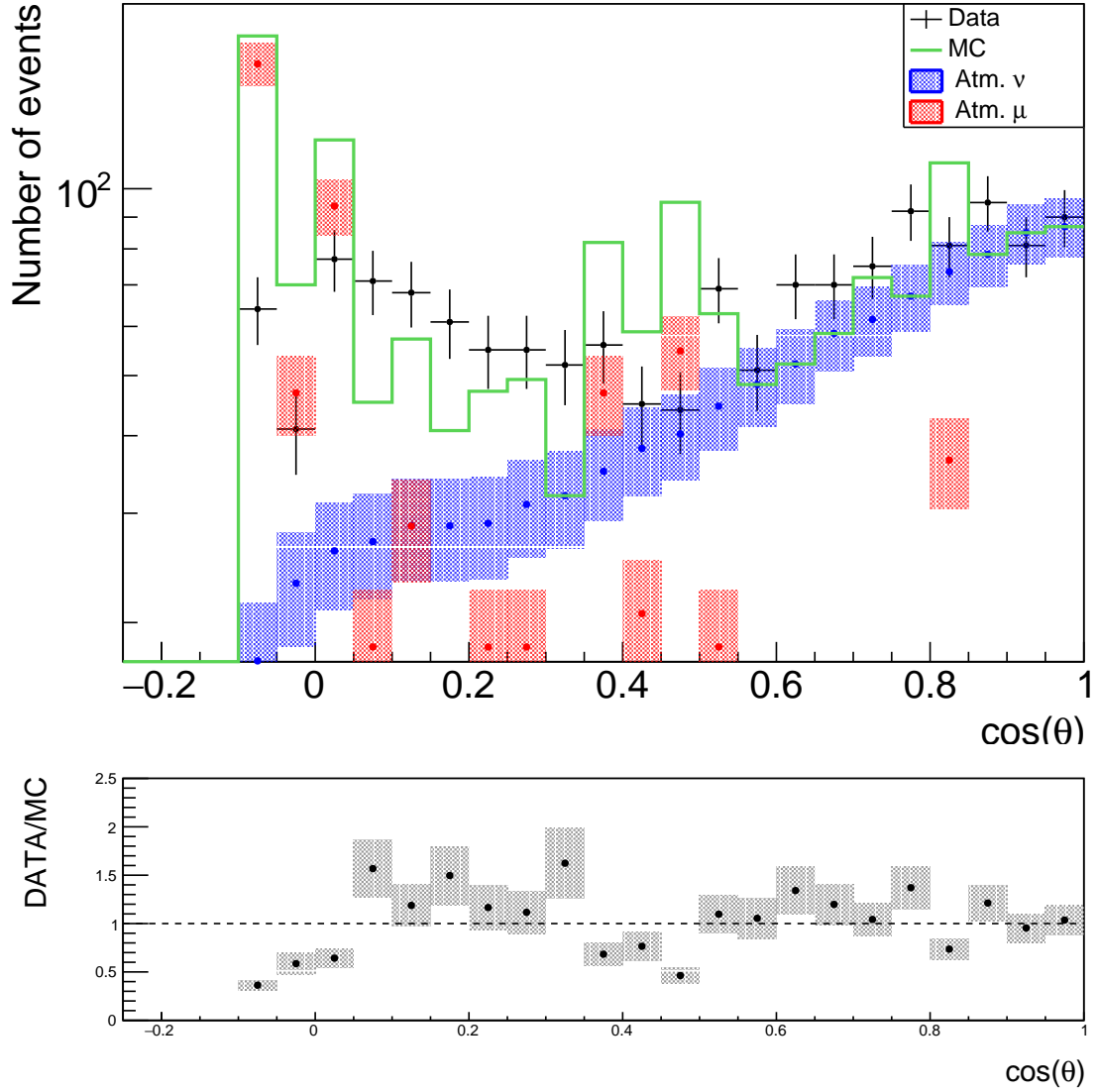


Figure 3: Comparison of the data with MC simulations as a function of the reconstructed cosine of the zenith angle  $\cos(\theta)$ . The figure corresponds to the event distribution after applying a cut on the quality parameter  $\Lambda > -5.3$  (the global cuts on  $\beta < 1.0^\circ$ , and  $\cos(\theta) > -0.1$  applied). The blue dots show the simulated up-going atmospheric neutrinos with the errors as a dashed area, the red dots show the mis-reconstructed atmospheric muons with the errors as a dashed area, the green line is the sum of both contributions, and the black crosses show the data. The bottom plot shows the data to MC ratio, where the number of MC events is the sum of neutrinos and atmospheric muons.

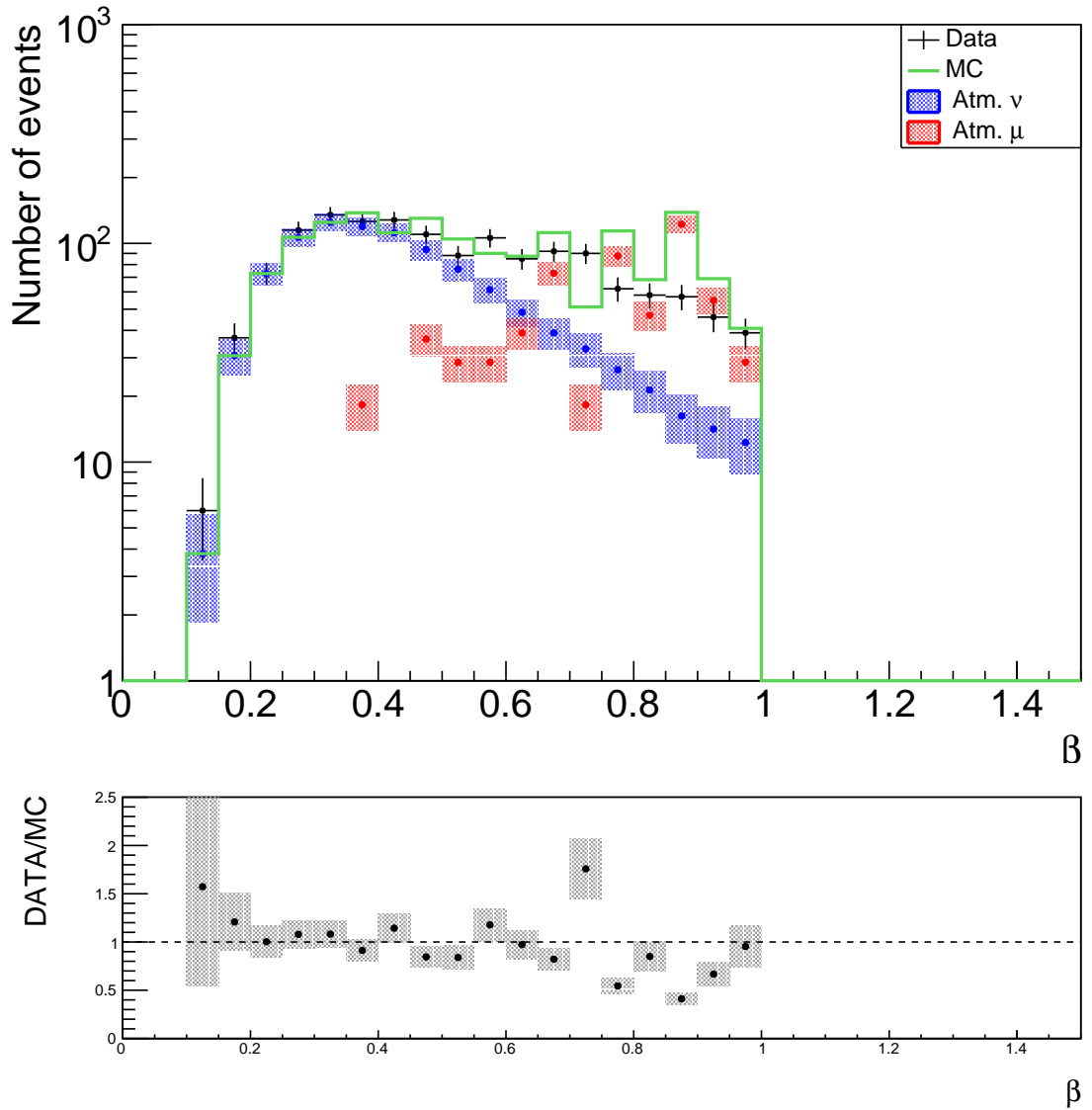


Figure 4: Comparison of the data with MC simulations as a function of the estimated error on the direction of the reconstructed muon track  $\beta$ . The figure corresponds to the event distribution after applying a cut on zenith angle  $\cos(\theta) > -0.1$  and a cut on the quality parameter  $\Lambda > -5.3$  (the global cut on  $\beta < 1.0^\circ$  applied). The blue dots show the simulated up-going atmospheric neutrinos with the errors as a dashed area, the red dots show the mis-reconstructed atmospheric muons with the errors as a dashed area, the green line is the sum of both contributions, and the black crosses show the data. The bottom plot shows the data to MC ratio, where the number of MC events is the sum of neutrinos and atmospheric muons.

### 3 Blazars

Mrk 421 and Mrk 501 are the brightest and closest BL Lac objects known, at luminosity distances  $d_L = 134$  Mpc with redshift  $z = 0.031$  and  $d_L = 143$  Mpc with redshift  $z=0.033$  respectively. Both are classified as high-peaked BL Lac objects (HBL) (see Fig. 5). Mrk 421 is known to exhibit a high degree of variability in its emission and yearly average fluxes are known to vary between a few tenths and  $\sim 1.9$  times the flux of the Crab Nebula. Variability of Mrk 421 has been observed down to time scales of hours or less and its spectral shape known to vary with its brightness <sup>1</sup>. Various studies of Mrk 501 at TeV energies have shown different features of low flux states emission and extreme outbursts [1].

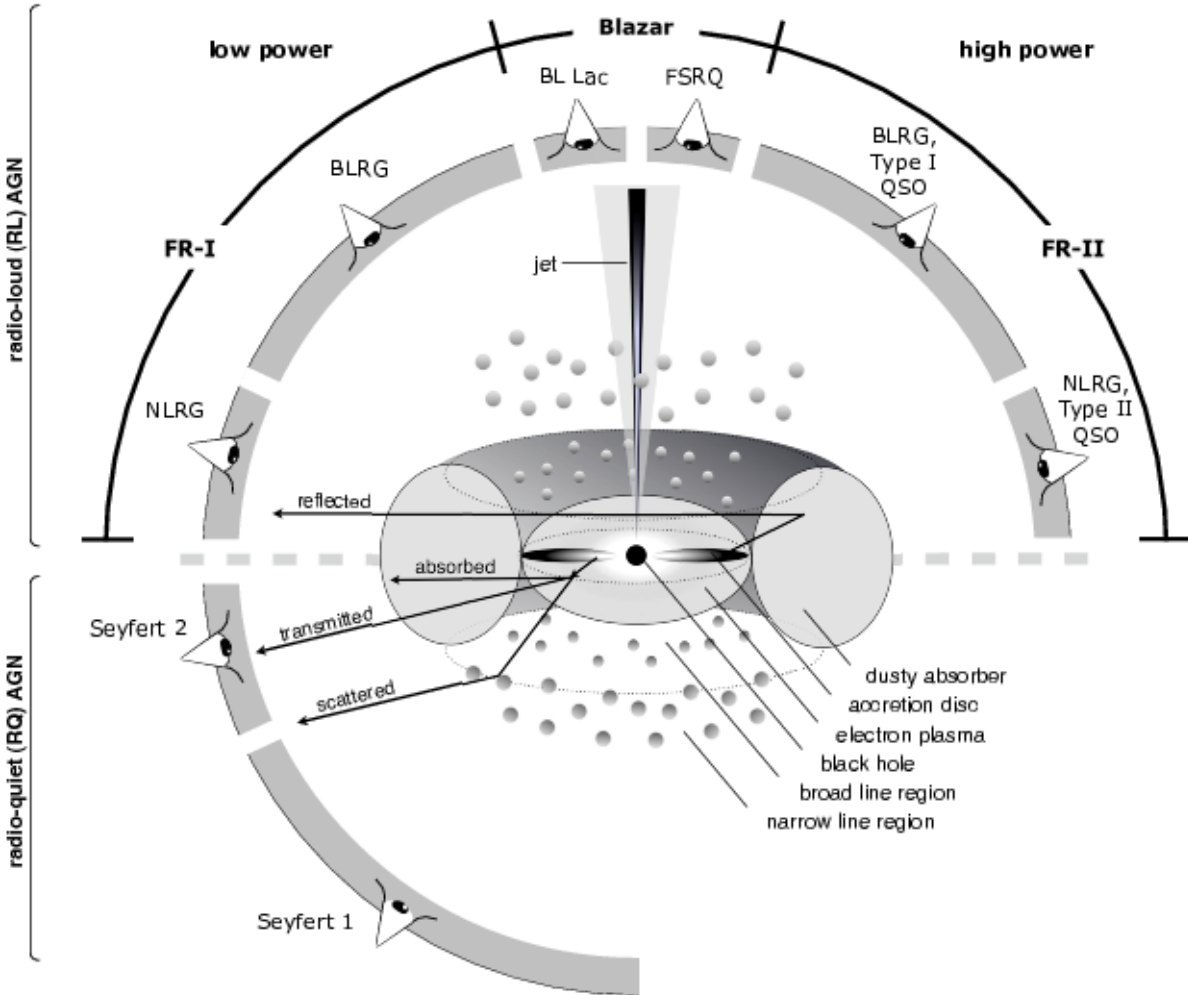


Figure 5: Schematic representation of our understanding of the AGN phenomenon in the unified scheme. The type of object we see depends on the viewing angle, whether or not the AGN produces a significant jet emission, and how powerful the central engine is. Note that radio loud objects are generally thought to display symmetric jet emission [3].

<sup>1</sup>Not taken into account in the analysis.

### 3.1 Markarian LCs

The HAWC Observatory is located at an elevation of 4,100 m above sea level on the flanks of the Sierra Negra volcano in the state of Puebla, Mexico. The installation began in February 2012 and HAWC-300 is fully operational since March 20, 2015. The design of HAWC is optimized for the detection of air showers induced by  $\gamma$ -rays in 0.1-100 TeV. With field of view  $\sim 2$  sr HAWC can monitor any source over 2/3 of the sky for up to 6 hours per day and is most sensitive to sources between declinations  $-26^\circ$  and  $+64^\circ$  [1]. Such capabilities make TeV light curve data available for studying flaring behavior of blazars.

HAWC has made clear detections of Mrk 421 and Mrk 501. In this analysis HAWC-300 data of first long-term TeV light curve studies are used, collected over 17 months between November 26<sup>th</sup>, 2014 and April 20<sup>th</sup>, 2016 [1].

The main characteristics of the  $\gamma$ -ray flux for the two sources are summarized in Table 1.

Table 1: Some parameters from [1]

	Mrk 421	Mrk 501
Highest daily flux*	$26.94 \pm 3.7$	$16.7 \pm 2.3$
Average flux*	$4.53 \pm 0.14$	$1.74 \pm 0.08$
$\Gamma^{**}$	$2.21 \pm 0.14_{\text{stat}} \pm 0.20_{\text{sys}}$	$1.60 \pm 0.30_{\text{stat}} \pm 0.20_{\text{sys}}$
$E_{\text{cut}}^{**}$	$E_0 = 5.4 \pm 1.1_{\text{stat}} \pm 1.0_{\text{sys}}$	$E_0 = 5.7 \pm 1.6_{\text{stat}} \pm 1.0_{\text{sys}}$

\* [ ] =  $10^{-12} \text{ ph cm}^{-2} \text{ s}^{-1}$ ; fluxes calculated above 2 TeV for Mrk 421 and above 3 TeV for Mrk 501.

\*\* Spectral index and exponential cut-off, derived from spectral fit.

The precise shape of the signal time PDF can be extracted directly for the  $\gamma$ -ray light curve assuming the proportionality between the  $\gamma$ -ray and the neutrino fluxes. If a light curve is variable, the Bayesian blocks algorithm can be used to find an optimal data segmentation into regions that are well represented by a constant flux, within the statistical uncertainties. Bayesian blocks algorithm is used to identify distinct flux states and the results are presented in [1]. Both Mrk 421 and Mrk 501 show clear variability on time scales of one day. The 1-day binning is applied to the final distinct fluxes from [1] (see Fig. 6) and used in the analysis as a signal time PDF. The signal time PDF is assumed to have a square shape.

Taking advantage of  $\gamma$ -ray flux variation time information from potential neutrino emitters as in Fig. 6, significantly reduce the v background and improve the signal-to-noise discrimination.

As discussed in Sec. 2 in this analysis for each day the DATA runs are available and the whole flaring period is fully covered by quality DATA runs with no sparking. The importance of the MC rescale can be seen in Fig. 7, where shaded red area represent fully OFF days in the case if only DATA-MC complete runs considered (the list of fully OFF days is collected in Table. 11 in Appendix A.1). Obviously, significant amount of time would be excluded from the analysis and some substantial high peaks would be not considered due to OFF days. Such situation leads to null probability in the time distribution of DATA events  $P_b(t)$  used in the pseudo-experiments to simulate time of the events. This, in turn, able to decrease neutrino discovery potential vastly.

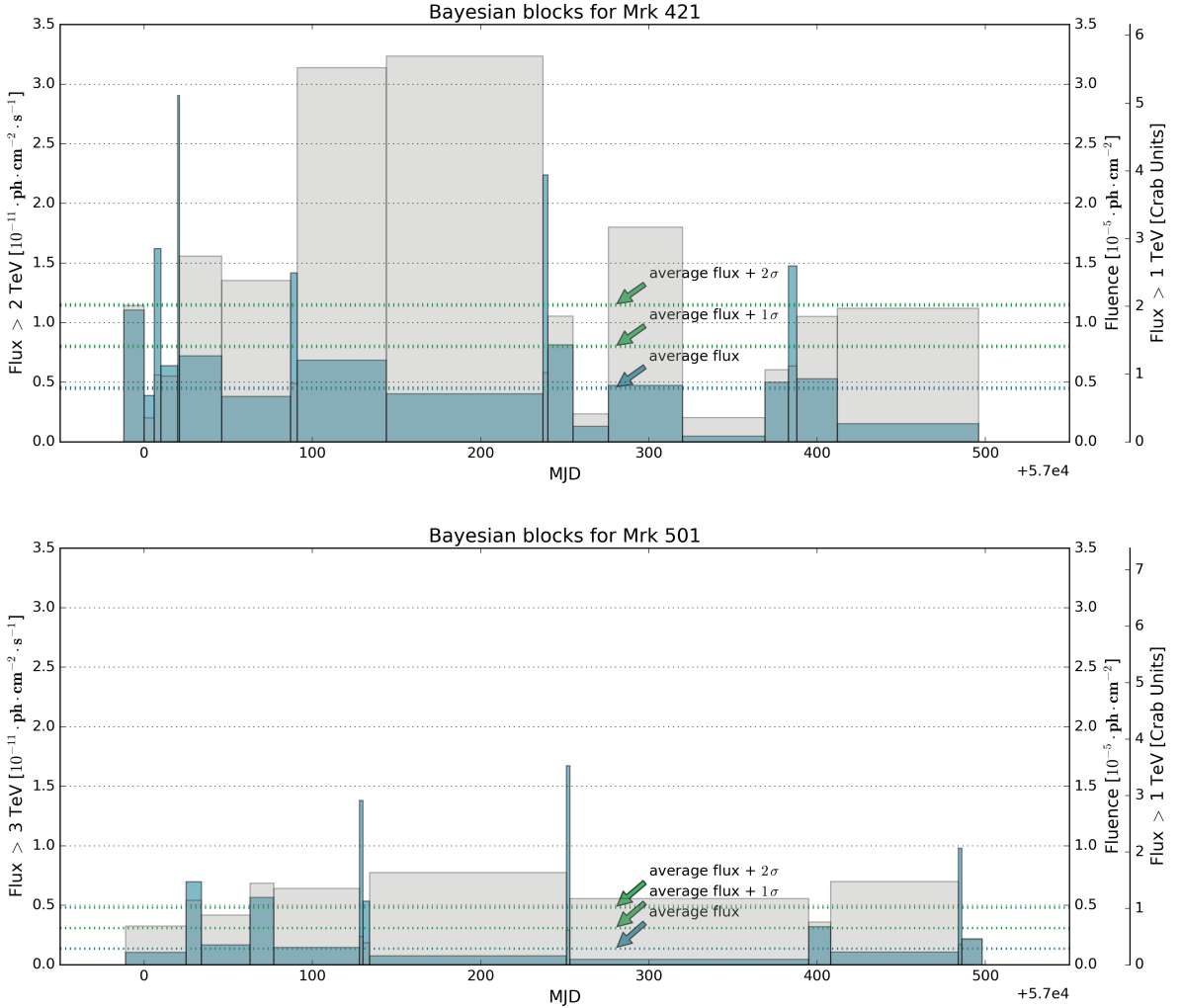


Figure 6: The distinct flare states for Mrk 421 (top) and Mrk 501 (bottom) for 17 months after 1-day binning applied to the light curve data from [1] (in blue and green); the blue dotted lines represent the average fluxes,  $\sim 0.8$  CU and  $\sim 0.3$  CU respectively; the green dotted lines represent the peaks selection criteria can be applied: *average flux*, *average flux + 1 $\sigma$* , *average flux + 2 $\sigma$* . The left axes represent the units of the fluxes, the right-right axis represent the fluxes in corresponding Crab Units (CU). The right-left axes represent the units of fluences shown as shaded grey areas.

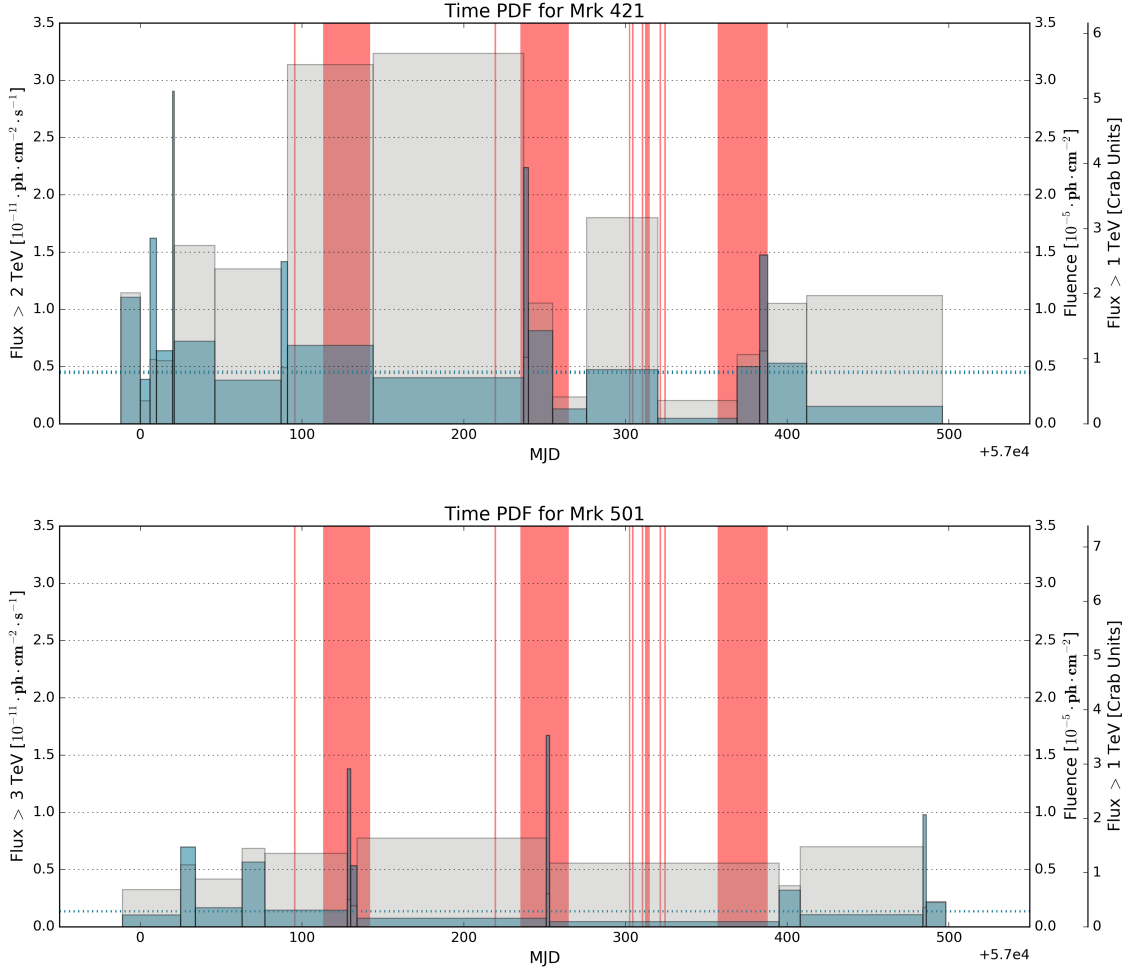


Figure 7: The distinct flare states for Mrk 421 (top) and Mrk 501 (bottom) for 17 months after 1-day binning applied to the light curve data from [1]. The shaded red area represent OFF days. The left axes represent the units of the fluxes, the right-right axis represent the fluxes in corresponding Crab Units (CU). The right-left axes represent the units of fluences shown as shaded grey areas.

## 4 ANTARES Visibility

The ANTARES neutrino telescope is located at a latitude of  $42^{\circ}48\text{N}$  latitude and can monitor with only up-going events a wide range of the sky,  $\delta \in [-90^{\circ}, +42.8^{\circ}]$ . Due to the fact that Mrk 421 and Mrk 501 are located at the edge of ANTARES visibility (see Fig. 8, 9), a small amount of down-going events close to the horizon can be accepted to gain  $\sim 15\%$  in visibility (see Table 2). The ANTARES visibility is a fraction of time that the source is visible by ANTARES due to its declination  $\delta$  and selected event cuts. In this analysis events with maximum  $\cos(\theta) > -0.1$  are selected and the optimization will be done with this cut on the reconstructed zenith. Because of expectation that gain in discovery flux is commensurate with increase of visibility w.r.t.  $\cos(\theta)$ , the possible extension up to  $\cos(\theta) > -0.5$  (see Figure. 9) added to estimate the capacity of gain in discovery flux whether  $\cos(\theta) > -0.3$  (grey dotted line),  $\cos(\theta) > -0.4$  (grey dashed line), or  $\cos(\theta) > -0.5$  (grey solid line) applied. Proper cut on zenith angle is essential to limit the contribution from mis-reconstructed atmospheric muons. But due to observed improvement in discovery flux w.r.t. increase in visibility (with the maximum cut on zenith angle  $\cos(\theta) > -0.1$  currently applied and giving better discovery flux), it can be assumed a chance to enhance the discovery flux via application of cut on zenith angle above  $\cos(\theta) > -0.1$ .

Table 2: Visibility and Ratio

$(\delta, \text{RA})$	$V.^{\text{up}}$	$> -0.1$	$> -0.2$	$> -0.3$	$> -0.4$	$> -0.5$
Mrk 421 (38.2,166.1)	24.0	31.5(1.31)	37.7(1.57)	43.6(1.81)	49.0(2.05)	54.5(2.28)
Mrk 501 (39.8,253.5)	21.9	29.7(1.36)	36.2(1.65)	42.2(1.93)	48.2(2.20)	53.8(2.46)

\* Visibility in %.

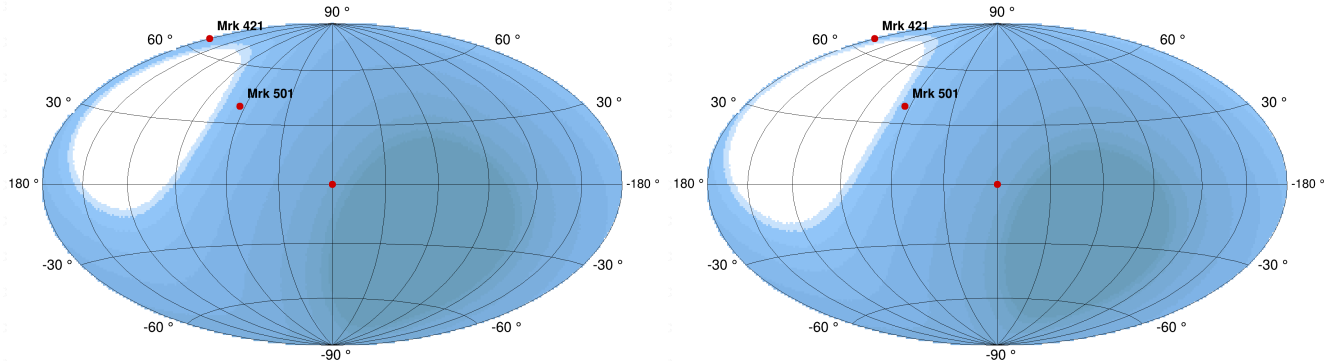


Figure 8: ANTARES visibility of the sky ranging from 0 (white) to 100% (dark blue) with 10% step. *Left panel:* Up-going with slightly down-going (angle above the horizon below  $5.74^{\circ}$ ) for  $\cos(\theta) > -0.1$ ; *Right panel:* Only Up-going  $\cos(\theta) > 0$ .

The elevation for the sources is shown in Fig. 10. As seen from the Fig. 10, e.g., the Mrk 421 is below the horizon for only  $\sim 6$  hours per day ( $\sim 24\%$  as from the  $V.^{\text{up}}$  in Table. 2). For  $\cos(\theta) > -0.1$  and  $\cos(\theta) > -0.2$  it gives roughly  $\sim 2\text{h}$  and  $\sim 3.5\text{h}$  gain respectively in addition to  $\sim 6\text{h}$  ( $\sim 31\%$  and  $\sim 57\%$  respectively as from the ratios in Table. 2).

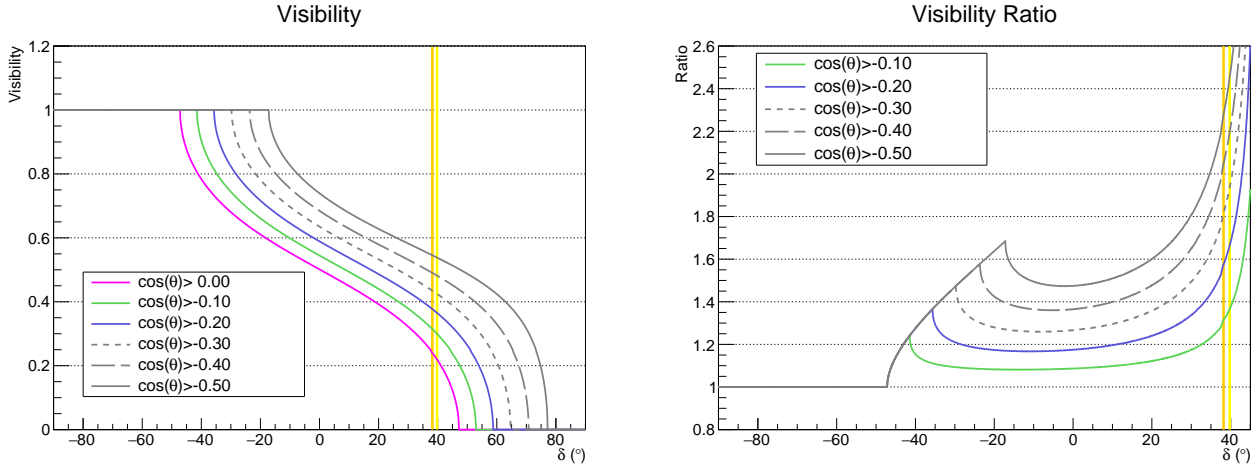


Figure 9: *Upper panel:* Visibility curves as a function of the declination for cuts on zenith angle used in the analysis  $\cos(\theta) > 0.0$ ,  $\cos(\theta) > -0.1$ ,  $\cos(\theta) > -0.2$  (colored solid lines) and for possible extension up to  $\cos(\theta) > -0.5$  (grey color dotted, dashed and solid lines respectively). *Lower panel:* Visibility ratio curves as a function of the declination with respect to  $\cos(\theta) > 0.0$ . The vertical color lines represent the declination of Mrk 421 (orange) and Mrk 501 (yellow).

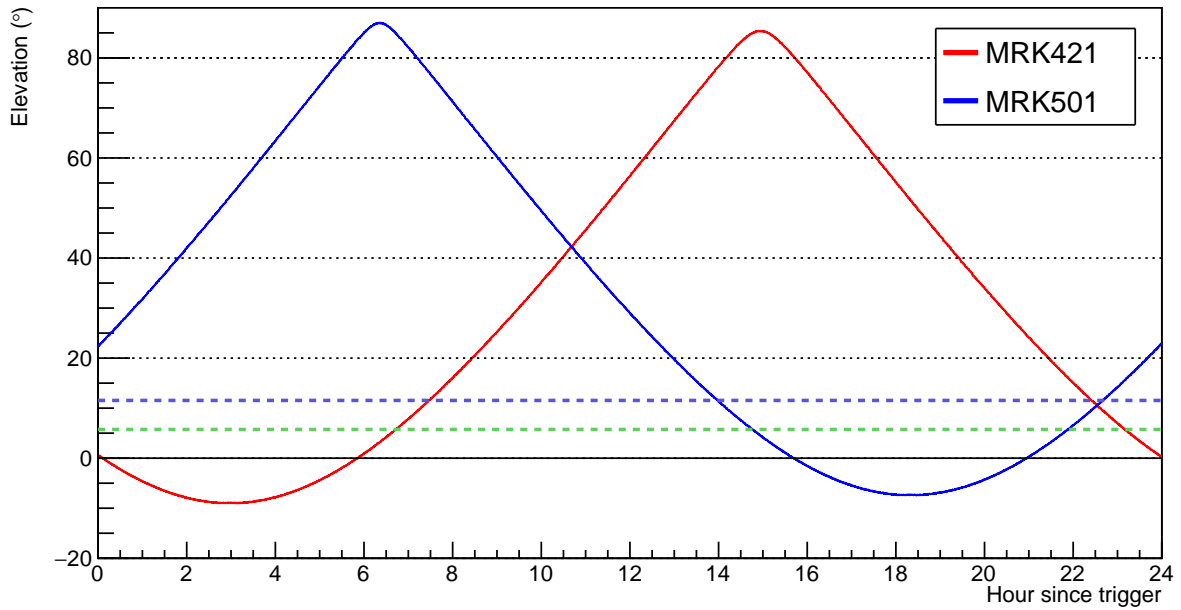


Figure 10: Elevation of the sources (in degrees). The green and blue dotted lines represent the improvement in the visibility for the  $\cos(\theta) > -0.1$  and  $\cos(\theta) > -0.2$  cuts and corresponds to  $5.74^\circ$  and  $11.54^\circ$  elevation levels respectively.

## 5 Search method

An unbinned likelihood-ratio maximization method [4,5] is used for a search. The ANTARES data sample is parametrized as two-component mixture of signal and background and the goal of the method is to determine in a given direction in the sky and at a given time the relative contribution of signal and background. The signal is expected to be small so that the full data direction can be used as an estimation of background.

The likelihood  $L$  is:

$$\ln(L) = \left( \sum_{i=1}^N \ln[N_S S_i + N_B B_i] \right) - [N_S + N_B] \quad (1)$$

The background rate  $N_B$  is known a priori when building the likelihood.  $S_i$  and  $B_i$  are defined as the probability density functions (PDF) respectively for signal and background for an event  $i$ , at time  $t_i$ , energy, declination  $\delta_i$ ; hence, the final likelihood with all terms:

$$\ln(L) = \left( \sum_{i=1}^N \ln[N_S \cdot P_s(\alpha_i) \cdot P_s(E) \cdot P_s(t) + N_B \cdot P_b(\sin(\delta_i)) \cdot P_b(E) \cdot P_b(t)] \right) - [N_S + N_B] \quad (2)$$

Here,

- Directional PDFs:  $P_s(\alpha_i)$  for signal and  $P_b(\delta_i)$  for background, the parameter  $\alpha_i$  represents the angular distance between the direction of the event  $i$  and direction to the source  $\delta_i$ ;
- Energy PDFs:  $P_s(E)$  and  $P_b(E)$ ; Various energy estimators have been developed in ANTARES: nhit, dE/dX, ANN. The simplest one is the total number of hits in the PMTs selected by the track reconstruction, which is expected to be proportional to the incident particle energy. Neutrinos generated in the atmosphere have a much softer energy spectrum ( $\propto E^{-3.7}$ ) than neutrinos from the expected astrophysical flux (for example,  $\propto E^{-2.0}$ ). Hence, the energy estimator information is used in the likelihood to further distinguish between cosmic signal and atmospheric background. The Nhits energy estimator is selected for the current analysis (see Fig. 1).
- Time PDFs:  $P_s(t)$  for signal and  $P_b(t)$  for background. The LCs for each source derived from HAWC (see Fig. 6) show the periods of interest for the coincident neutrino search and used as a time PDFs. The background time PDF  $P_b(t)$  is the probability to have a background event at a given time. It is built using the distribution in time of ANTARES events with following criteria:  $\Lambda > -5.6$ , number of hits in PMTs  $n_{\text{hit}} > 5$  in more than one line  $n_{\text{line}} > 1$ , and an estimated angular uncertainty on the fitted muon track direction  $\beta < 1.0^\circ$ .

The ingredients are determined using the ANTARES Monte Carlo simulations and data (see section 2). The background PDFs are all computed using data only. The shape of the time PDF for the signal event is extracted directly from the  $\gamma$ -ray light curve assuming a proportionality between the  $\gamma$ -ray and the neutrino fluxes.

The neutrinos produced by a given flare may not reach the Earth at the same time as the associated  $\gamma$ -rays. No possible lag between  $\gamma$ -ray and the neutrino is considered in the likelihood in order to take into account a possible arrival time difference of  $\gamma$ -ray and the neutrino signals. For example, the  $\pm 5$  days lag considered in [4,5] is much larger than the theoretical estimation in [6] and was introduced to only not miss a neutrino signal for the shortest flares if the assumption of the simultaneous arrival of the  $\gamma$ -ray and the neutrino signals is off by one day, and in that case to allow a small lags in the proportionality which corresponds to a possible shift of the entire time PDF. Due to the fact, that the duration of the flares used

in the current analysis much longer than one day, and the theoretical estimation in [6] gives the arrival time difference between  $\gamma$ -ray and the neutrino much less than one day, it is considered for the lag to be set to zero.

The energy PDF for the signal event is produced according to the studied energy spectrum. The angular distance to the source is characterized by the Point Spread Function (PSF)  $P_s(\alpha_i)$  defined as the probability density of  $\alpha$  per unit solid angle  $\Omega$ .

## 5.1 Test statistics

The maximum likelihood method takes as best-fit values of the unknown parameter  $N_s$  the values that maximize the likelihood function. The maximization of the likelihood function  $L$  is performed with MINUIT minimization software [7] (ROOT class TMinuit) via search of minimum in  $-2\ln(L)$  using MIGRAD algorithm.

The goal of the unbinned search is to determine, for a given direction in the sky and at a given time, the relative contribution of background and signal components, and to calculate the probability to have a signal above a given background model.

Finally, to calculate goodness of fit between two models,  $H_0$  and  $H_1$ , and to differentiate hypotheses, we build a test statistic (TS) equivalent to a likelihood ratio:

$$TS = 2(\ln(L_{s+b}^{\max}) - \ln(L_b)) \quad (3)$$

Test statistic represents the logarithm of the ratio between the source-model likelihood  $L_{s+b}^{\max}$  maximized w.r.t.  $N_s$  over the likelihood  $L_b$  calculated in the background-only hypothesis assuming  $N_s = 0$ . Test statistic Q is a ratio of the probability for background plus signal hypothesis  $H_1$  over the probability of background-only hypothesis  $H_0$  (see Fig. 11).

The significance of a measurement is determined by its p-value, which is given by the probability to yield TS equal or higher than TS observed if the background-only hypothesis were true. The p-value determines how "likely" or "unlikely" the data with the true background-only  $H_0$  hypothesis.

## 5.2 Pseudo-experiments

To have the TS pseudo-experiments (PEX) were generated simulating background and signal in a  $30^\circ$  cone around the considered source according to background and signal hypothesis.  $3 \times 10^5$  PEX are produced for background hypothesis and  $3 \times 10^4$  PEX for signal hypotheses from 1 up to 20 possible signals. Then the signal distributions  $H_1(Q)$  is derived and test statistics Q-values for each hypotheses are evaluated. The discovery potentials for  $3\sigma$  and  $5\sigma$  discoveries as the average number of signal events required to achieve a p-value lower than  $2.7 \cdot 10^{-3}$  and  $5.7 \cdot 10^{-7}$  respectively are computed later.

## 5.3 Systematics

The possible systematics intrinsically inherent to the detector is considered. The systematics on the absolute pointing accuracy, angular resolution and the energy resolution is applied as a correction over the simulated parameter that is obtained from a Gaussian distribution with that uncertainty as a standard deviation. Since the events are simulated in equatorial coordinates ( $\delta, RA$ ), the systematic uncertainty in local coordinates ( $\theta, \phi$ ) is considered in the PEX by determining an elevation  $\theta$  and azimuth  $\phi$  for that source in the moment of the day at which the event was simulated.

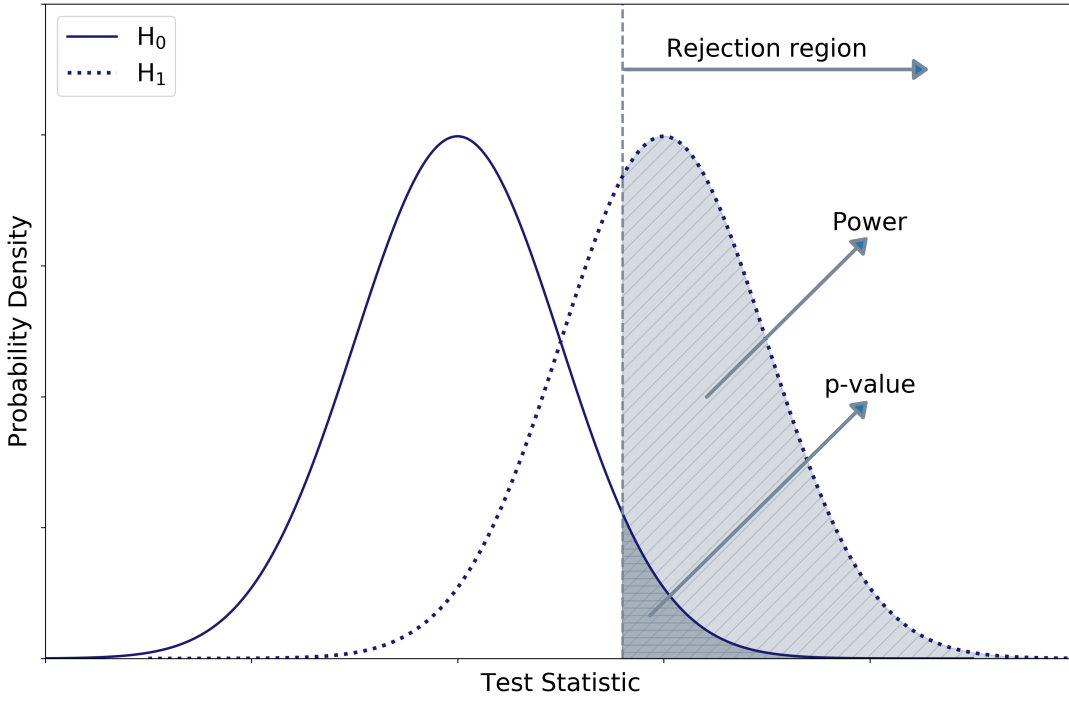


Figure 11: Definition of the power and p-value significance of the test statistic. The distributions of the test statistic, TS, for the background-only ( $H_0$ ) and signal plus background ( $H_1$ ) hypotheses are shown. The test statistic required for  $H_0$  rejection is shown as a dotted line. Corresponding p-value significance and the power to discriminate  $H_0$  from  $H_1$  are shown as a dark-shaded and light-shaded areas respectively.

- Absolute pointing accuracy uncertainty in the local coordinates established in [8]: uncertainty of  $0.13^\circ$  and  $0.06^\circ$  on the horizontal ( $\phi$ ) and vertical ( $\theta$ ) directions, respectively. This corresponds to 0.0023 and 0.0011 in radians and set in the PEX simulation.
- Angular resolution uncertainty: 15% degradation on the angular resolution in the track channel is considered. The accuracy of the detected hit times can directly impact on the angular resolution of the track reconstruction algorithm [9]. A smearing of the hit times was performed in simulations by varying the hit time resolution leading to a 15% degradation on the angular resolution in the track channel [10]. Many possible effects can contribute to this resolution, including the PMT transit time spread, mis-calibrations of the timing system and possible spatial misalignments of the detector [10].
- Energy resolution uncertainty: 10% on the number of hits  $nhit$ . Same systematic uncertainty but in  $dE/dX$  energy estimator is used in [4].

Occasionally, the systematics simulations can produce a meaningless value for an event parameter: an undetectable declination due to the elevation cut or an energy estimator with null probability in some of the PDFs used in the likelihood. In that case, it is rejected and the event is simulated again.

## 6 Ingredients

The muon track reconstruction returns two quality parameters, namely the track-fit quality parameter,  $\Lambda$ , and the estimated angular uncertainty on the fitted muon track direction,  $\beta$ . Cuts on these parameters are used to improve the signal-to-noise ratio.

- The  $\beta < 1.0$  only is selected contrary to  $\beta < 1.0$  as from the global cut, this ensure a rather good directional reconstruction of the selected  $\nu$  candidates as well as enough statistics for the analysis with this cut. Given the correlation between  $\beta$  and  $\Lambda$ , the more constraining cut on beta is obtained by choosing a cut on  $\Lambda$ .
- The 9  $\Lambda$  parameters in the range [-5.8;-5.0] with step=0.1 considered for the analysis and  $\Lambda$  will be optimized source by source for spectra considered. This range is sufficient out of the full range of 13  $\Lambda$  [-6.0;-4.8] could be taken into account because of the fact the vastly decreasing discovery fluxes outside of defined 9  $\Lambda$  range and evidence of more stability of background time PDF (see Sec. 6.2) in this range.
- The analysis is performed for the one cut on the reconstructed zenith  $\cos(\theta)$ :  $\cos(\theta) > -0.1$  (a bit down-going events accepted as it gives increase in solid angle and also increase of visibility for each source, see Sec. 4). The  $\cos(\theta) > 0.0$  cut with only up-going events are not considered as it gives worse discovery fluxes. As mentioned in Sec. 2, the  $\cos(\theta) > -0.2$  cut is not taken into account due to no stability in the ratio between DATA and MC.
- The spectra used in the analysis: a generic power-law  $E^{-\gamma}$  with  $\gamma = -2.0$  and  $\gamma = -2.5$  covering most astrophysical models as well as power-law  $E^{-\gamma}$  with  $\gamma = -1.0$  and exponential cutoff at 1 PeV. In addition, the  $\gamma$ -ray derived neutrino spectrum  $E^{-\gamma}$  with  $\gamma = -2.25$  is considered for Mrk 501 (see Sec. 6.1). Such spectrum is selected taken into account the  $\gamma$ -ray attenuation due to interaction with the Extragalactic Background Light (EBL). Recently, HAWC released spectral analysis [11] on the Mrk 421 and Mrk 501 for the periods of observation from [1] with the EBL correction of two models described in [12, 13] applied. The  $\gamma$ -ray spectra to estimate the neutrino flux emitted by the sources is taken from [11] and the estimation is done (see Sec. 6.1). Due to not well known ratio between cutoff for  $\gamma$  and  $\nu$  fluxes, the  $\gamma$ -ray spectrum for Mrk 421 with existing  $\gamma$ -ray cutoff at 5 TeV is not considered to derive corresponding neutrino spectrum.

Final set of spectra used in the analysis is:

- $(E_\nu/1\text{ GeV})^{-1.0} \exp(-E_\nu/1\text{ PeV})$  (both);
- $(E_\nu/1\text{ GeV})^{-2.0}$  (both);
- $(E_\nu/1\text{ GeV})^{-2.5}$  (both);
- $(E_\nu/1\text{ GeV})^{-2.25}$  (Mrk 501 only).

## 6.1 Gamma-ray derived neutrino spectra

From the observed spectrum, the  $\gamma$ -ray spectrum at the source can be estimated using EBL attenuation correction (see Sec. 6.1.1), which then can be used to estimate a probable neutrino spectrum.

The one neutrino spectrum is selected for the analysis:

- Mrk 501:  $(E_\nu/1\text{ GeV})^{-2.25}$ .

### 6.1.1 EBL attenuation correction

The VHE  $\gamma$ -rays emitted by an extragalactic source interact with the background photons of EBL via pair-production and the flux is attenuated. The attenuation of flux depends on the redshift of the source and on the energy. To model the intrinsic source spectra, this attenuation effect has to be taken into account.

With the known optical depth  $\tau(z, E_\gamma)$  for a redshift  $z$  and an energy  $E$  from a particular EBL model, the intrinsic spectrum for a given observed spectrum of a source can be calculated multiplying by the attenuation factor to de-absorb the spectrum using Eq. 4

$$\frac{dF}{dE} \Big|_{int} = \frac{dF}{dE} \Big|_{obs} \cdot e^{\tau(z, E_\gamma)} \quad (4)$$

There are different approaches to calculate the EBL. Three models Franceschini 08 [12], Domínguez 10 [14] and Gilmore 12 [13] consider these approaches:

- forward evolution [13], which begins with cosmological initial conditions and semi-analytically models the absorption during the galaxy evolution with time;
- backward evolution [12], which begins with existing galaxy populations and evolves them backwards in time;
- evolution that is directly observed [14] over a range of redshift;

The example of optical depth and corresponding attenuation versus energy for three models is shown in Fig. 12.

The Table 3 combines the spectra and cutoff information obtained from [1] and [11]. The discussion of the absorption features of the EBL is beyond the scope of [1] and a more detailed analysis of the HAWC AGN spectra done in [11] with two models [12] and [13] of  $\gamma$ -rays absorption on the EBL applied.

For the EBL correction the model in [12] is selected as it gives the tables for the redshift with the step=0.001. In the energy range of the analysis (HAWC: 0.1-100 TeV) the three models [12–14] show good agreement. Both AGNs are located at the redshift  $z=0.031$  and  $z=0.034$  for Mrk 421 and Mrk 501 respectively and the optical depths for the sources are almost equal.

The  $\gamma$ -ray spectra and cutoff information from [11] obtained with the models [12, 13].

For Mrk 421: we have  $\gamma = -2.04 \pm 0.07 / -2.02 \pm 0.09$  and cutoff  $E_{cut} = 5.28 \pm 0.87 / 4.75 \pm 0.70$  for model from [12] and [13] respectively (see Table 3). Due to good compatibility and taken into account the errors, the  $\gamma = -2.0$  and  $E_{cut} = 5.0$  TeV cutoff can be selected as a  $\gamma$ -ray spectrum. As discussed in Sec. 6 due to not well known ratio between cutoff for  $\gamma$  and  $\nu$  fluxes, the  $\gamma$ -ray spectrum for Mrk 421 with existing  $\gamma$ -ray cutoff at 5 TeV is not considered to derive corresponding neutrino spectrum.

For Mrk 501: we have  $\gamma = -2.15 \pm 0.06 / -2.25 \pm 0.04$  and no cutoff for model from [12] and [13] respectively (see Table 3). In [11] it is concluded that there is no a significant improvement with and without an exponential energy cut-off and the simple power law can well describe Mrk 501 intrinsic

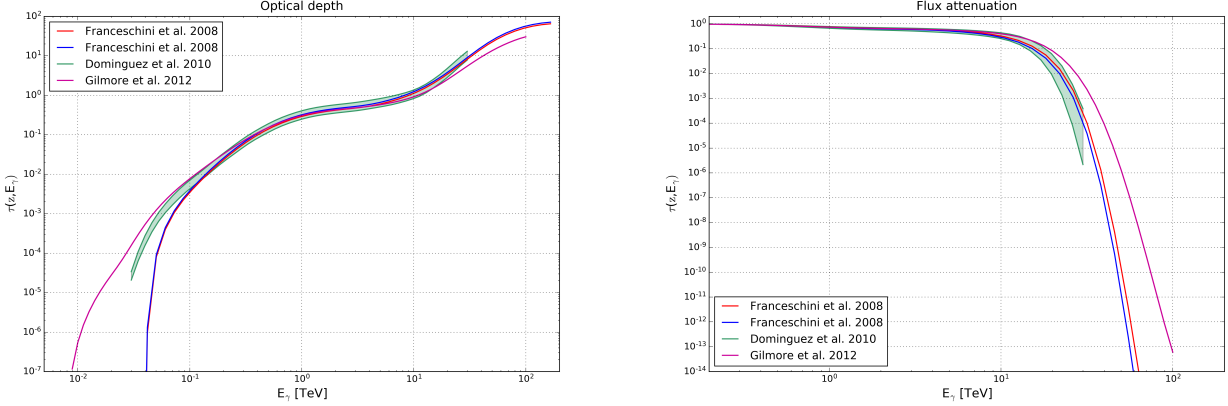


Figure 12: *Left panel:* The optical depth  $\tau(z, E_\gamma)$  versus energy of  $\gamma$ -ray photons for Mrk 421 and Mrk 501. *Right panel:* The attenuation  $e^{-\tau(z, E_\gamma)}$  of  $\gamma$ -rays versus energy for sources. The red and blue color lines represent results from [12] for Mrk 421 at redshift  $z=0.031$  and Mrk 501 at redshift  $z=0.034$  respectively. Dashed green color region represent results from [14], the range is between  $z=0.025$  and  $z=0.040$  of which the data table is available. Violet line represent results from [13] at  $z=0.030$  of which the data table is available.

Table 3: Spectra and cutoff

	Mrk 421	Mrk 501
$\Gamma^{**}$	$2.21 \pm 0.14_{\text{stat}} \pm 0.20_{\text{sys}}$	$1.60 \pm 0.30_{\text{stat}} \pm 0.20_{\text{sys}}$
$E_{\text{cut}}^*$	$5.4 \pm 1.1_{\text{stat}} \pm 1.0_{\text{sys}}$	$5.7 \pm 1.6_{\text{stat}} \pm 1.0_{\text{sys}}$
$\Gamma^{*1}$	$2.02 \pm 0.09$	$2.25 \pm 0.04$
$E_{\text{cut}}^{*1}$	$4.75 \pm 0.70$	-
$\Gamma^{*2}$	$2.04 \pm 0.07$	$2.15 \pm 0.06$
$E_{\text{cut}}^{*2}$	$5.28 \pm 0.87$	-

\*\* from [1] of HAWC observation.

\*1 from [11] Gilmore 12 model used.

\*2 from [11] Franceschini 08 model used.

spectra. Taking into account the fact of no cutoff here, and that in the analysis a generic power-law  $E^{-\gamma}$  with  $\gamma = -2.0$  and  $\gamma = -2.5$  are included, then for appropriate comparison the  $\gamma = -2.25$  can be selected because if the photon spectrum is approximated with a power law  $\Phi_\gamma \propto E^{-\Gamma}$ , hence:

$$\frac{dN_\gamma}{dE} = \left( \frac{E_\gamma}{1 \text{ GeV}} \right)^{-2.25} \Rightarrow \frac{dN_v}{dE} \propto \left( \frac{E_v}{1 \text{ GeV}} \right)^{-2.25} \quad (5)$$

## 6.2 Background time PDF

The background time PDF  $P_b(t)$  is the probability to have a background event at a given time. It is built using the distribution in time of ANTARES events with following criteria:  $\Lambda > -5.6$ , number of hits in PMTs  $n_{hit} > 5$  in more than one line  $N_{line} > 1$ , the reconstructed zenith  $\cos(\theta) > -0.1$ , and an estimated angular uncertainty on the fitted muon track direction  $\beta < 1.0^\circ$  (see Fig. 13).

Background time PDF for different  $\Lambda$  is shown in Fig. 14. Bkg time PDF shows good stability for different  $\Lambda$  (see Fig. 15) and it is built once for the whole analysis with  $\Lambda > -5.6$  (see Fig. 13). As seen, bkg time PDF is more stable especially in  $\Lambda \in [-5.8; -5.0]$  range.

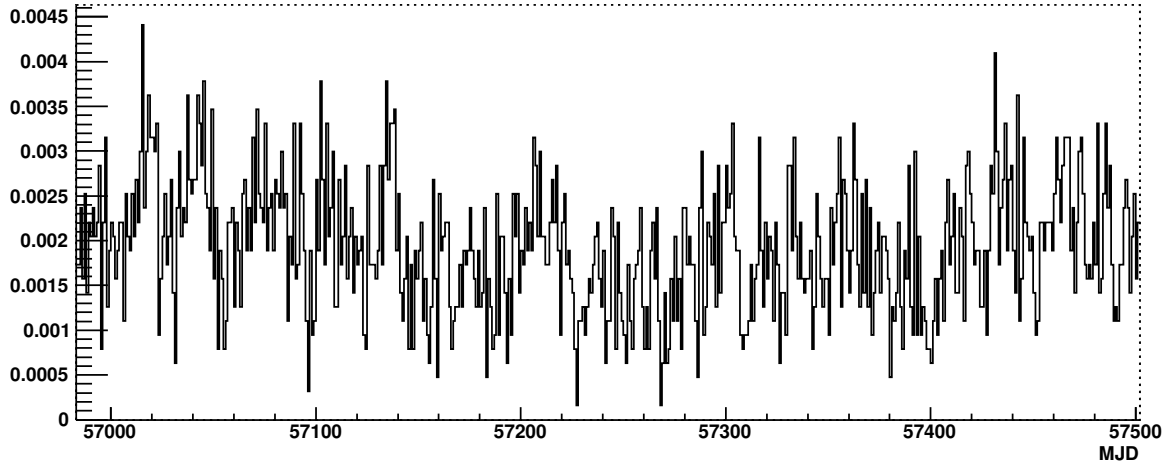


Figure 13: The normalized to unity ANTARES background time distribution of selected period made for quality parameter  $\Lambda > -5.6$ , reconstructed zenith  $\cos(\theta) > -0.1$ , and an estimated angular uncertainty on the fitted muon track direction  $\beta < 1.0^\circ$  with number of hits in PMTs  $n_{hit} > 5$  in more than one line  $N_{line} > 1$ . The size of the bin is 1 day.

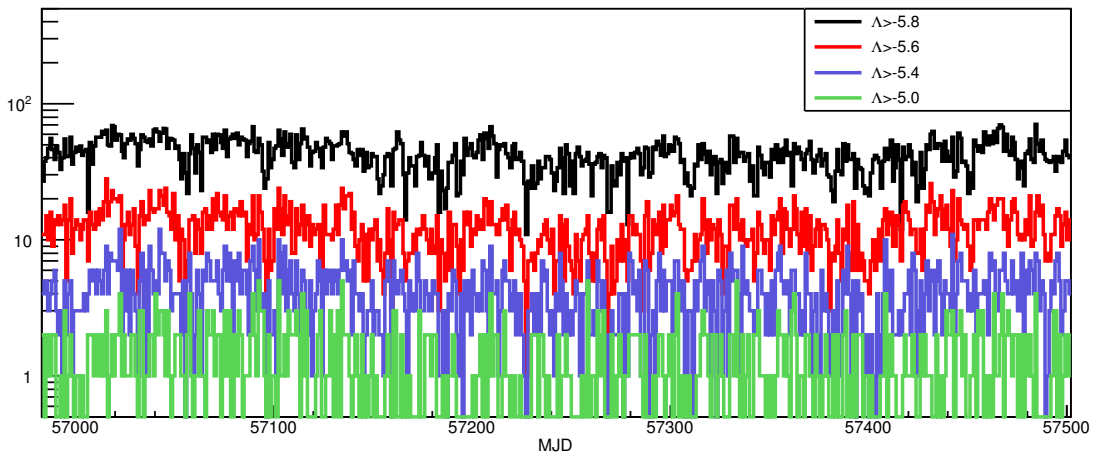


Figure 14: Background time PDF of selected period for several  $\Lambda$  values with  $\cos(\theta) > -0.1$ ,  $\beta < 1.0^\circ$ ,  $n_{hit} > 5$ ,  $N_{line} > 1$  conditions applied.

Ratios  $\Lambda > X / \Lambda > -5.4$

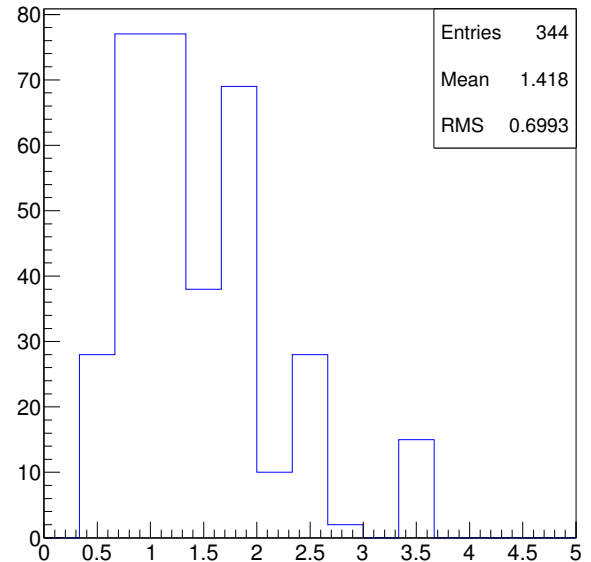
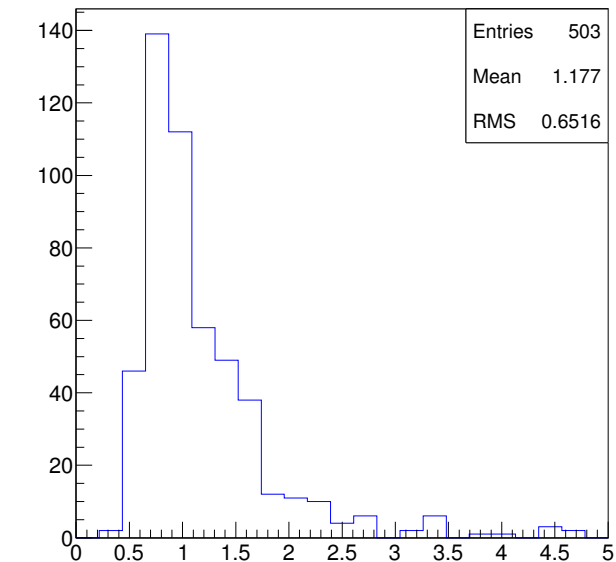
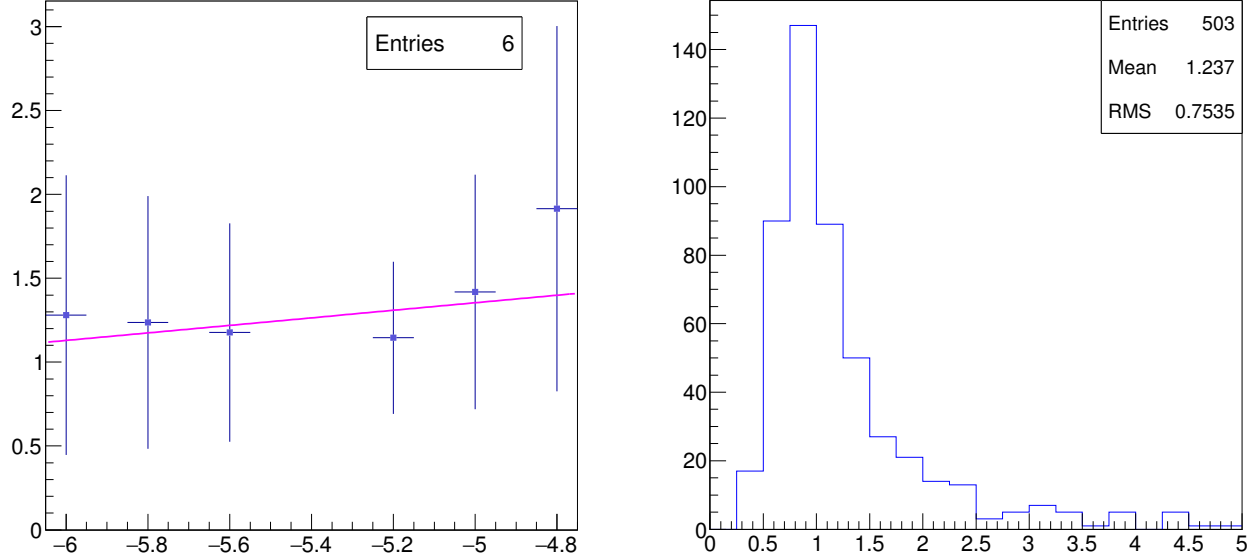


Figure 15: *Upper left panel:* The mean value and the errors of distributions of bkg time PDF ratios of  $\Lambda > X_i / \Lambda > X_{\text{ref}}$  for  $X_i = -6.0, -5.8, -5.6, -5.2, -5.0, -4.8$  with the reference to  $\Lambda_{\text{ref}} > -5.4$ . The pink color line represent the linear fit. *Upper right panel and Lower panel:* Example of distributions of normalized bkg time PDF ratios  $\Lambda > X_i / \Lambda > X_{\text{ref}}$  for  $X_i = -5.8, -5.6, -5.0$  with the reference to  $\Lambda_{\text{ref}} > -5.4$ .

## 7 Flares selection

In the analysis two cases considered for neutrino injection during PEX:

- Long (L) case: All flares selected.
- Short (S) case: Only peaks which pass a given threshold are selected.

The Fig. 6 represent signal time PDFs used in the analysis for long case (L). Selection of the peaks as the most promising flaring periods improve the analysis performance. Several selection criteria in short (S) case can be established as a threshold in order to identify the flaring periods of interest: *average flux*, *average flux + 1 $\sigma$* , *average flux + 2 $\sigma$*  (see Fig. 16, 17). This, in turn, help to see the influence of the threshold definition.

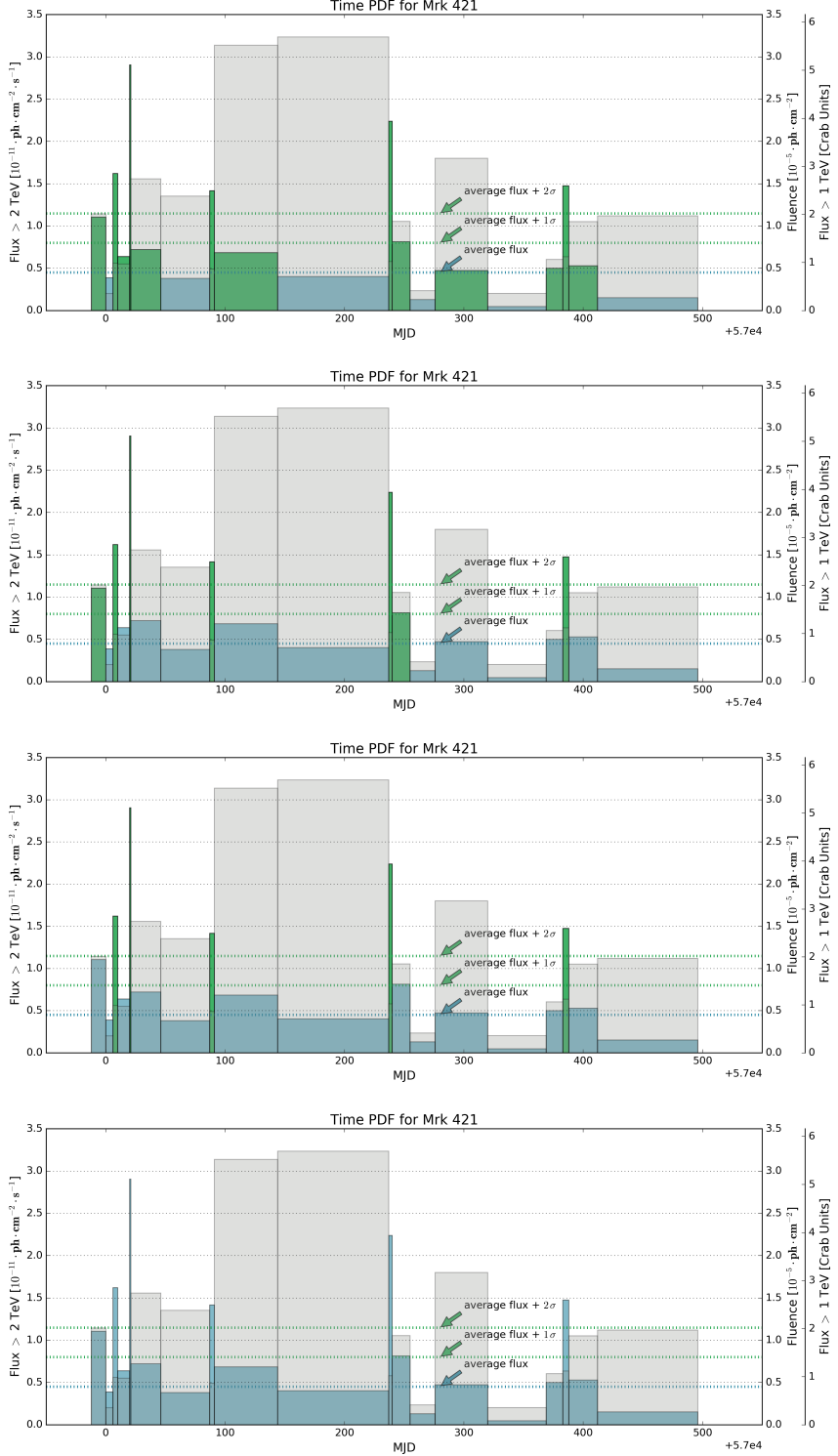


Figure 16: The distinct flare states for Mrk 421 vs threshold. The blue dotted line represent the average fluxes  $\sim 0.8$  CU; the green dotted lines represent the peak selection thresholds: *average flux*, *average flux + 1 $\sigma$* , *average flux + 2 $\sigma$* . The bottommost plot shows the long case, the three upper plots show short case for *average flux*, *average flux + 1 $\sigma$* , *average flux + 2 $\sigma$*  respectively. The left axes represent the units of the fluxes, the right-right axis represent the fluxes in corresponding Crab Units (CU). The right-left axes represent the units of fluences shown as shaded grey areas.

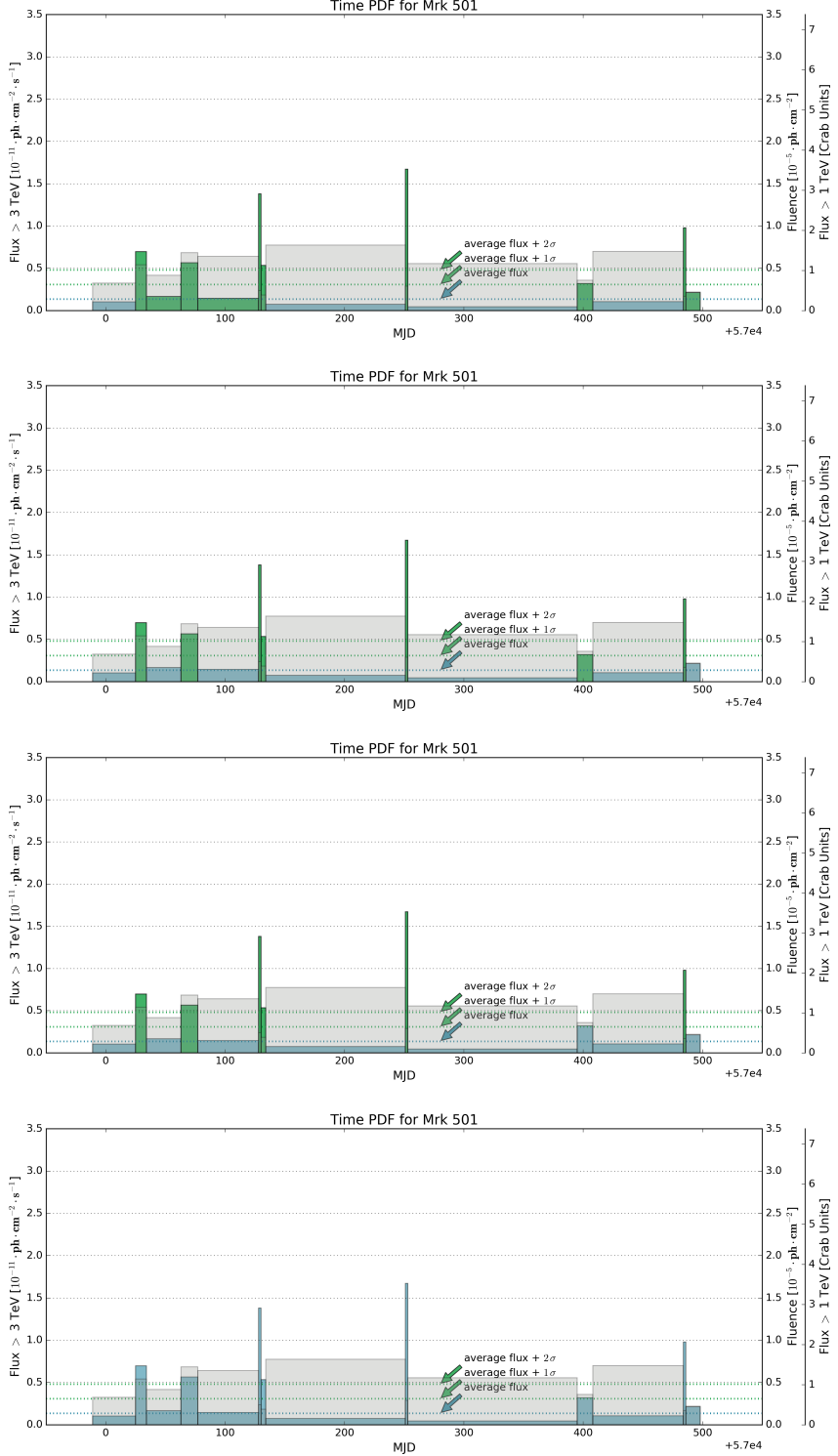


Figure 17: The distinct flare states for Mrk 501 vs threshold. The blue dotted line represent the average fluxes  $\sim 0.3$  CU; the green dotted lines represent the peak selection thresholds: *average flux*, *average flux + 1 $\sigma$* , *average flux + 2 $\sigma$* . The bottommost plot shows the long case, the three upper plots show short case for *average flux*, *average flux + 1 $\sigma$* , *average flux + 2 $\sigma$*  respectively. The left axes represent the units of the fluxes, the right-right axis represent the fluxes in corresponding Crab Units (CU). The right-left axes represent the units of fluences shown as shaded grey areas.

## 8 Analysis

In this section, the analysis results for Mrk 421 and Mrk 501 for all spectra discussed:

- $E^{-1.0} \exp(-E/1\text{PeV})$  (both);
- $E^{-2.0}$  (both);
- $E^{-2.5}$  (both);
- $E^{-2.25}$  (Mrk 501 only).

For each spectra four cases have been studied: long case with all flare states selected and short case with flare states above three given thresholds selected in order to estimate the influence of the peaks selection definition:

- *average flux*;
- *average flux + 1 $\sigma$* ;
- *average flux + 2 $\sigma$* .

### 8.1 Discovery signal

For each PEX the test statistic  $Q$  was calculated. Using the background-only distribution  $H_0(Q)$ , the lowest test statistics  $Q$ -value  $Q_p^X$  that is necessary to claim a discovery with a certain p-value and significance  $X$  can be calculated with [15]:

$$P(Q \geq Q_p^X | \mu_B) = \int_{Q_p^X}^{\infty} H_0(Q) dQ = p. \quad (6)$$

Higher values of  $Q$  indicate that the measurement is more compatible with the signal hypothesis  $H_1$ . The example of probability distributions  $H_1(Q)$  for different  $N_S$  are shown in Fig. 18 with the  $3\sigma$  and  $5\sigma$  threshold  $Q$ -values indicated by the dotted vertical lines. Here,  $Q^{3\sigma} = 3.1$  as counted and  $Q^{5\sigma} = 8.95$  as obtained from the fit.

The probability distribution of  $Q$  values for any number of expected signal events  $\mu_S$  is calculated via [15]:

$$P(Q|\mu_S) = \sum_{N_S}^{\infty} P(N_S|\mu_S) \cdot H_1(Q), \quad (7)$$

with the Poisson distribution  $P(N_S|\mu_S)$  giving the probability of observing  $N_S$  events from a mean number of expected events  $\mu_S$ .

The integral of  $P(Q|\mu_S)$  gives the model discovery potential (MDP) (see Sec. 8.4); it is the probability to make a discovery assuming that the model was correct [15]:

$$\begin{aligned} MDP^X &= P(Q \geq Q_p^X | \mu_S) = \int_{Q_p^X}^{\infty} P(Q|\mu_S) dQ \\ &= \sum_{N_S}^{\infty} P(N_S|\mu_S) \int_{Q_p^X}^{\infty} H_1(Q) dQ, \end{aligned} \quad (8)$$

where  $\int_{Q_p^X}^{\infty} H_1(Q) dQ$  gives the discovery signal, an amount of signal required to have a test statistic  $Q$ -value over  $Q^X$  (with significance  $X$ ) in 50% of the trials (50% C.L.). The discovery power plots for

Mrk 421 with the energy spectrum  $E^{-2.0}$  and cut on zenith angle  $\cos(\theta) > -0.1$  for optimum lambda cut  $\Lambda > -5.3$  with selected signals at  $3\sigma$  evidence and  $5\sigma$  discovery can be seen in Fig 19.

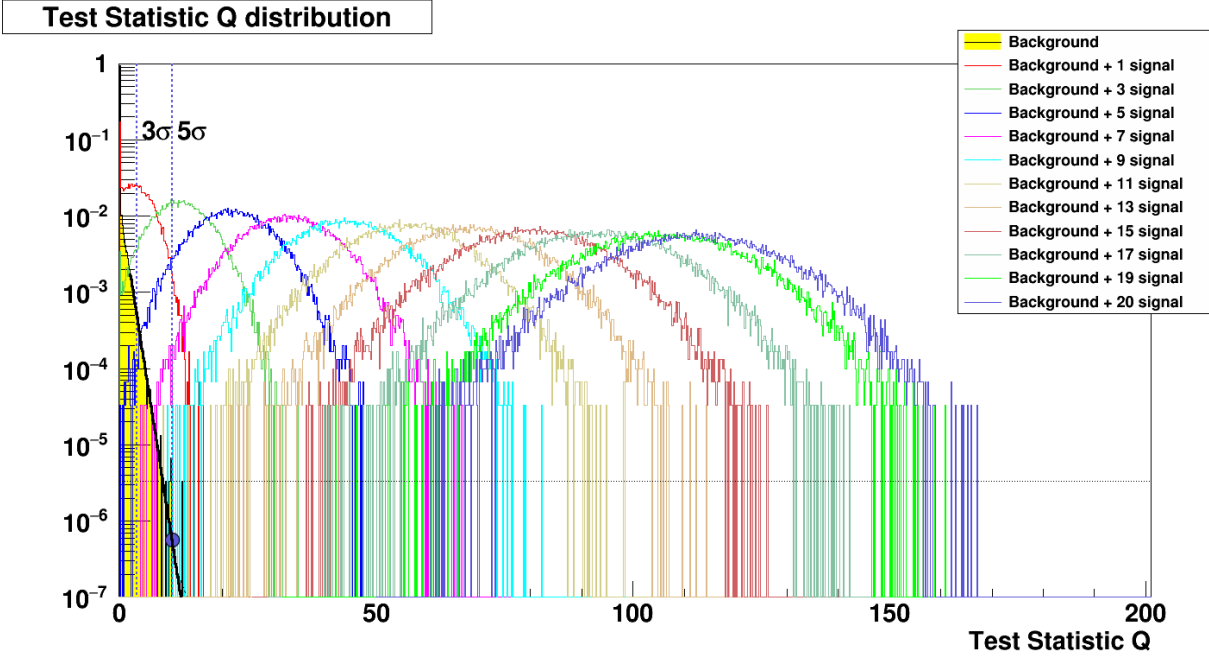


Figure 18: Probability distribution of the test statistic variable issued from pseudo experiments for background-only  $H_0$  (yellow area) and by adding from 1 up to 20 signal neutrinos  $N_S$  around the source (red, green, blue, ... etc colors represent  $N_S = 1, 3, 5, \dots$  injected signal events) for Mrk 421 with the energy spectrum  $E^{-2.0}$  and cut on zenith angle  $\cos(\theta) > -0.1$  for optimum lambda cut  $\Lambda > -5.3$ . The mean background events  $\mu_B = 5.37 \cdot 10^{-5}$ . Dotted vertical lines indicate the threshold values for the  $3\sigma$  and  $5\sigma$  significances for the rejection of the background-only hypothesis. The dotted horizontal line marks the point below which the lack of statistics (one over the total amount of PEXs simulated) and implies an extrapolation by an exponential fit (broad black line) to estimate  $Q^{5\sigma}$ .

The distribution  $P(Q|\mu_S)$  from Eq. 7 is also used to set upper limits on the number of signal events when no discovery is made (see Sec. 9). The 90% confidence level (C.L.) upper limit  $\mu_S^{90\%}$  on the signal is set by rejecting all event expectations  $\mu_S$  that would lead to values  $Q > Q_{\text{final}}$  in 90% of all PEXs when the final analysis returns  $Q_{\text{final}}$  [15]:

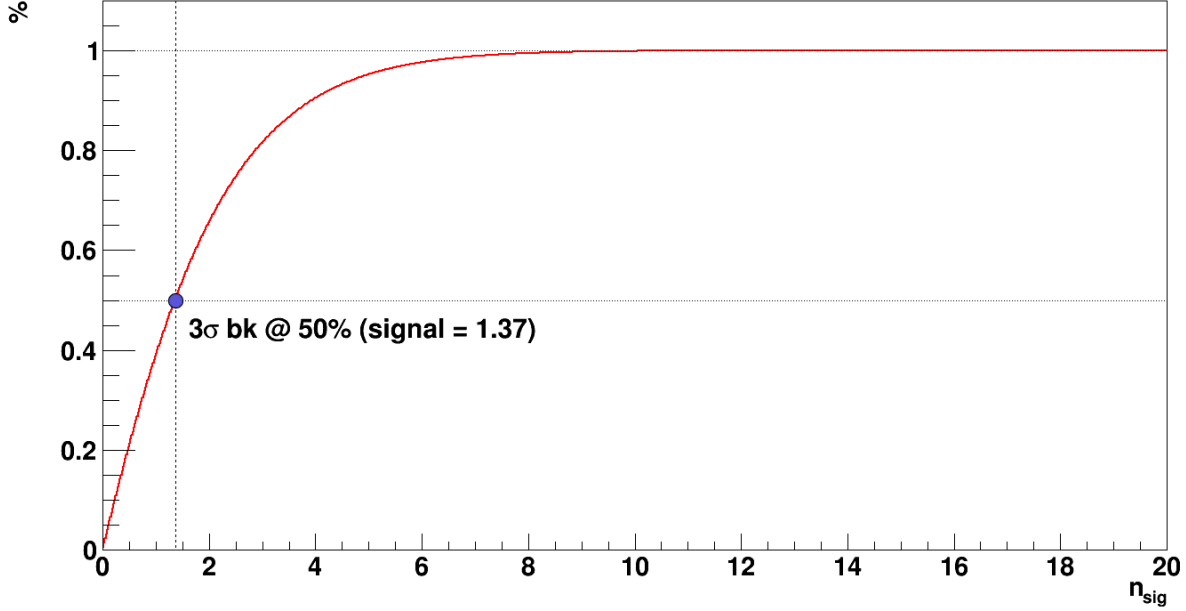
$$P(Q \geq Q_{\text{final}} | \mu_S^{90\%}) = \int_{Q_{\text{final}}}^{\infty} P(Q|\mu_S^{90\%}) dQ = 0.9. \quad (9)$$

For example, when no event was measured ( $Q_{\text{final}} = 0$ ), a 90% C.L. upper limit was set at 2.3, the lowest possible value, derived from Poisson statistics, since the probability to detect at least one event at a mean rate of 2.3 is exactly 90% ( $\mu_S^{90\%} = 2.3$ ):

$$\begin{aligned} 1 - P(x) &= 1 - \frac{e^{-\lambda} \lambda^x}{x!} \Big|_{x=0}^{\lambda=2.3} = 1 - \frac{e^{-2.3} \cdot 1}{0!} \\ &= 1 - 2.71828^{-2.3} = 1 - 0.1 = 0.9. \end{aligned} \quad (10)$$

The number of signal events  $N_S^{3\sigma}, N_S^{5\sigma}$  required for  $3\sigma$  evidence or  $5\sigma$  discovery give the minimum

**Percentage of Signal above the 3 sigma**



**Percentage of Signal above the 5 sigma**

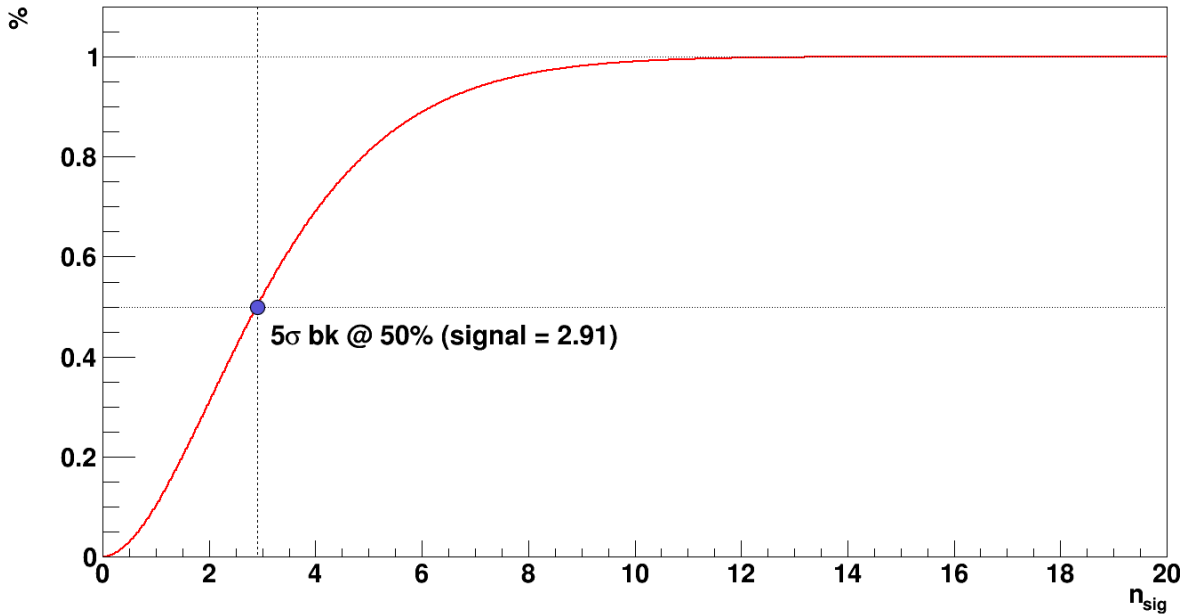


Figure 19: Discovery power at 3 $\sigma$  (top) and 5 $\sigma$  (bottom) levels for Mrk 421 with the energy spectrum  $E^{-2.0}$  for optimum lambda cut  $\Lambda > -5.3$  and  $\cos(\theta) > -0.1$ . Blue circles represent signals selected at 3 $\sigma$ , 5 $\sigma$  levels in 50% of the trials.

flux that could give an evidence at 3 $\sigma$  level or 5 $\sigma$  discovery in 50% of the trials. The Fig. 20 represent  $N_S^{5\sigma}$  versus  $\Lambda$  for the long and the short cases. The plots for 3 $\sigma$  level can be seen in Fig. 57 in Appendix A.2

The conversion of  $N_S$  into the equivalent source flux is done through the acceptance of the detector (see Sec. 8.2).

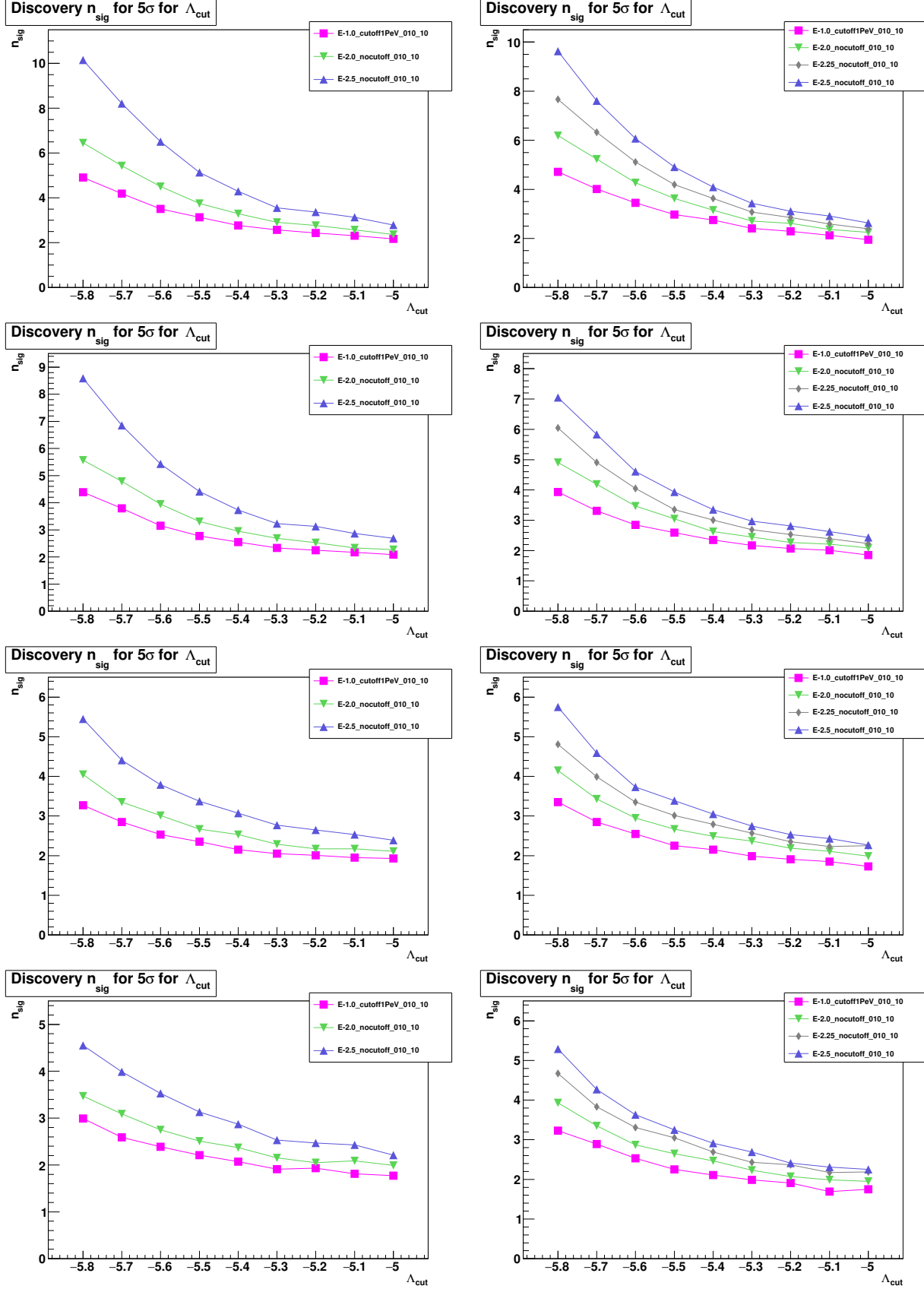


Figure 20: Discovery power at  $5\sigma$  level. *Left panel:* Mrk 421 *Right panel:* Mrk 501. From upper to bottom: all flares, short flares with *average flux*, *average flux + 1 $\sigma$* , *average flux + 2 $\sigma$*  thresholds.

## 8.2 Acceptance

The declination-dependent acceptance  $A_{cc}$  is defined as the proportionality constant between a given flux normalization  $\Phi_0 = E^2 d\Phi/dE$  and the expected number of signal events  $N_{ev}$  to be detected within the telescope for this particular flux:

$$A_{cc} = \frac{N_{ev}}{\Phi_0} \quad (11)$$

It can be expressed in terms of the effective area  $A_{eff}(E_v, \delta)$ :

$$A_{cc} = \Phi_0^{-1} \int dt \int dE_v \frac{d\Phi}{dE_v} A_{eff}(E_v, \delta) \quad (12)$$

The comparison of acceptances for Mrk 421 and Mrk 501 can be seen in Fig. 21, 22 respectively.

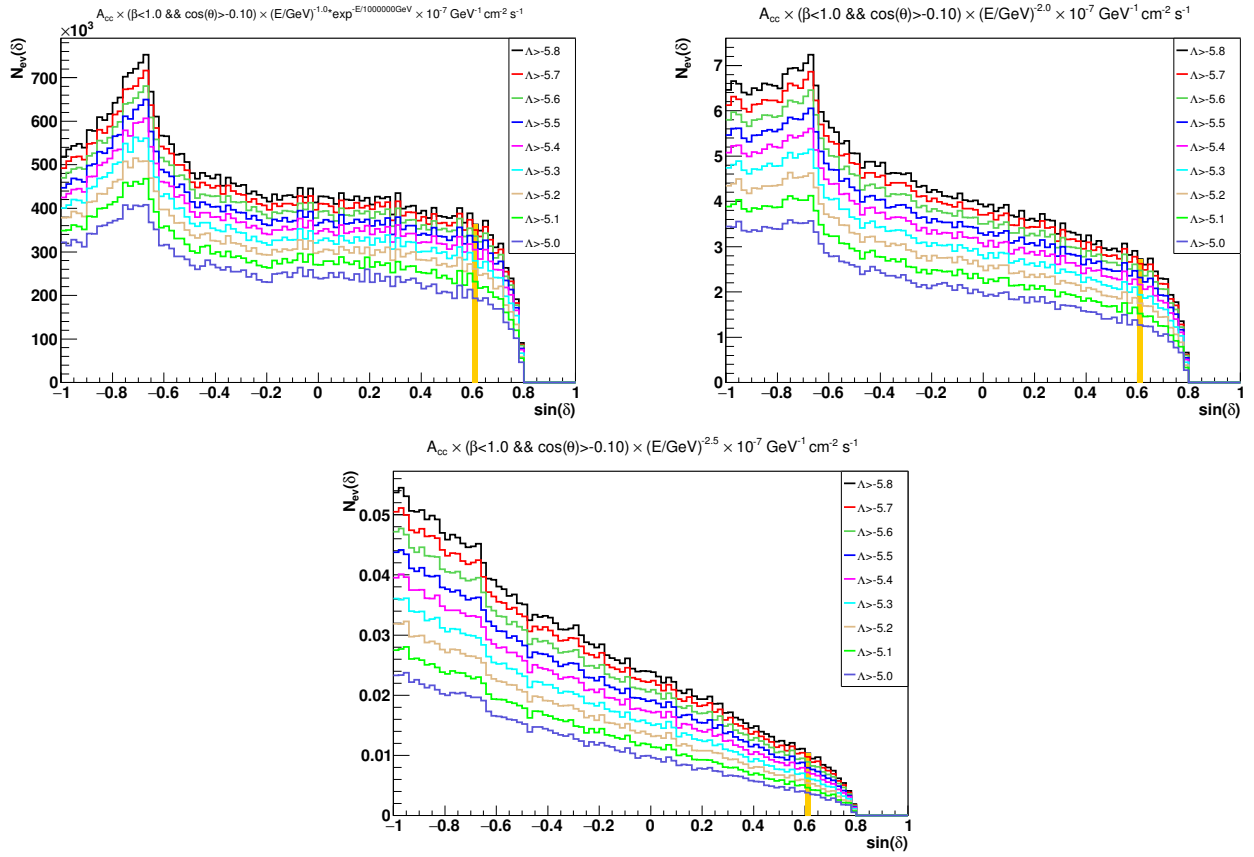


Figure 21: Examples of acceptance for Mrk 421 as a function of the source declination for the several  $\Lambda$  cuts [with  $\beta < 1.0$  and  $\cos(\theta) > -0.1$ ] with a flux normalization factor of  $\Phi_0 = 10^{-7} \text{ GeV}^{-1} \text{ cm}^{-2} \text{ s}^{-1}$  in  $N_{ev} = A_{cc} \times \Phi_0$  magnitudes. The period used: November 26<sup>th</sup>, 2014 - April 20<sup>th</sup>, 2016. *Upper left panel:*  $E^{-1.0} \exp(-E/1\text{PeV})$ . *Upper right panel:*  $E^{-2.0}$ . *Lower panel:*  $E^{-2.5}$ . Orange color represents the bins of the source declination.

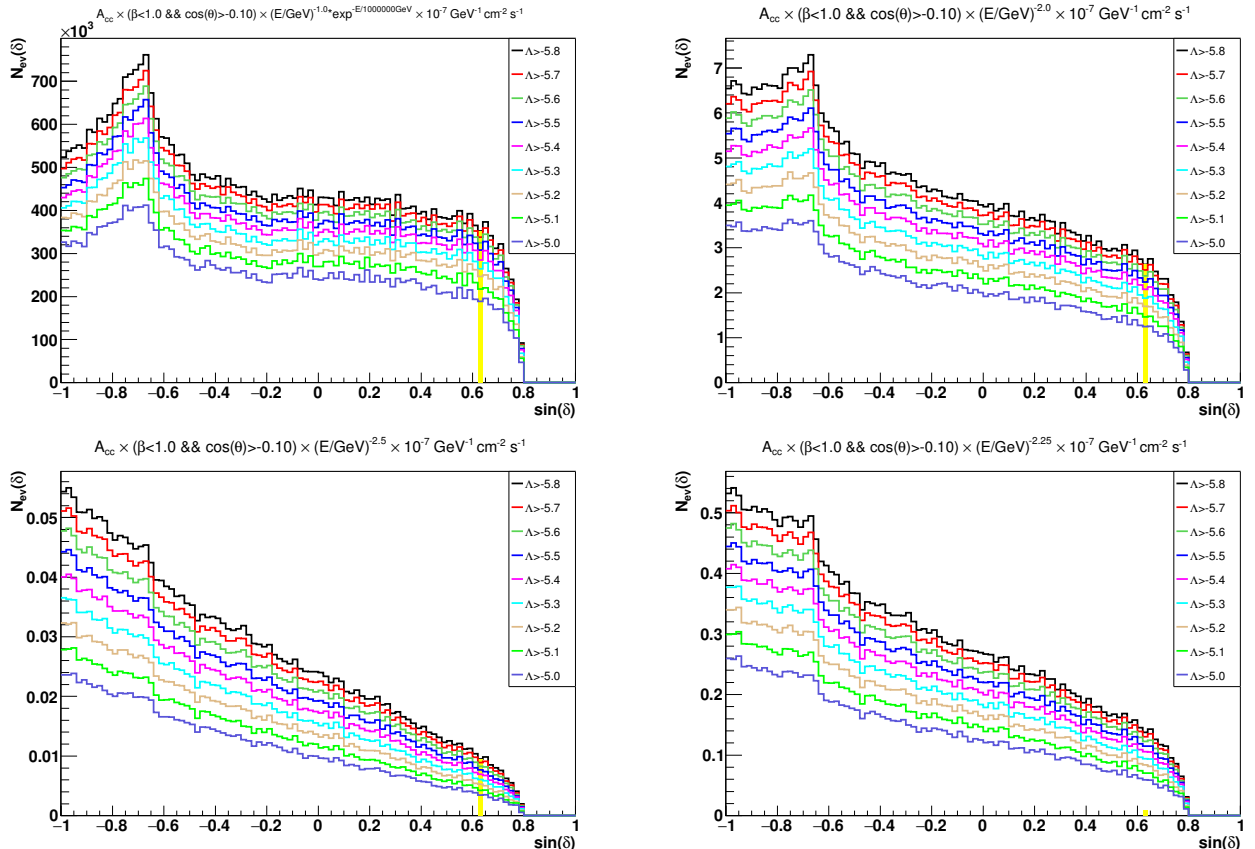


Figure 22: Examples of acceptance for Mrk 501 as a function of the source declination for the several  $\Lambda$  cuts [with  $\beta < 1.0$  and  $\cos(\theta) > -0.1$ ] with a flux normalization factor of  $\Phi_0 = 10^{-7} \text{ GeV}^{-1} \text{ cm}^{-2} \text{ s}^{-1}$  in  $N_{ev} = A_{cc} \times \Phi_0$  magnitudes. The period used: November 26<sup>th</sup>, 2014 - April 20<sup>th</sup>, 2016. *Upper left panel:*  $E^{-1.0} \exp(-E/1\text{PeV})$ . *Upper right panel:*  $E^{-2.0}$ . *Lower left panel:*  $E^{-2.5}$ . *Lower right panel:*  $E^{-2.25}$ . Yellow color represents the bins of the source declination.

### 8.3 Discovery fluxes

In this section the discovery fluxes obtained in analysis for all spectra with all flare states selected (long case) and with only flare states above *average flux*, *average flux + 1 $\sigma$* , *average flux + 2 $\sigma$*  threshold selected (short case) are discussed.

Discovery flux level  $DF_{5\sigma}^{50\%CL}$  is the flux required to have a test statistic TS over  $TS_{5\sigma}$  in 50% of trials. Discovery fluxes  $DF_{5\sigma}^{50\%CL}$  versus  $\Lambda$  for cut on the reconstructed zenith  $\cos(\theta) > -0.1$  and cases of all flares and only peaks are shown in Fig. 23, 24. The plots for discovery fluxes at 3 $\sigma$  level can be seen in Fig. 58, 59 in Appendix A.2. Obtained  $DF_{5\sigma}^{50\%CL}$  for short cases (only peaks) is higher than  $DF_{5\sigma}^{50\%CL}$  discovery fluxes for all flares (long case). But such method gives much better results (lower required discovery fluxes) than simple short case analysis with no long-short rescale procedure considered.

As far as HAWC detector operates nearly continuously and provide data for almost each day and longer periods have better acceptance, the usage of all available flares (long case) is obviously preferable (see comparison plots in Fig. 23, 24 and Fig. 58, 59). Taking into account such long duration flare timing information given by HAWC gamma-ray observations, it significantly improves the efficiency of the search for a neutrino counterpart with ANTARES telescope.

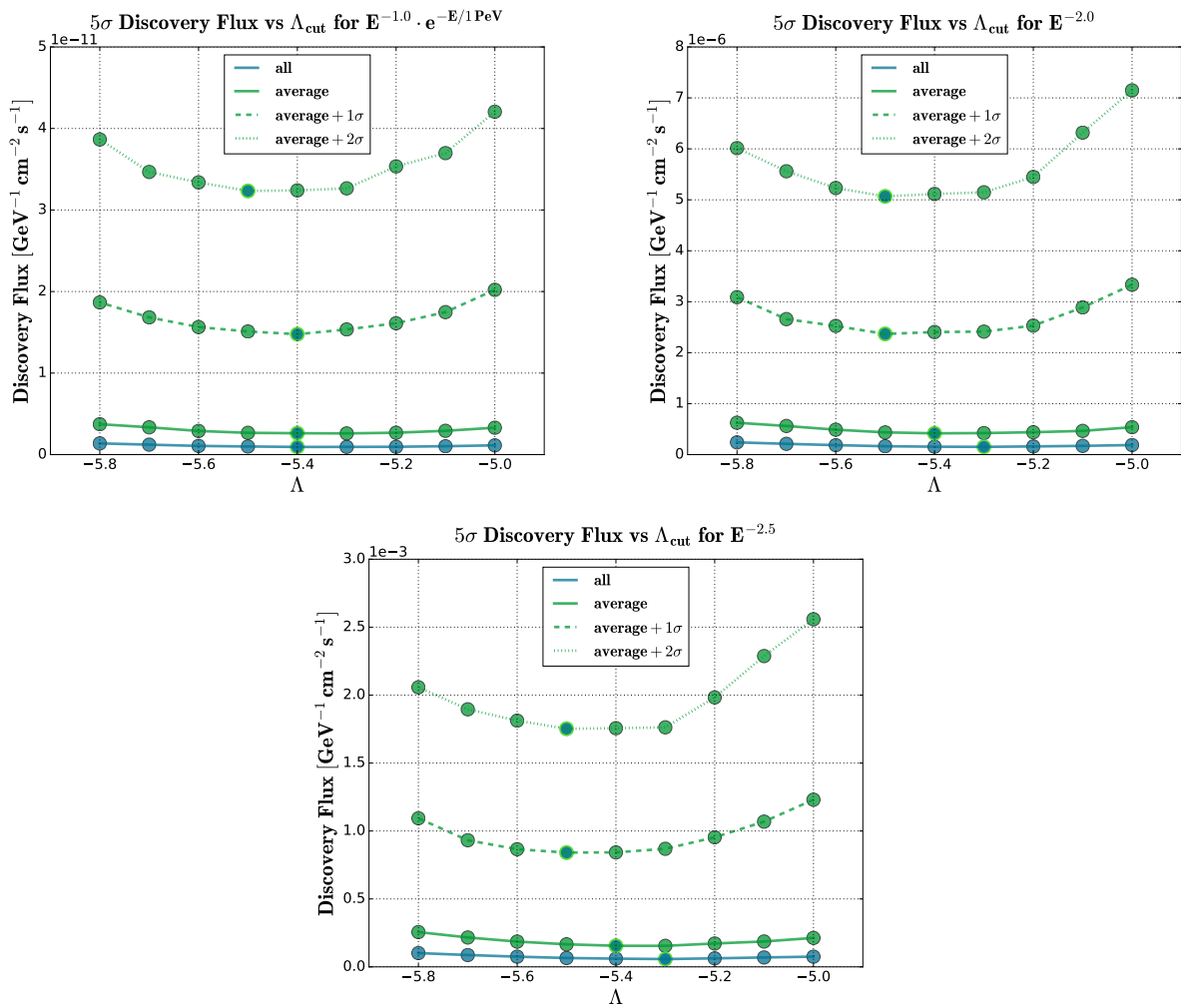


Figure 23: Discovery fluxes comparison at  $5\sigma$  level for Mrk 421 for several thresholds. *Upper left panel:*  $E^{-1.0} \exp(-E/1 \text{PeV})$ . *Upper right panel:*  $E^{-2.0}$ . *Lower panel:*  $E^{-2.5}$ . Light green color circles represent the values with  $\Lambda$  that maximizes  $MDP^{5\sigma}$ .

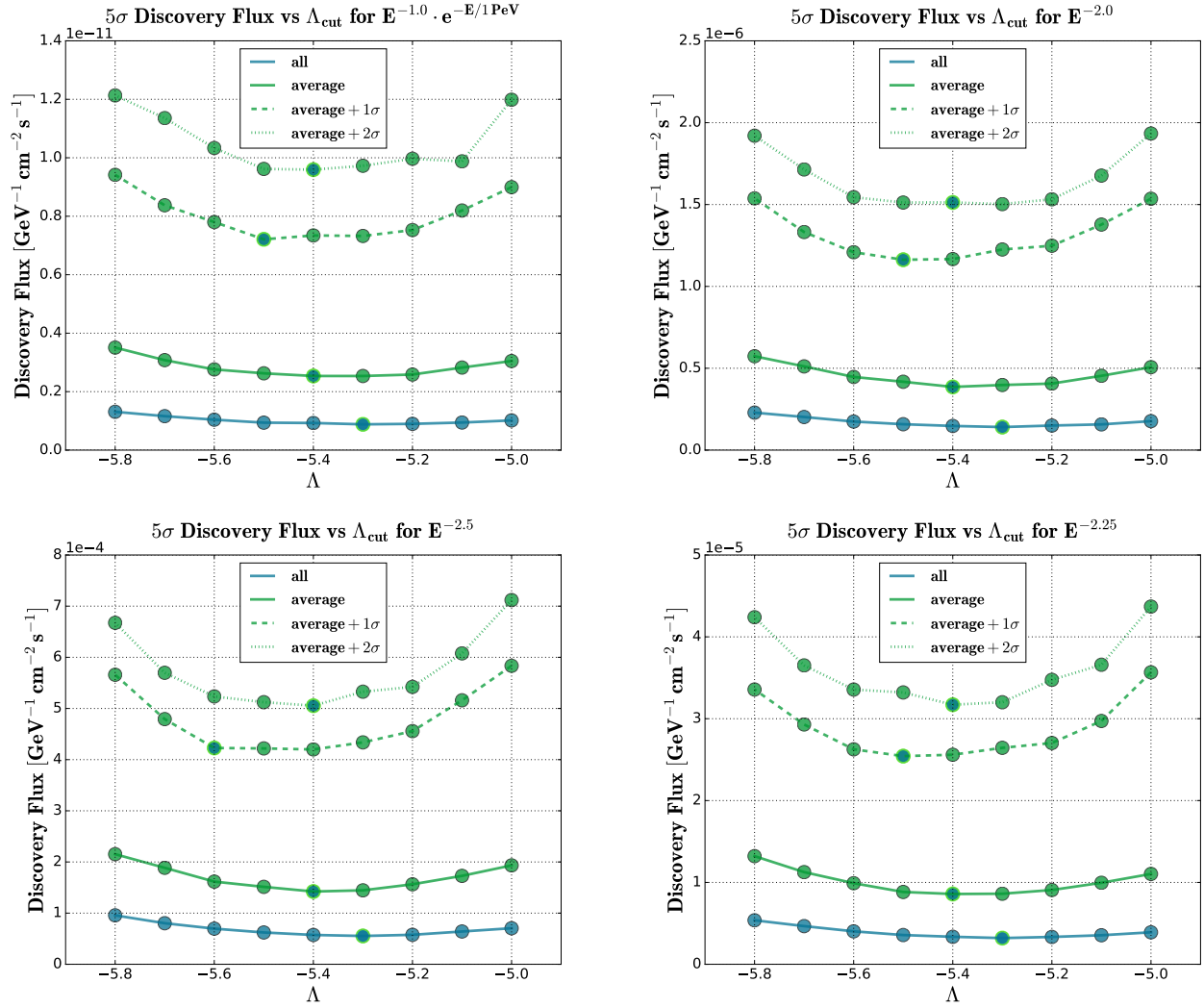


Figure 24: Discovery fluxes comparison at  $5\sigma$  level for Mrk 501 for several thresholds. *Upper left panel:*  $E^{-1.0} \exp(-E/1\text{PeV})$ . *Upper right panel:*  $E^{-2.0}$ . *Lower left panel:*  $E^{-2.5}$ . *Lower right panel:*  $E^{-2.25}$ . Light green color circles represent the values with  $\Lambda$  that maximizes  $\text{MDP}^{5\sigma}$ .

Table 4: Results on optimization for Mrk 421

	T <sub>flare</sub>	LT	$\Lambda$	$N_S^{3\sigma}$	$\Lambda$	$N_S^{5\sigma}$	$DF_{3\sigma}^{50\%CL}$	$DF_{5\sigma}^{50\%CL}$
$E^{-1.0} \exp(-E/1\text{PeV})$								
L	508	491.66	-5.3	1.15	-5.4	2.77	0.42	0.94
S: av.	213	210.52	-5.3	1.03	-5.4	2.55	1.15	2.62
S: av. + 1 $\sigma$	44	43.509	-5.3	0.87	-5.4	2.15	6.51	14.8
S: av. + 2 $\sigma$	17	16.149	-5.4	0.87	-5.5	2.21	13.6	32.3
$\times 10^{-12} \cdot \text{GeV}^{-1} \text{cm}^{-2} \text{s}^{-1}$								
$E^{-2.0}$								
L	508	491.66	-5.3	1.37	-5.3	2.91	0.72	1.52
S: av.	213	210.52	-5.3	1.19	-5.4	2.95	1.87	4.18
S: av. + 1 $\sigma$	44	43.509	-5.3	0.93	-5.5	2.67	9.80	23.7
S: av. + 2 $\sigma$	17	16.149	-5.3	0.83	-5.5	2.51	19.9	50.7
$\times 10^{-7} \cdot \text{GeV}^{-1} \text{cm}^{-2} \text{s}^{-1}$								
$E^{-2.5}$								
L	508	491.66	-5.3	1.75	-5.3	3.55	0.28	0.58
S: av.	213	210.52	-5.4	1.85	-5.4	3.73	0.77	1.55
S: av. + 1 $\sigma$	44	43.509	-5.3	1.09	-5.5	3.37	3.42	8.41
S: av. + 2 $\sigma$	17	16.149	-5.4	1.11	-5.5	3.13	6.79	17.5
$\times 10^{-4} \cdot \text{GeV}^{-1} \text{cm}^{-2} \text{s}^{-1}$								

Table 5: Results on optimization for Mrk 501

	T <sub>flare</sub>	LT	$\Lambda$	$N_S^{3\sigma}$	$\Lambda$	$N_S^{5\sigma}$	$DF_{3\sigma}^{50\%CL}$	$DF_{5\sigma}^{50\%CL}$
$E^{-1.0} \exp(-E/1\text{PeV})$								
L	509	492.88	-5.3	1.09	-5.3	2.41	0.40	0.60
S: av.	138	136.55	-5.3	0.95	-5.4	2.35	1.11	2.54
S: av. + 1 $\sigma$	46	45.928	-5.3	0.85	-5.5	2.25	3.13	7.21
S: av. + 2 $\sigma$	33	33.100	-5.3	0.83	-5.4	2.11	4.06	9.59
$\times 10^{-12} \cdot \text{GeV}^{-1} \text{cm}^{-2} \text{s}^{-1}$								
$E^{-2.0}$								
L	509	492.88	-5.3	1.25	-5.3	2.71	0.65	1.41
S: av.	138	136.55	-5.3	1.07	-5.4	2.63	1.74	3.86
S: av. + 1 $\sigma$	46	45.928	-5.3	0.91	-5.5	2.67	4.71	11.6
S: av. + 2 $\sigma$	33	33.100	-5.3	0.91	-5.4	2.47	1.37	15.1
$\times 10^{-7} \cdot \text{GeV}^{-1} \text{cm}^{-2} \text{s}^{-1}$								
$E^{-2.25}$								
L	509	492.88	-5.3	1.45	-5.3	3.07	1.51	3.20
S: av.	138	136.55	-5.3	1.19	-5.4	3.01	3.81	8.59
S: av. + 1 $\sigma$	46	45.928	-5.3	1.01	-5.5	3.01	10.4	25.4
S: av. + 2 $\sigma$	33	33.100	-5.3	0.97	-5.4	2.69	12.8	31.7
$\times 10^{-6} \cdot \text{GeV}^{-1} \text{cm}^{-2} \text{s}^{-1}$								
$E^{-2.5}$								
L	509	492.88	-5.3	1.61	-5.3	3.43	0.26	0.55
S: av.	138	136.55	-5.4	1.59	-5.4	3.35	0.68	1.42
S: av. + 1 $\sigma$	46	45.928	-5.3	1.09	-5.6	3.73	1.72	4.23
S: av. + 2 $\sigma$	33	33.100	-5.4	1.25	-5.4	2.91	2.17	5.05
$\times 10^{-4} \cdot \text{GeV}^{-1} \text{cm}^{-2} \text{s}^{-1}$								

## 8.4 MDP

The value of the cut on  $\Lambda$  is optimised for each source on the basis of maximizing a model discovery potential (MDP) [15] for the  $3\sigma$  or  $5\sigma$  significance levels for each neutrino spectrum. MDP sets best limits in case of the no-discovery. Fig. 25 represent the MDP values versus  $\Lambda$  for both sources at  $5\sigma$  level. The MDP plots for  $3\sigma$  level can be seen in Fig. 60 in Appendix A.2.

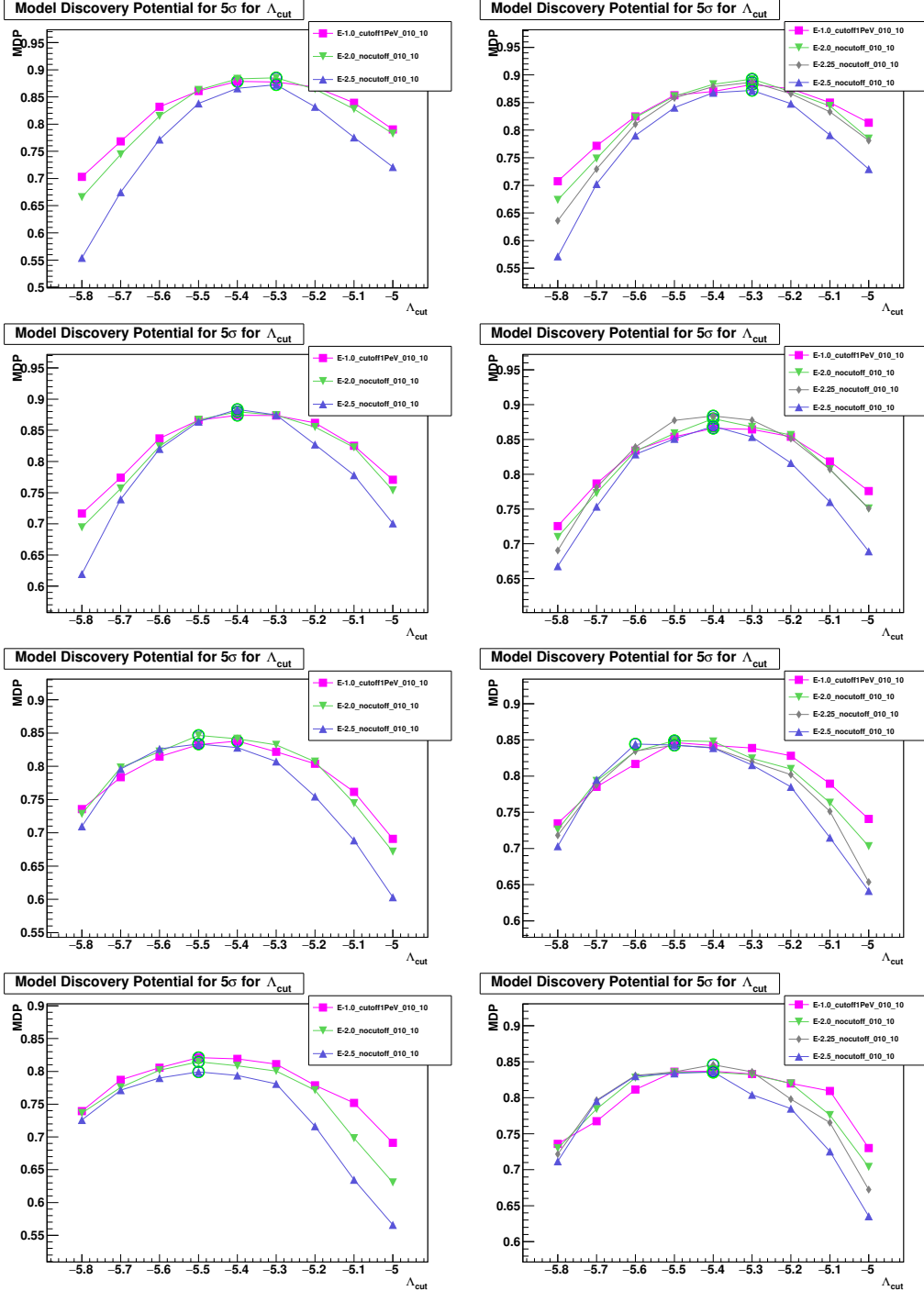


Figure 25: MDP for  $5\sigma$  discovery. *Left panel:* Mrk 421 *Right panel:* Mrk 501. From upper to bottom: all flares, short flares with *average flux*, *average flux +  $1\sigma$* , *average flux +  $2\sigma$*  thresholds.. Light green color circles represent the maximum MDP values.

## 8.5 Sensitivity fluxes

Similarly to  $5\sigma$  discovery fluxes, the discovery flux level  $\text{DF}_{\text{Median}}^{90\% \text{CL}}$  (see Fig. 26, 27) is defined as the sensitivity flux required to have a test statistic  $\text{TS}$  over the median of the background distribution  $\text{TS}_{\text{Median}}$  in 90% of the trials. The sensitivity flux places the upper limit on fluxes at 90% Confidence Level (C.L.). In the absence of a signal, it is used for 90% C.L. sensitivity calculations.

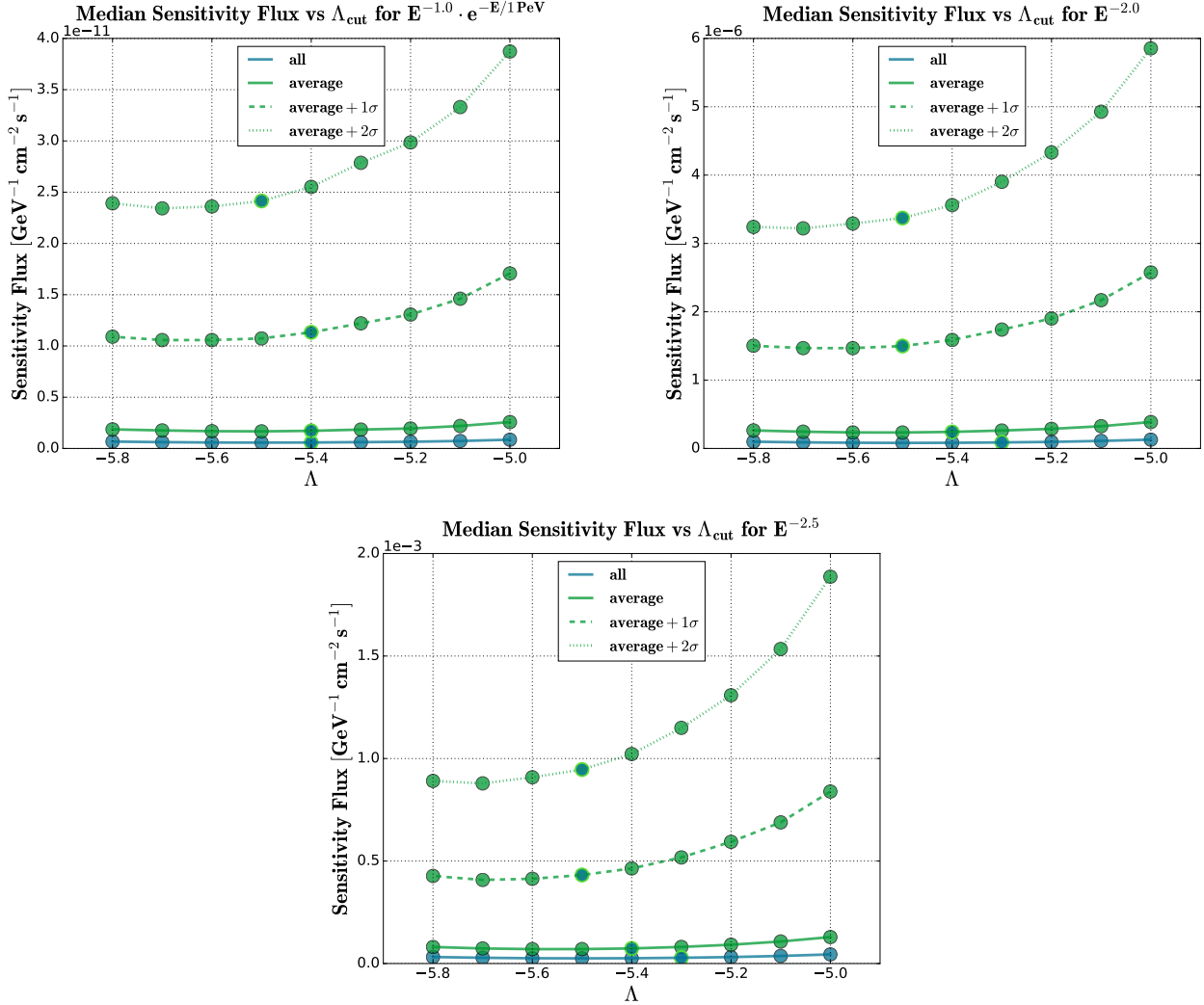


Figure 26: Sensitivity fluxes comparison for Mrk 421 for several thresholds. *Upper left panel:*  $E^{-1.0} \exp(-E/1\text{PeV})$ . *Upper right panel:*  $E^{-2.0}$ . *Lower panel:*  $E^{-2.5}$ . Light green color circles represent the values with  $\Lambda$  that maximizes  $\text{MDP}^{5\sigma}$ .

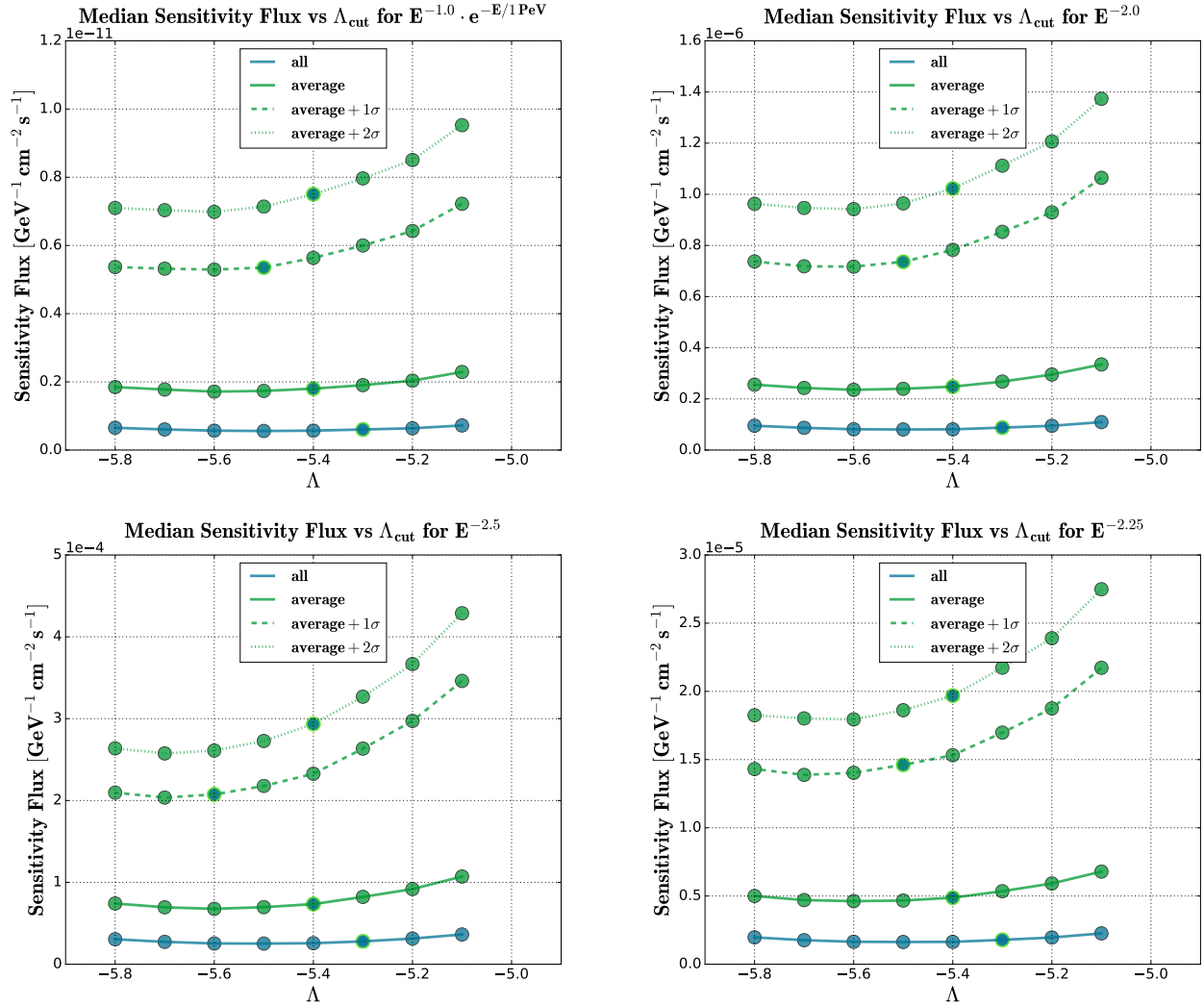


Figure 27: Sensitivity fluxes comparison for Mrk 501 for several thresholds. *Upper left panel:*  $E^{-1.0} \exp(-E/1\text{PeV})$ . *Upper right panel:*  $E^{-2.0}$ . *Lower left panel:*  $E^{-2.5}$ . *Lower right panel:*  $E^{-2.25}$ . Light green color circles represent the values with  $\Lambda$  that maximize  $\text{MDP}^{5\sigma}$ .

## 9 Sensitivities

If no discovery is made, the upper limits will be calculated according to the classical (frequentist) approach [16]. The Neyman [16] 90% C.L. upper limits on the fluence, which is the energy per unit area [ $\text{GeV cm}^{-2}$ ], are calculated as follows:

$$\mathcal{F}^{90\%CL} = \int F dt = F \Delta T = \Delta T \cdot \Phi_0^{90\%CL} \int_{E_{min}}^{E_{max}} E S(E) dE \quad (13)$$

with the energy flux  $F$ , which is the energy per unit area and time [ $\text{GeV}^{-1} \text{cm}^{-2} \text{s}^{-1}$ ], derived as:

$$F = \int E d\Phi = \int E \Phi_E dE = \int E \Phi_0 S(E) dE = \Phi_0 \int E S(E) dE \quad (14)$$

Here:

- $\Delta T$  is the livetime of the search [s];
- $\Phi_0^{90\%CL} = DF^{90\%CL}$  is the upper limit on the neutrino flux normalization [ $\text{GeV}^{-1} \text{cm}^{-2} \text{s}^{-1}$ ];
- $S(E)$  is the dimensionless neutrino spectra  $(\frac{E}{\text{GeV}})^{-\gamma}$ , and  $dN/dE = \Phi_0 \cdot S(E)$ ;
- $E_{min}$  and  $E_{max}$  are 5% and 95% energy limits respectively, defined to contain 90% of the spectrum emission. This is the energy range at which ANTARES is sensible for each spectrum  $S(E)$  and source, and computed from the MC neutrino simulation used to calculate the PSF. The MC neutrino simulation extends up to  $10^8$  GeV.

The 5% and 95% energy limits for each spectrum  $S(E)$  and source are shown in Fig. 28. The sensitivities at 90% C.L. on neutrino fluxes and fluences for each source and spectrum for corresponding limits are listed in Table 6. Additionally, Fig. 29, 30 summarize the sensitivities on the neutrino fluxes and fluences.

Fluence 90% C.L. sensitivities vs  $\Lambda$  for different peak selection thresholds are gathered in Fig. 31, 32.

The tendencies for fluence in the short case for Mrk 421 and Mrk 501 are different. For Mrk 421 the fluence values are worsening with respect to increase of the threshold except for the *average flux* +  $2\sigma$  which gives the sensitivities even better than *average flux* +  $1\sigma$ . For Mrk 501 the fluence values are getting lower with respect to increase of the threshold except for the *average flux* +  $1\sigma$  which gives some worsening w.r.t. the *average flux* case.

As a result, the better sensitivities on the neutrino fluxes can be obtained with the long case for both sources, but the better sensitivities on the neutrino fluences can be obtained with long case for Mrk 421 and in contrary to that with short case and the *average flux* +  $2\sigma$  threshold for Mrk 501 (see Fig. 31, 32).

Table 6: Sensitivities at 90% C.L.

	$S(E)$	T <sub>flare</sub>	LT	$\Lambda$	$E_{min}$	$E_{max}$	$\Phi_0^{90\%CL}$	$\mathcal{F}^{90\%CL}$
Mrk 421	$E^{-1.0} \cdot e^{-E/1\text{PeV}}$			-5.4	4.792	6.392	$5.808^{*1}$	21.0
	$E^{-2.0}$	508	491.659	-5.3	3.960	7.080	$8.846^{*2}$	27.0
	$E^{-2.5}$			-5.3	3.064	5.912	$2.812^{*3}$	67.8
Mrk 501	$E^{-1.0} \cdot e^{-E/1\text{PeV}}$			-5.3	4.808	6.400	$6.038^{*1}$	22.0
	$E^{-2.0}$	509	492.878	-5.3	3.968	7.096	$8.783^{*2}$	26.9
	$E^{-2.25}$			-5.3	3.544	6.496	$0.178^{*3}$	32.3
	$E^{-2.5}$			-5.3	3.088	5.936	$2.792^{*3}$	65.5
							$\cdot \text{GeV}^{-1} \text{cm}^{-2} \text{s}^{-1}$	$\cdot \text{GeV cm}^{-2}$

Note:  $E_{min}$  and  $E_{max}$  in log.

$*^1 \times 10^{-13}$

$*^2 \times 10^{-8}$

$*^3 \times 10^{-5}$

[LT] = [T<sub>flare</sub>] = days.

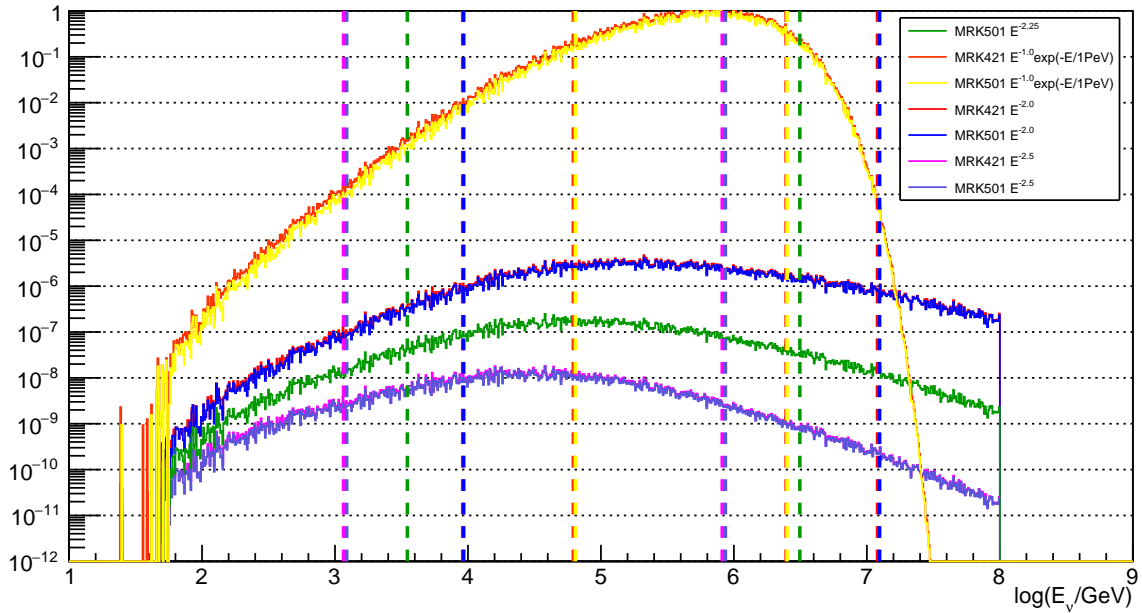


Figure 28: Distribution of the MC neutrinos  $v_\mu + \bar{v}_\mu$  for each spectrum and source for the optimum  $\Lambda$  cuts (with the optimum  $\cos(\theta) > -0.1$  and  $\beta < 1.0$  considered) obtained for the long case. The dotted vertical lines represent the corresponding 5% and 95% energy limits.

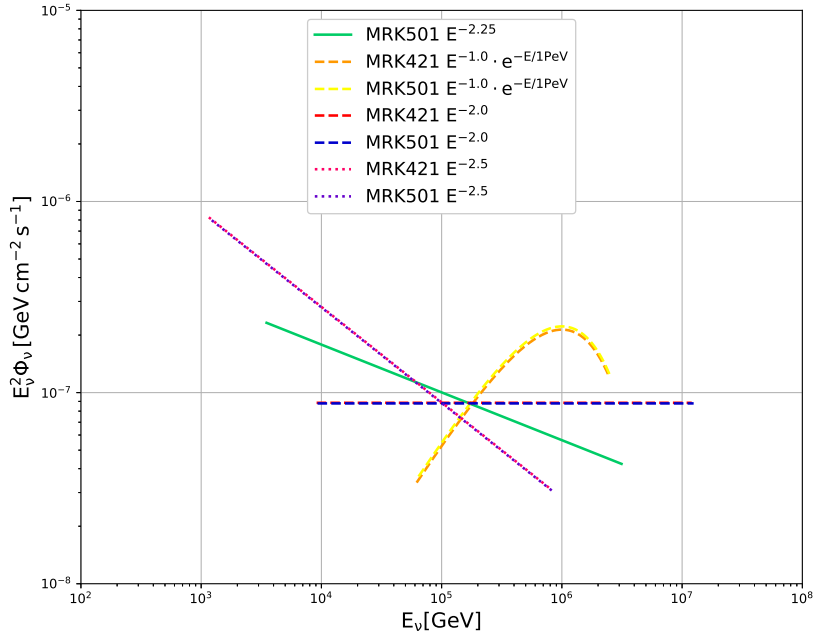


Figure 29: Neutrino energy flux sensitivities at 90% C.L. obtained in the analysis with  $E^{-1.0} \exp(-E/1\text{PeV})$ ,  $E^{-2.0}$ ,  $E^{-2.5}$ ,  $E^{-2.25}$  (this for Mrk 501 only) neutrino energy spectra. Obtained for the long case with sensitivity fluxes for optimum  $\Lambda$  values for each spectrum.

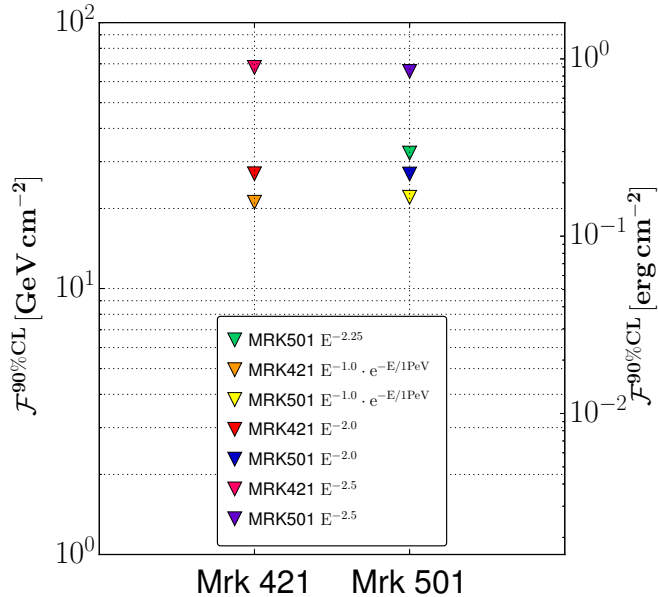


Figure 30: Neutrino fluence sensitivities for long case at 90% C.L. obtained in the analysis with  $E^{-1.0} \exp(-E/1\text{PeV})$ ,  $E^{-2.0}$ ,  $E^{-2.5}$ ,  $E^{-2.25}$  (this for Mrk 501 only) neutrino energy spectra. Obtained for the long case with sensitivity fluxes for optimum  $\Lambda$  values for each spectrum.

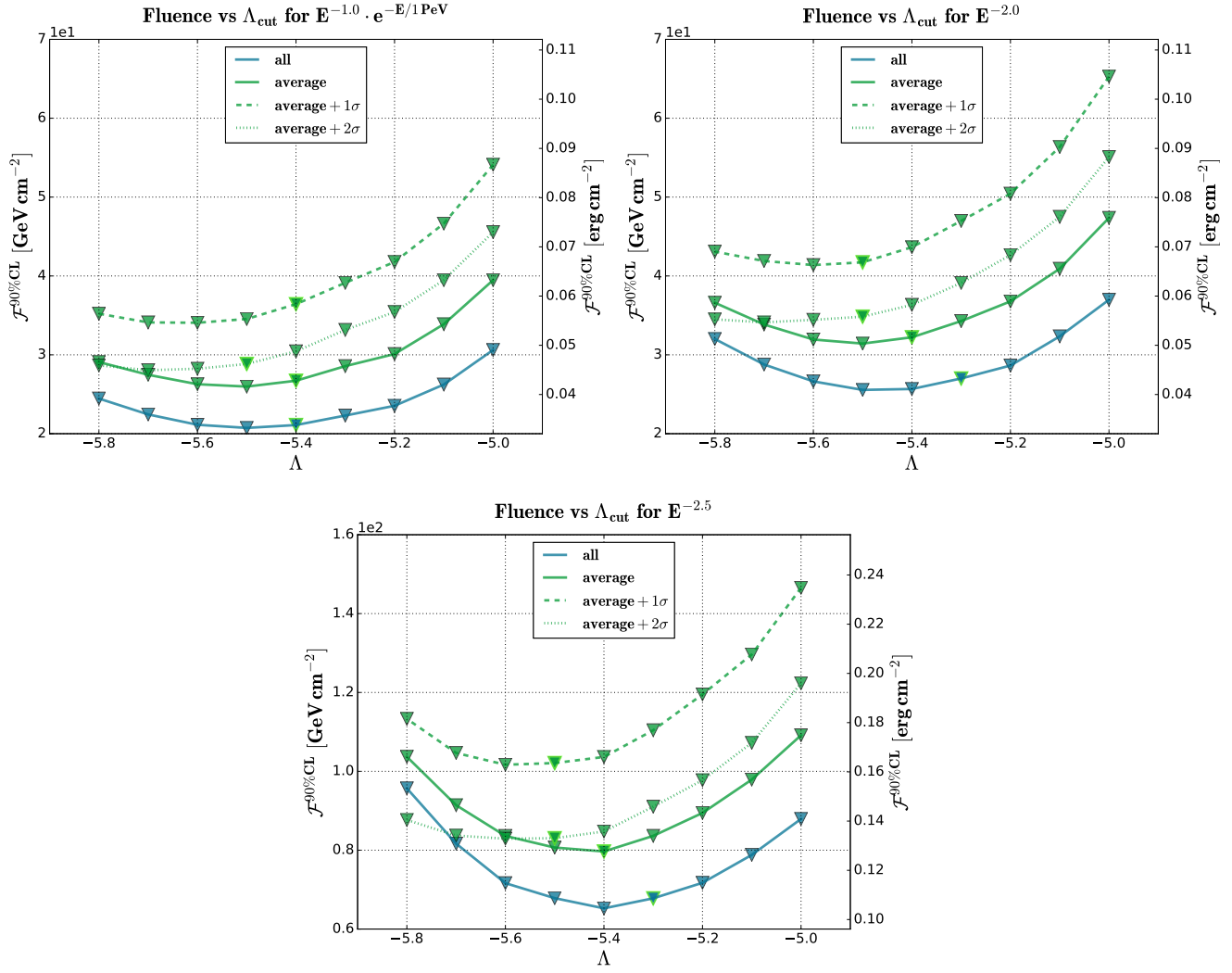


Figure 31: Neutrino fluence sensitivities at 90% C.L. vs  $\Lambda$  for Mrk 421 for different peak selection thresholds. *Upper left panel:*  $E^{-1.0} \exp(-E/1\text{PeV})$ . *Upper right panel:*  $E^{-2.0}$ . *Lower panel:*  $E^{-2.5}$ . Light green color circles represent the sensitivities derived with  $DF^{90\% \text{CL}}$  of optimum  $\Lambda$  values.

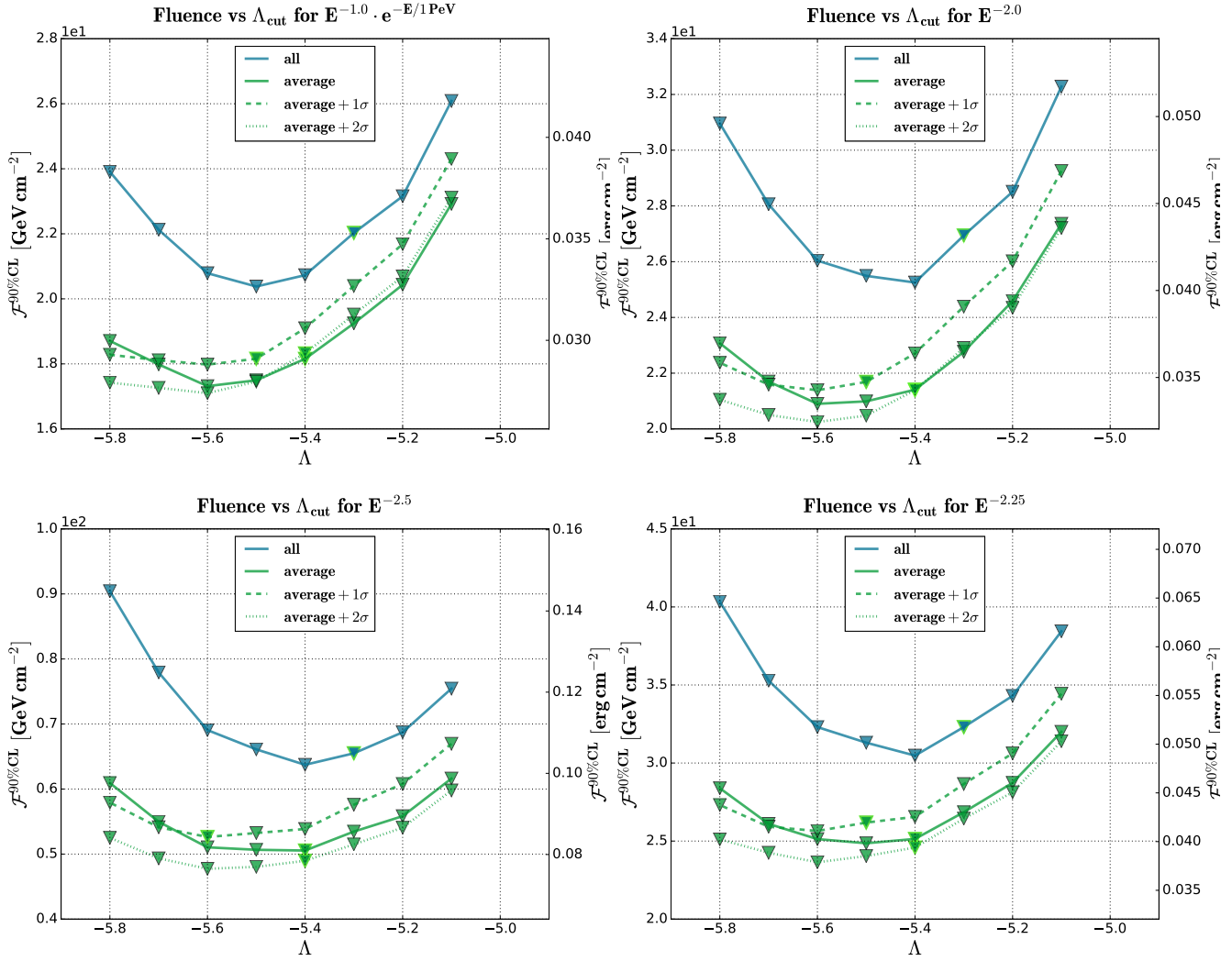


Figure 32: Neutrino fluence sensitivities at 90% C.L. vs  $\Lambda$  for Mrk 501 for different peak selection thresholds. *Upper left panel:*  $E^{-1.0} \exp(-E/1\text{PeV})$ . *Upper right panel:*  $E^{-2.0}$ . *Lower left panel:*  $E^{-2.5}$ . *Lower right panel:*  $E^{-2.25}$ . Light green color circles represent the sensitivities derived with  $DF^{90\%CL}$  of optimum  $\Lambda$  values.

## Conclusion Intermediate

This is imtermediate conclusion for the period HAWC 2014-2016 analysed.

- Conclusion on thresholds:

- Sensitivity fluxes comparison for several thresholds show that the long case provides the best option;
- Sensitivity fluences comparison for several thresholds shows that the short cases provide a better option than the long case for Mrk 501, especially with *average flux* +  $2\sigma$  threshold. From all of the short case thresholds, the *average flux* +  $2\sigma$  provides the best option for Mrk 501 and for Mrk 421 (if *average flux* threshold not taking into account) and thus can be taken into account alone in future analysis.

- Cuts:

- In the analysis, the 9  $\Lambda$  parameters in the range [-5.8;-5.0] with step=0.1 has been considered. This range was sufficient out of the full range of 13  $\Lambda$  [-6.0;-4.8] which could be possible to be taken into account. Because of the fact of vast decrease of discovery fluxes outside of defined 9  $\Lambda$  range and evidence of more stability of background time PDF in this range. As have been seen throughout the analysis, this number even can be shortened to a 7  $\Lambda$  parameters instead of 9, because  $\Lambda > -5.7$  and  $\Lambda > -5.7$  all show worse discovery fluxes, MPDs than  $\Lambda < -5.6$ . Therefore, usage of 7  $\Lambda$  parameters in the range [-5.6;-5.0] are rather sufficient for future extend of this analysis.

## 10 Analysis updates: HAWC 2014-2017

In this section the analysis updates w.r.t. new HAWC light curve data has been presented. The new HAWC data extends the analysis up to 31-th December, 2017. The procedure for this period remains the same with one important exception: the Bayesian Blocks (see Sec. 10.1) now have been applied directly to raw-data light curves provided from HAWC. Previously, we used flare states blocks from the paper [1]. For more details about the Bayesian Blocks application see Sec. 10.1. Also, for this period from the variety of peak selection thresholds like *average flux*, *average flux + 1 $\sigma$* , *average flux + 2 $\sigma$* , the only *average flux + 2 $\sigma$*  has been saved as concluded in the intermediate conclusions (see Sec. 9). Also, the range of 9  $\Lambda$  parameters used in the previous analysis has been shortened in new analysis to 7 from [-5.8;-5.0] to [-5.6;-5.0] due to sufficiency as concluded in intermediate conslusions (see Sec. 9).

### 10.1 Bayesian Blocks

The signal time PDF is assumed to have a square shape. The precise shape of the signal time PDF can be extracted directly for the  $\gamma$ -ray LC assuming the proportionality between the  $\gamma$ -ray and the  $\nu$  fluxes.

The Bayesian blocks algorithm [17] can be applied to detect and characterize signals in noisy time series. If a LC is variable, the Bayesian blocks can be used to find an optimal data segmentation into regions that are well represented by a constant flux, within the statistical uncertainties. The Bayesian analysis helps to identify changes between flux state via finding change points at the transition from one flux state to the next.

In the HAWC 17-months analysis [1] the Bayesian blocks algorithm is used to identify the distinct flux states for Mrk 421 and Mrk 501 and the resulting distinct fluxes have been released in tabular form. In order to properly use such flare states information in the analysis, the 1-day binning was additionally applied (see Fig. 6). In the current analysis, the only available data is the raw-data LCs but not flare states blocks; therefore, the Bayesian Blocks has to be done with the new HAWC data which extends the analysis up to 31-st December, 2017. In order to find the change points at the transition from one flux state to the next, in [1] the so-called point measurements fitness function for the Bayesian blocks algorithm (Sec. 3.3 in [17]) has been adopted and later applied to the daily flux data points. In this analysis, the Bayesian blocks algorithm has been implemented according to the procedure in [1]. Also, some functions have been adopted from the HAWC Public Datasets dedicated to the HAWC 17-months analysis [1].

The Bayesian blocks algorithm requires the initial choice of a Bayesian prior, called  $ncp_{prior}$ , for the probability of finding a new change of flux states, where  $\gamma = \exp(-ncp_{prior})$  is the constant factor defining a priori how much less likely it is to find  $k+1$  change points instead of  $k$  points [1]. In the HAWC 17-months analysis [1] the predetermined 5% false positive probability is used. This value results in a relative frequency of 5% for identifying a change point that is not a true flux state change for each light curve [1]. To fulfill the 5% false positive probability for finding one change point, in [1] the  $ncp_{prior} = 6$  has been adopted from simulations. Same  $ncp_{prior} = 6$  value is used in this analysis. In addition, different  $ncp_{prior}$  values have been tested, and  $ncp_{prior} = 6$  seems to be reasonable (see Fig. 33). As axample, for Mrk 421 it has given almost the same block profile for the first 17 months as from the paper [1].

The Bayesian blocks algorithm with  $ncp_{prior} = 6$  corresponding to a false positive probability of 5% identifies 36 and 30 change points in the light curves shown in Fig. 34, 35 for Mrk 421 and Mrk 501 respectively .

The Bayesian blocks analysis for Mrk 501 returns the negative flux amplitude values for the period of approximately during the last 2 months of 2017 year (see Fig. 35) just after MJD=58063 and for the short period around MJD=57568. Moreover, it gives one single block between that two periods with roughly

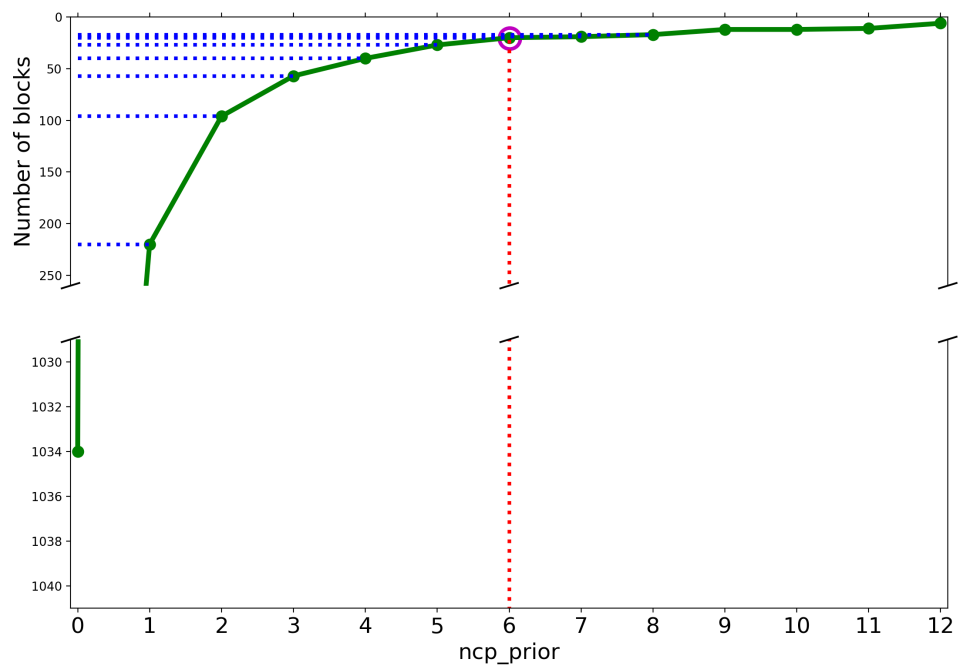
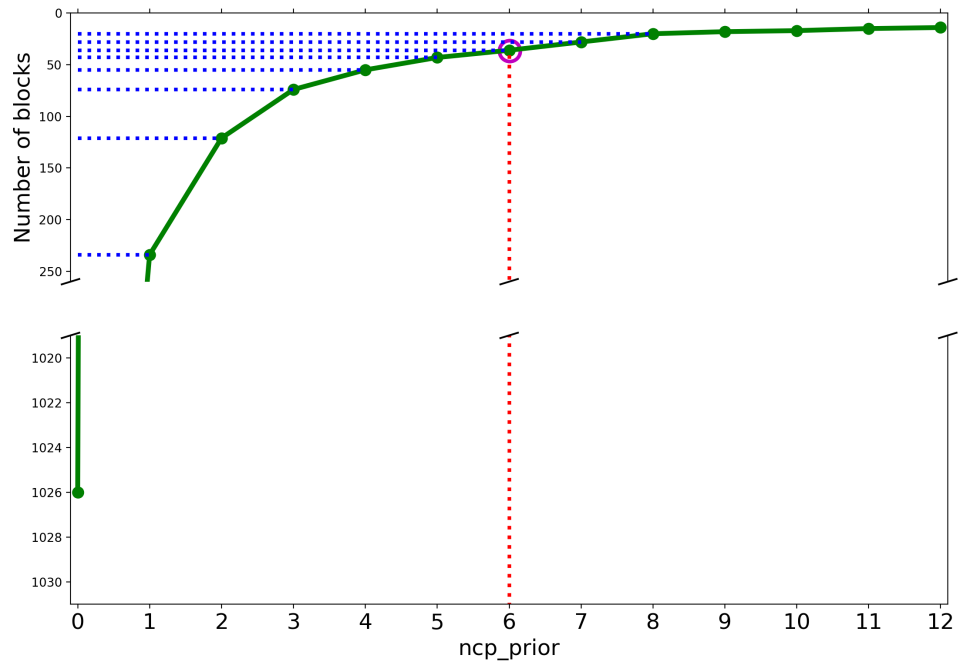


Figure 33: Bayesian blocks vs  $ncp_{prior}$ . *Upper plot:* Mrk 421. *Lower plot:* Mrk 501. The 1026 and 1034 blocks for  $ncp_{prior} = 0$  are the total number of data points (or days of search) available for Mrk 421 and Mrk 501 respectively.

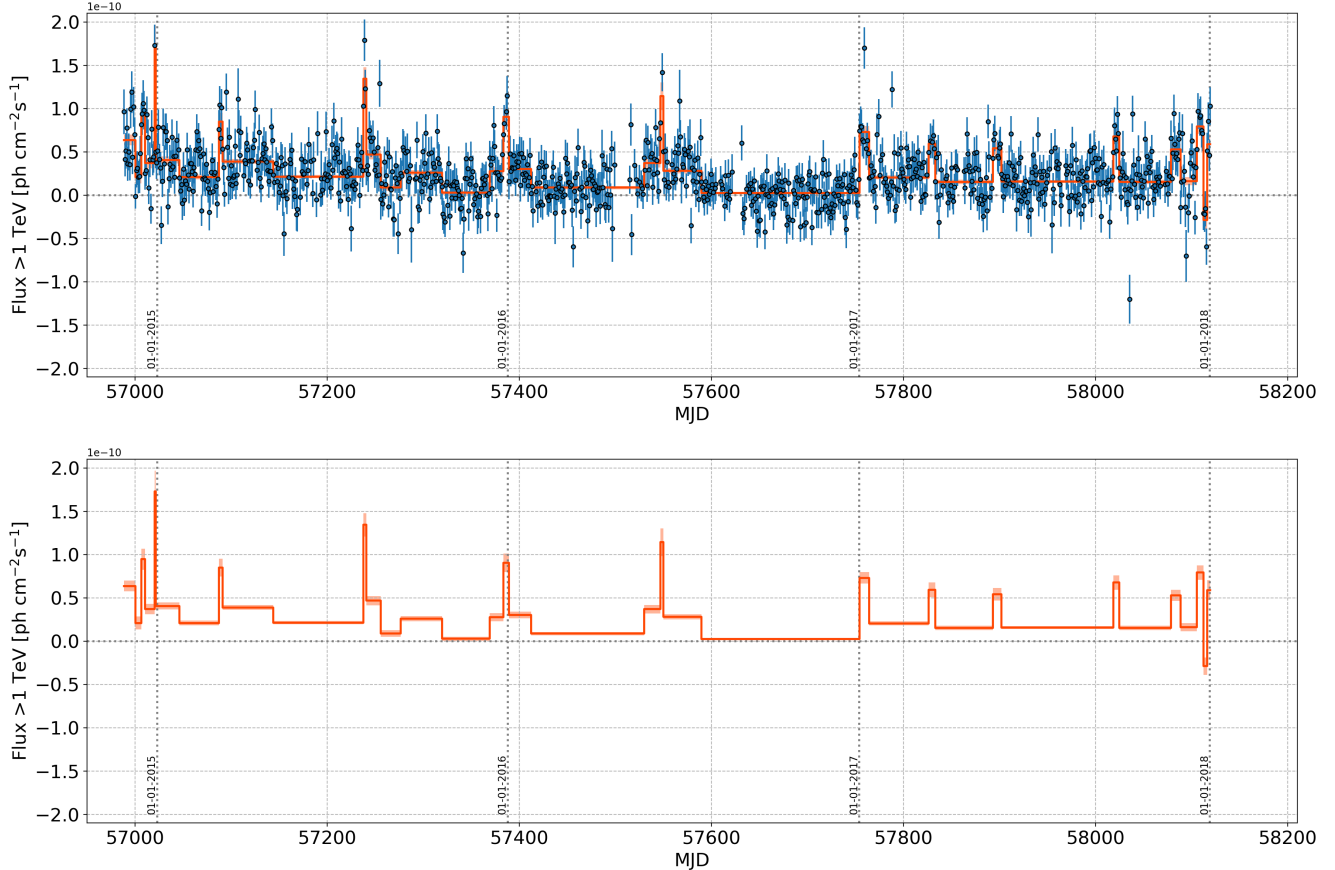


Figure 34: The HAWC daily flux light curve for Mrk 421 for 1026 transits between November 27<sup>th</sup>, 2014 and January 1<sup>st</sup>, 2018. The orange lines show the distinct flux states between change points identified via the Bayesian blocks analysis with a 5% false positive probability and  $n_{cp_{prior}} = 6$ . The orange shaded regions represent the statistical uncertainty of  $1\sigma$  of the flux amplitudes for the periods between two change points. The bottom plot shows the distinct flux states in a separate plot.

500 days of duration and positive flux amplitude but very low w.r.t. any other positive distinct flare state fluxes (around one order of magnitude less) obtained for this source. Such a low value can be treated as zero, and the corresponding block with surrounding blocks having negative values have been together excluded from the analysis. In that case, the Bayesian blocks have been recalculated for Mrk 501, but for a new shorter period from the November 28<sup>th</sup>, 2014 to June 28<sup>th</sup>, 2016 (MJD: 56989-57567).

It is worth noting, that the integrated HAWC data for Mrk 421 and Mrk 501 are best described via a curved spectrum with a photon index  $\Gamma$  and an exponential cut-off at  $E_0$ , but these values are different for 17 months analysis [1] and for the new raw-data provided. For example, the integrated HAWC 17 month data for Mrk 421 and Mrk 501 are best described via a curved spectrum with a photon index  $\Gamma = 2.21$  and an exponential cut-off at  $E_0 = 5.4$  TeV and with a photon index  $\Gamma = 1.6$  and an exponential cut-off at  $E_0 = 5.7$  respectively. In contrast to that, the spectral fits for Mrk 421 and Mrk 501 yield a rather different power-law index  $\Gamma = 2.07$  and an exponential cut-off  $E_0 = 4.53$  TeV and the power-law index  $\Gamma = 1.66$  and an exponential cut-off  $E_0 = 5.76$  TeV respectively.

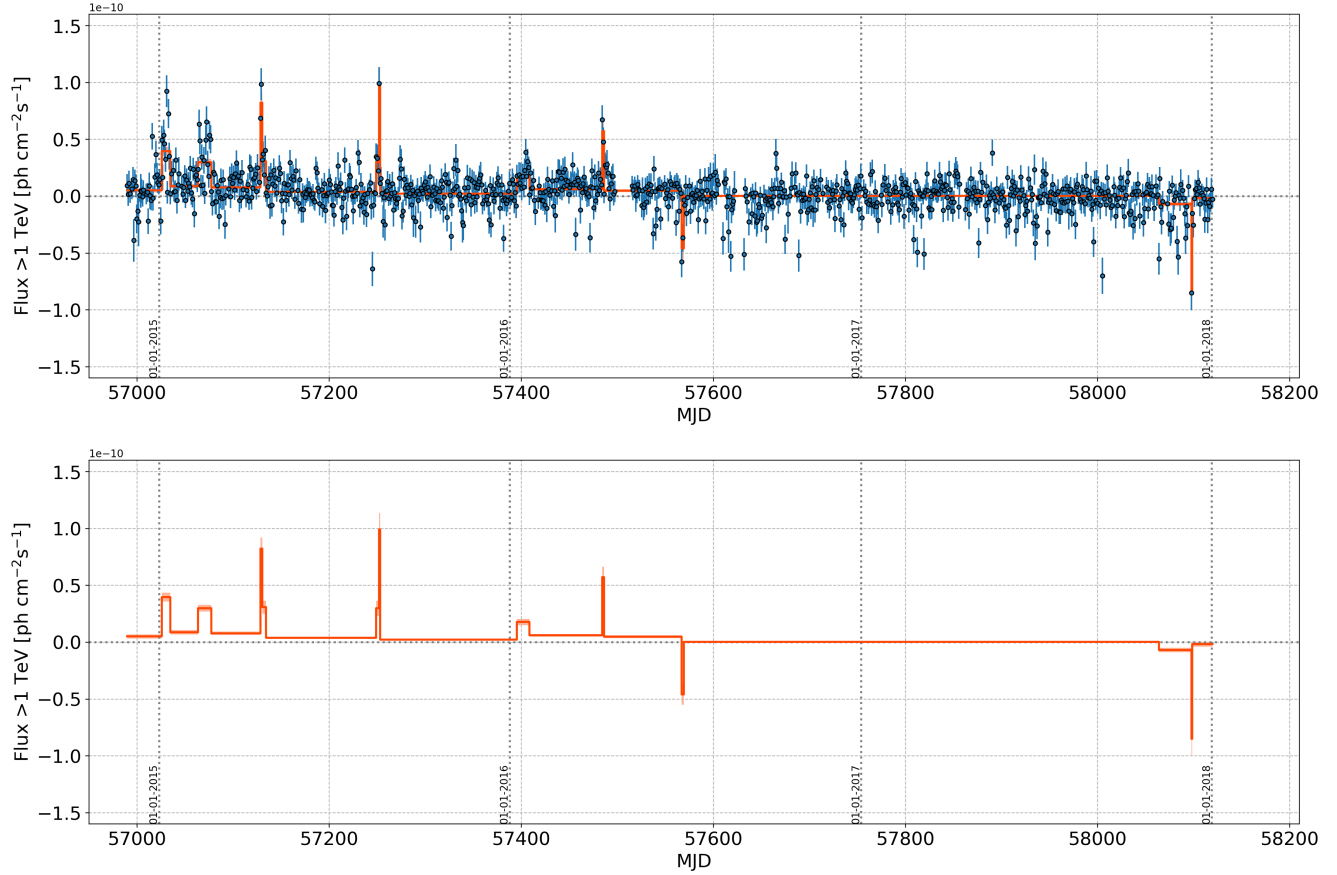


Figure 35: The HAWC daily flux light curve for Mrk 501 for 1034 transits between November 28<sup>th</sup>, 2014 and January 1<sup>st</sup>, 2018. The orange lines show the distinct flux states between change points identified via the Bayesian blocks analysis with a 5% false positive probability and  $n_{cp}_{prior} = 6$ . The orange shaded regions represent the statistical uncertainty of  $1\sigma$  of the flux amplitudes for the periods between two change points. The bottom plot shows the distinct flux states in a separate plot.

## 10.2 Signal time PDF

In this section, the distinct flare states obtained in the analysis and selected as the time PDF profiles for the sources (see Fig. 36, 37) are presented. As mentioned earlier, for this analysis from the variety of peak selection thresholds like *average flux*, *average flux + 1 $\sigma$* , *average flux + 2 $\sigma$* , the only *average flux + 2 $\sigma$*  has been saved being sufficient (see Sec. 9).

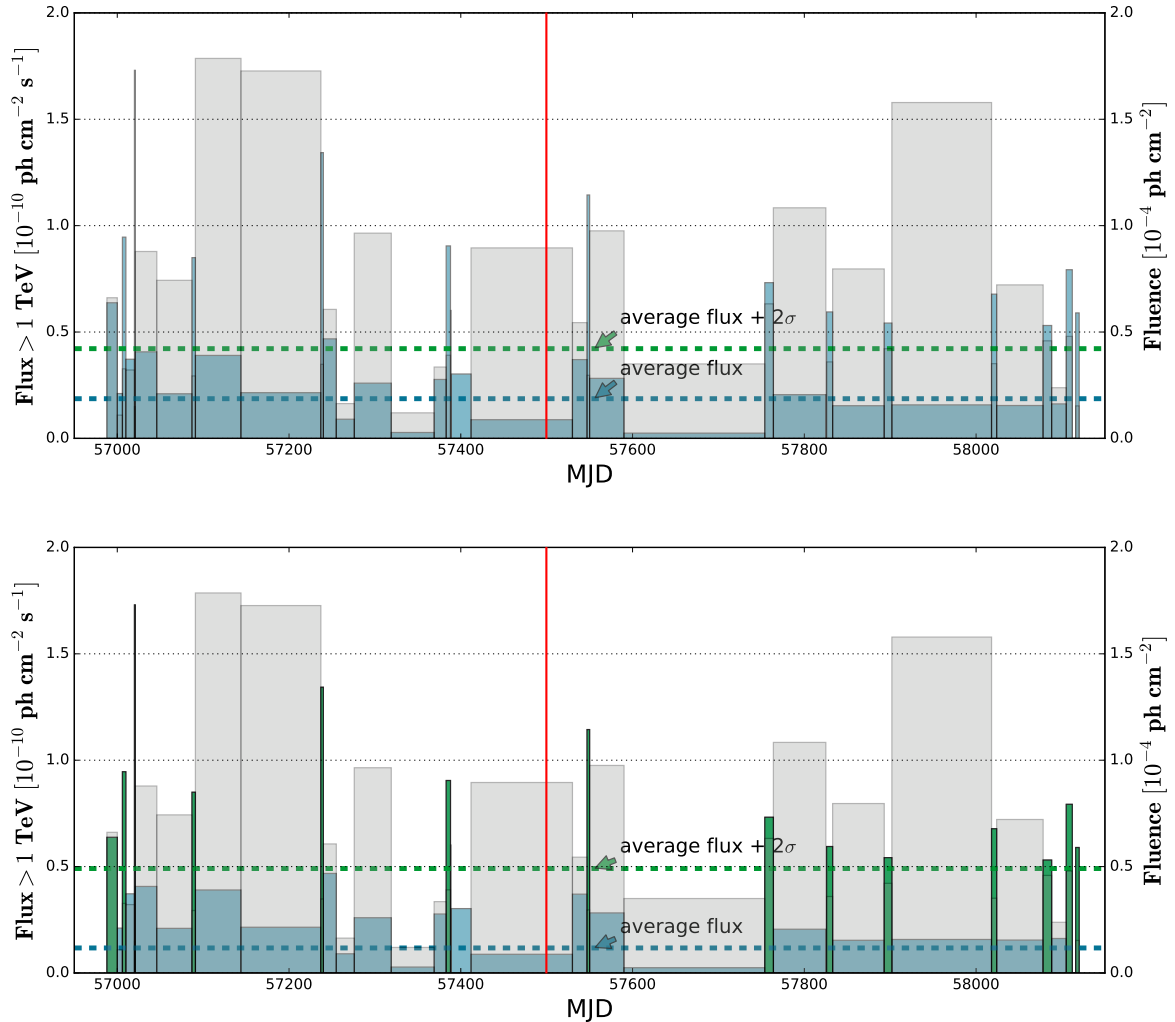


Figure 36: Obtained distinct flare states for Mrk 421 vs threshold. *Upper plot* The long case. *Lower plot* The short case for *average flux + 2 $\sigma$* . The blue dotted line represents the average flux; the green dotted line represents the *average flux + 2 $\sigma$*  peak selection threshold. The left axis represents the units of the flux, the right axis represents the units of the fluences shown as shaded grey areas. The red line represents the edge of the period of interests in the analysis based on HAWC 17 months search [1].

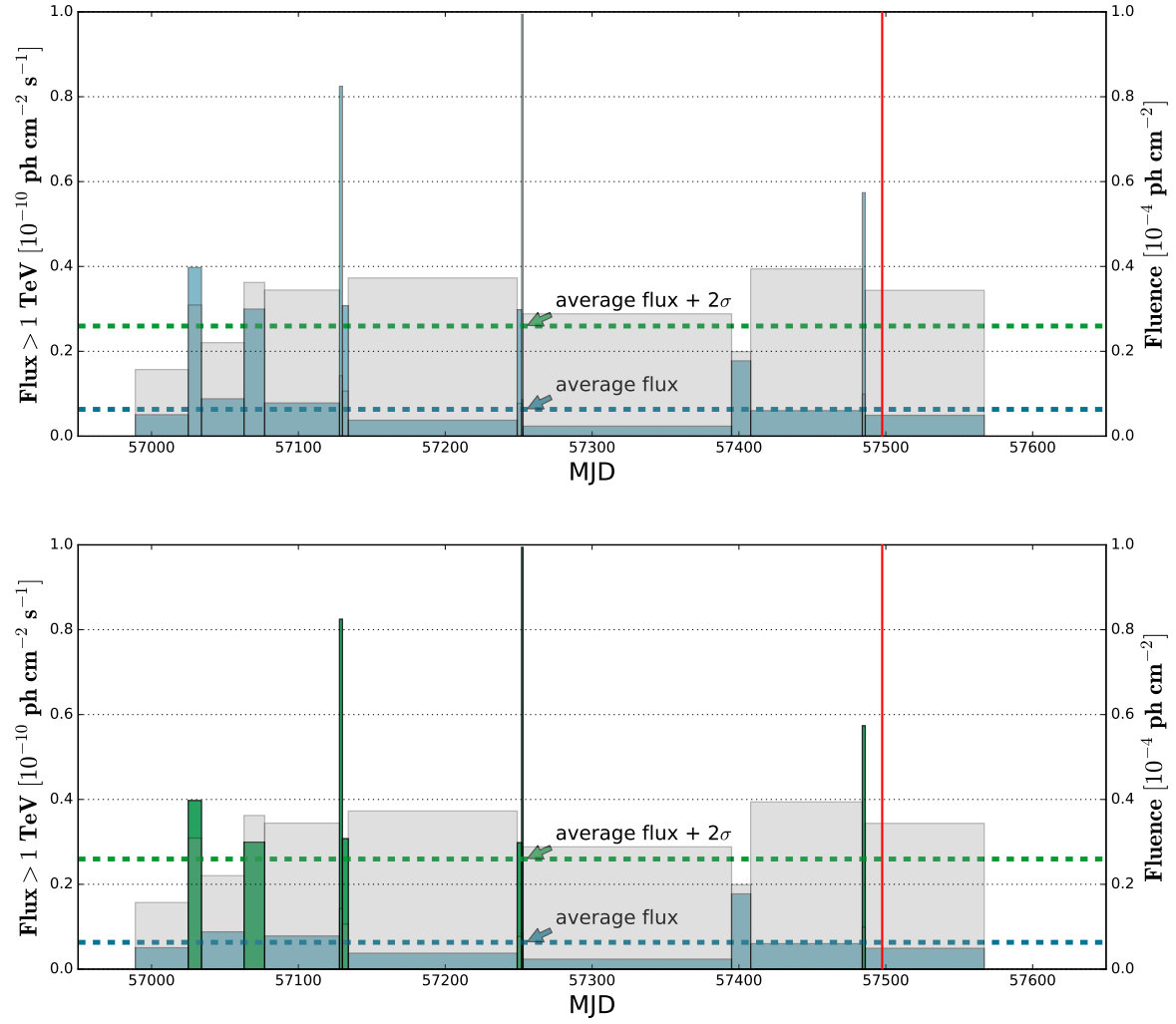


Figure 37: Obtained distinct flare states for Mrk 501 vs threshold. *Upper plot* The long case. *Lower plot* The short case for *average flux +  $2\sigma$* . The blue dotted line represents the average flux; the green dotted line represents the *average flux +  $2\sigma$*  peak selection threshold. The left axis represents the units of the flux, the right axis represents the units of the fluences shown as shaded grey areas. The red line represents the edge of the period of interests in the analysis based on HAWC 17 months search [1].

## 10.3 The new Data set

The selected data set covers the same period of observation as HAWC. The data set selected for the Mrk 421 covers the period from the November 27<sup>th</sup>, 2014 to January 1<sup>st</sup>, 2018 (MJD: 56988-58119) leading to effective detector livetime of 1099.93 days (3.009 years), which doubles the previous search period of 503.7 days (1.379 y). As shown in Sec. 10.1, such period has been cutted for Mrk 501 due to some period which was not possible to be defined as having distinct flare states. Thus, the data set selected for the Mrk 501 covers the period from the November 28<sup>th</sup>, 2014 to June 28<sup>th</sup>, 2016 (MJD: 56989-57567) leading to effective detector livetime of 561.55 days (1.537 years), which increases search period by  $\sim 10\%$  w.r.t. the previous 503.7 days (1.379 y).

The search relies on track-like event signatures, so only CC interactions of muon neutrinos are considered.

The DATA and Monte Carlo (MC) files were obtained from the following folders:

The DATA files:

- /hpss/in2p3.fr/group/antares/SeaTray/prod\_2018-02-01/Line12/sea/ [HPSS]

The MC files  $\nu|\mu$ :

- /hpss/in2p3.fr/group/antares/mc/rbr/v4/reco/final/AntDST/ [HPSS]

Runs are selected if the conditions below are fulfilled:

- QualityBasic  $>= 1$
- SCAN  $=! 1$
- Sparking  $=! 1$  (Addition sparking runs were observed and removed)

The MC production is selected to be complete, i.e. MUPAGE and all track-like (a)numu files were available. Besides, since not all DATA runs have a corresponding MC runs and MC complete runs give livetime less than those for DATA runs, rescaling of incomplete MC is required. Thus, rescale of available MC livetime up to livetime in DATA is applied. It is considered as an additional weight on the MC in order to take into account the livetime difference and done on a year-to-year basis  $LT_{year}^{DATA}/LT_{year}^{MC}$ .

Table 7: Effective livetime vs MC complete period

Source	Effective LT	MC complete
Mrk 421	1099.93 d (3.009 y)	993.83 d (2.721 y)
Mrk 501	561.55 d (1.537 y)	462.13 d (1.265 y)
Previous	503.70 d (1.379 y)	332.80 d (0.911 y)

Since the new reprocessed data prod\_2018-02-01 inherently had no pre-selection cuts as it happened with Reprocessing\_2016\_05 used in the previous analysis, then no global cuts applied on the whole period as it has been forcedly done in the previous analysis (see Sec. 2 for more details). So, no preliminary cuts on  $\Lambda$ ,  $\beta$  and  $\cos(\theta)$  applied.

### 10.3.1 DATA/MC

In order to test the goodness of the ANTARES MC production for the period of the analysis, it is compared with measured data. The DATA/MC comparison plots for the energy estimator nhit and for the  $\Lambda$ ,  $\cos(\theta)$ ,  $\beta$  cuts with non-normalized distributions and with indicated MC contributions (up-going atmospheric neutrinos and mis-reconstructed atmospheric muons) can be seen in Fig. 38- 41.

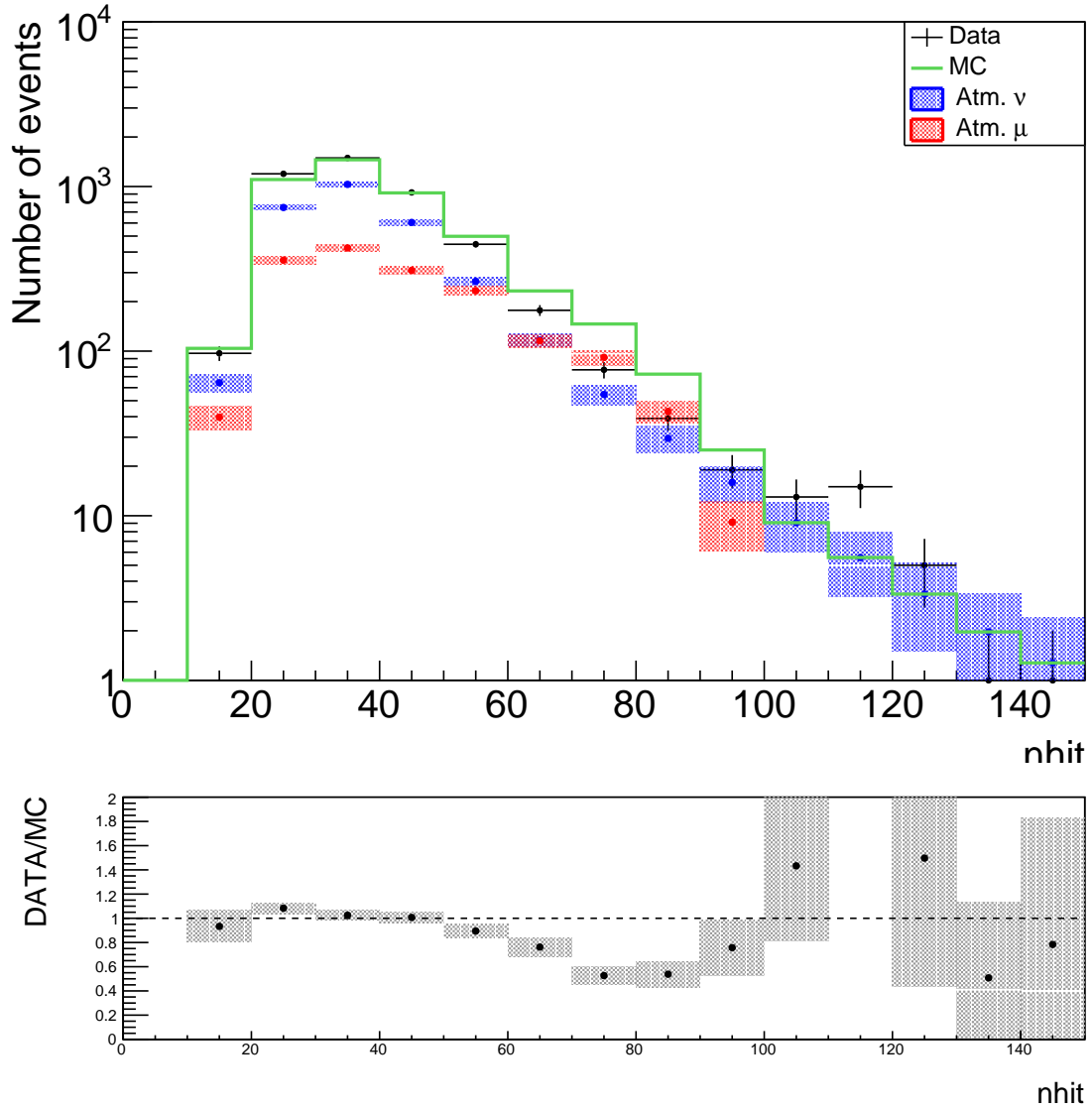


Figure 38: Comparison of the data with MC simulations as a function of the number of hits nhit. The figure corresponds to the energy PDF distribution after applying the cut on the quality parameter  $\Lambda > -5.4$ . The blue dots show the simulated up-going atmospheric neutrinos with the errors as a dashed area, the red dots show the mis-reconstructed atmospheric muons with the errors as a dashed area, the green line is the sum of both contributions, and the black crosses show the data. The bottom plot shows the data to MC ratio, where the number of MC events is the sum of neutrinos and atmospheric muons.

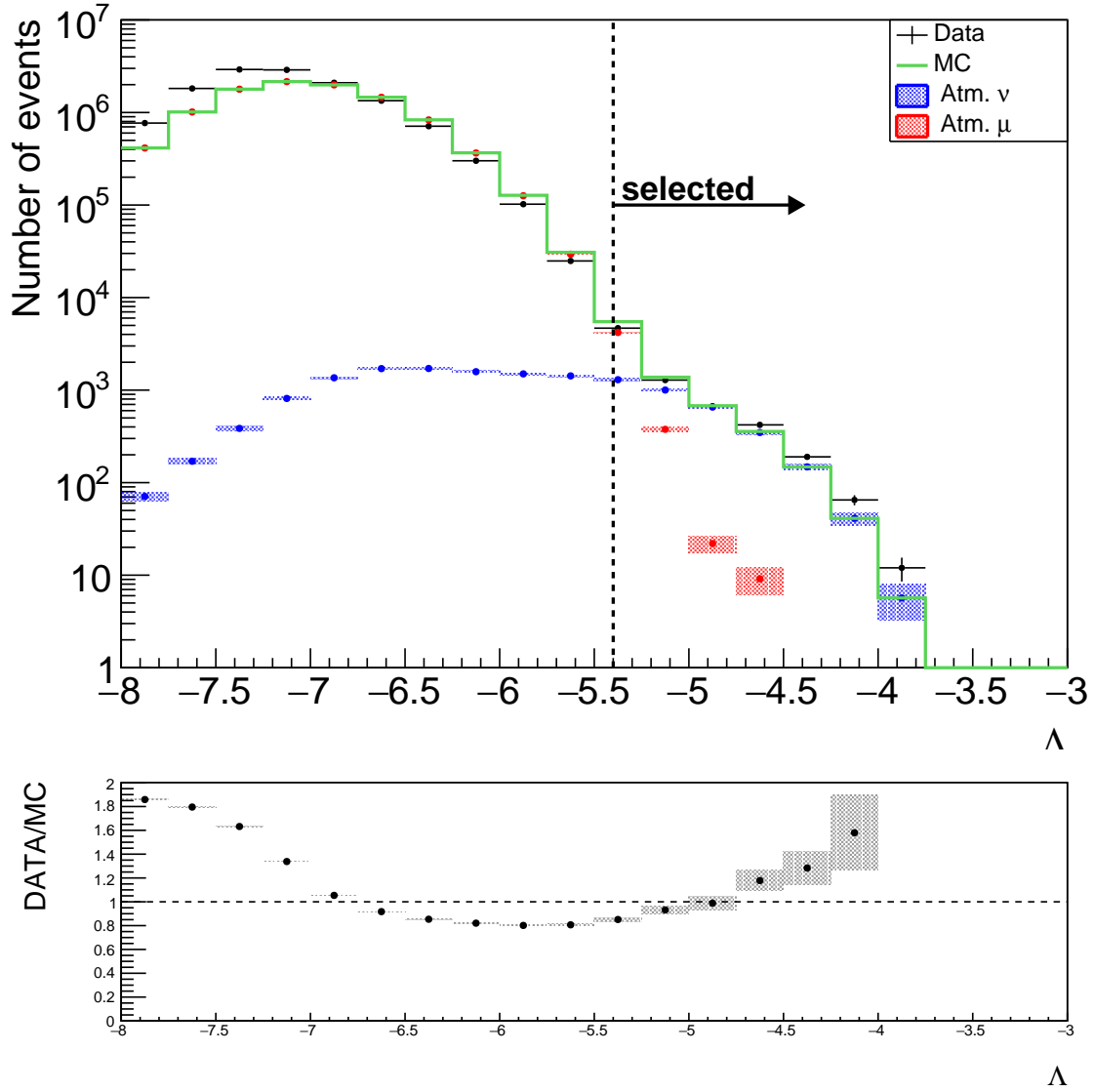


Figure 39: Comparison of the data with MC simulations as a function of the quality parameter of the reconstruction of muon track  $\Lambda$ . The figure corresponds to the event distribution after applying the cut on the reconstructed cosine of the zenith angle  $\cos(\theta) > -0.1$  and the cut on the error on the direction of the reconstructed muon track  $\beta < 1.0^\circ$ . The blue dots show the simulated up-going atmospheric neutrinos with the errors as a dashed area, the red dots show the mis-reconstructed atmospheric muons with the errors as a dashed area, the green line is the sum of both contributions, and the black crosses show the data. The vertical dotted line with the arrow shows where the optimized selection cuts stand for the various tested spectra of both sources. The bottom plot shows the data to MC ratio, where the number of MC events is the sum of neutrinos and atmospheric muons.

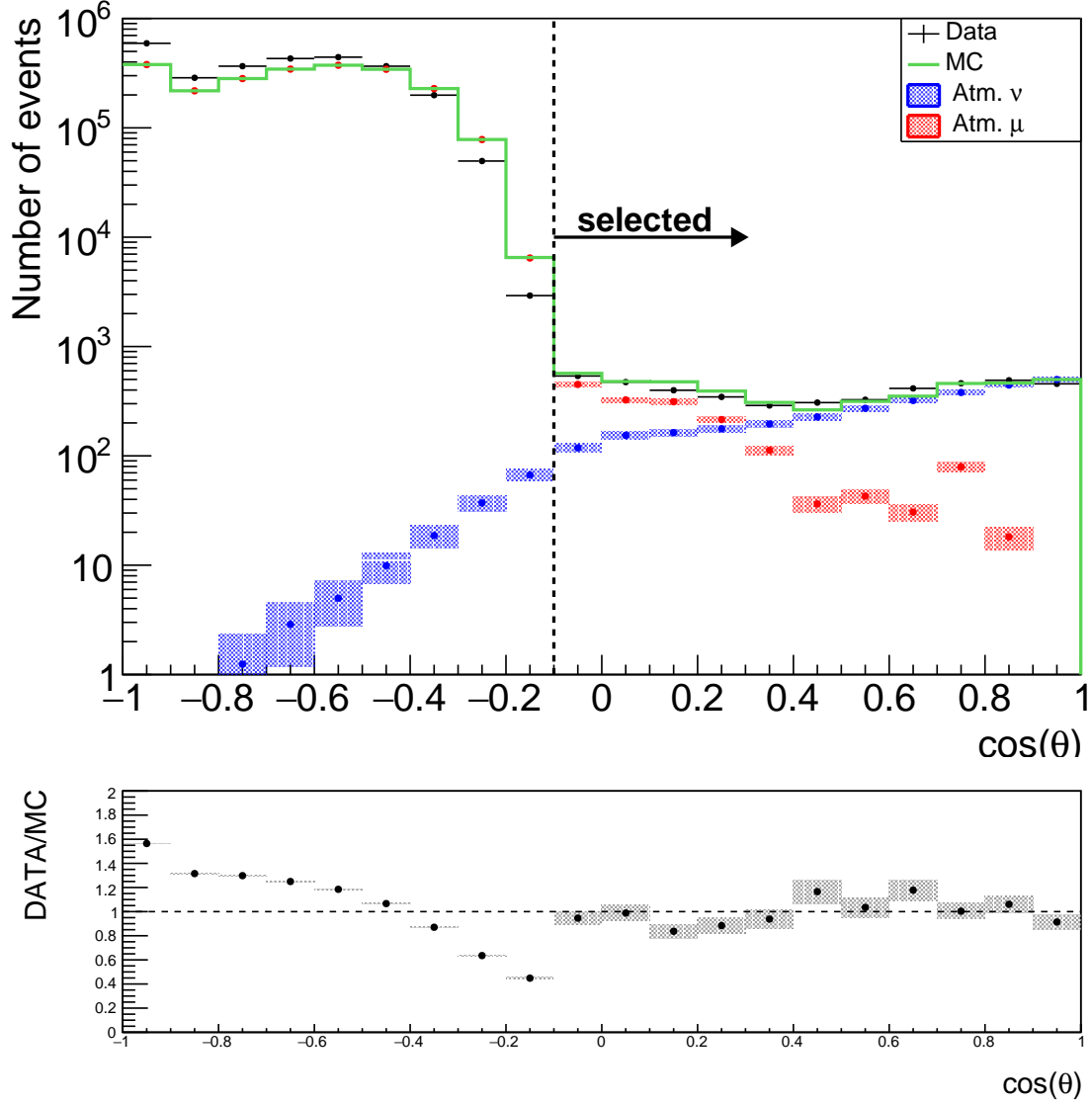


Figure 40: Comparison of the data with MC simulations as a function of the reconstructed cosine of the zenith angle  $\cos(\theta)$ . The figure corresponds to the event distribution after applying the cut on the quality parameter  $\Lambda > -5.4$  and the cut on the error on the direction of the reconstructed muon track  $\beta < 1.0^\circ$ . The blue dots show the simulated up-going atmospheric neutrinos with the errors as a dashed area, the red dots show the mis-reconstructed atmospheric muons with the errors as a dashed area, the green line is the sum of both contributions, and the black crosses show the data. The vertical dotted line with the arrow shows the selected  $\cos(\theta) > -0.1$  cut. The bottom plot shows the data to MC ratio, where the number of MC events is the sum of neutrinos and atmospheric muons.

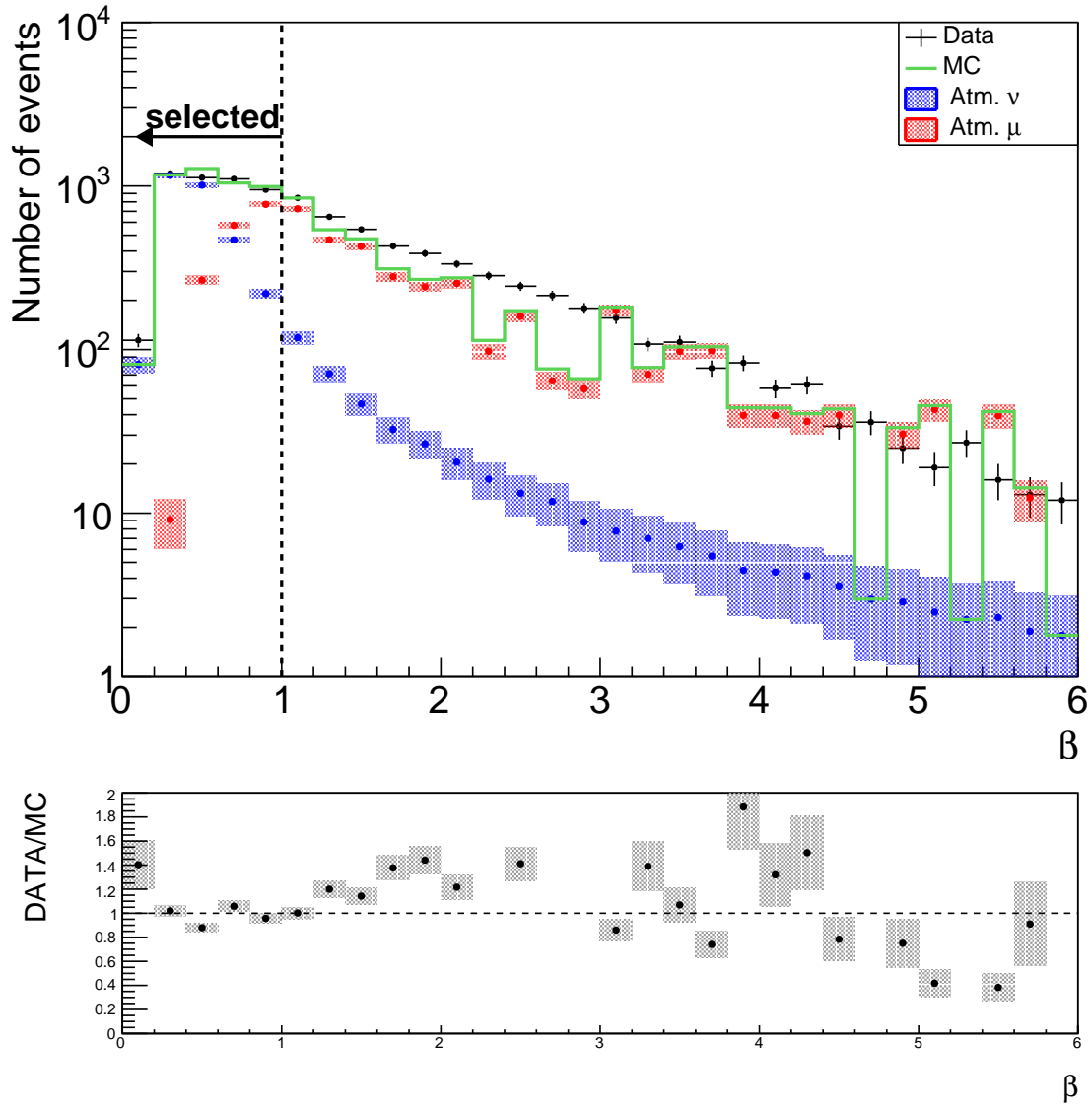


Figure 41: Comparison of the data with MC simulations as a function of the estimated error on the direction of the reconstructed muon track  $\beta$ . The figure corresponds to the event distribution after applying the cut on zenith angle  $\cos(\theta) > -0.1$  and the cut on the quality parameter  $\Lambda > -5.4$ . The blue dots show the simulated up-going atmospheric neutrinos with the errors as a dashed area, the red dots show the mis-reconstructed atmospheric muons with the errors as a dashed area, the green line is the sum of both contributions, and the black crosses show the data. The vertical dotted line with the arrow shows the selected  $\beta < 1.0^\circ$  cut. The bottom plot shows the data to MC ratio, where the number of MC events is the sum of neutrinos and atmospheric muons.

## 10.4 Results

In this section, the new results of the analysis for Mrk 421 and Mrk 501 discussed. As concluded in 9, the parameters selected for this analysis are:

- Considered spectra
  - $E^{-\gamma} \cdot \exp(-E/E_{cut})$  with  $\gamma = 1.0$  and cutoff at 1 PeV for both sources;
  - $E^{-\gamma}$  with  $\gamma = 2.0$  for both sources;
  - $E^{-\gamma}$  with  $\gamma = 2.5$  for both sources;
  - $E^{-\gamma}$  with  $\gamma = 2.25$  for Mrk 501 only.
- Considered flares:
  - all flare blocks (long case);
  - higher *average flux* +  $2\sigma$  (short case).
- Considered cuts:
  - 7 instead of 9 track reconstruction quality parameters  $\Lambda$ :  $\Lambda > -5.6; \dots; -5.0$ ;
  - 1 cut on error on the reconstructed zenith  $\cos(\theta)$ :  $\cos(\theta) > -0.1$ ;
  - 1 cut on angular error estimate  $\beta$ :  $\beta < 1.0$ .

### 10.4.1 Discovery signal

The number of signal events  $N_S^{3\sigma}, N_S^{5\sigma}$  required for  $3\sigma$  evidence or  $5\sigma$  discovery give the minimum flux that could give an evidence at  $3\sigma$  level or  $5\sigma$  discovery in 50% of the trials. The Fig. 42, 43 represent  $N_S^{3\sigma}$  and  $N_S^{5\sigma}$  versus  $\Lambda$  respectively. It can bee seen from the plots, that the short case with *average flux* +  $2\sigma$  threshold requires 2 times less neutrino events for discovery.

The conversion of  $N_S$  into the equivalent source flux is done through the acceptance of the detector (see Sec. 8.2). The acceptance calculation procedure has been discussed in Sec. 8.2. The new acceptance plots is discussed in Sec. 10.4.2.

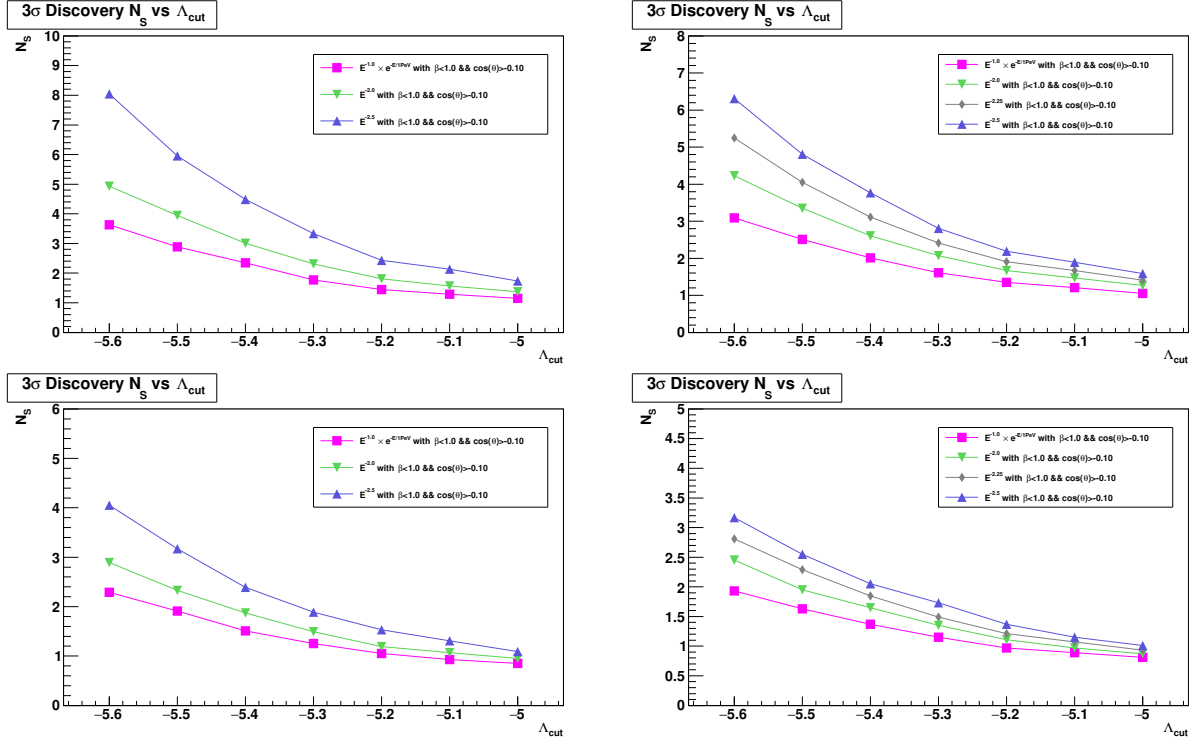


Figure 42: Discovery power at  $3\sigma$  level. *Left panel*: Mrk 421 *Right panel*: Mrk 501. *Upper panel* all flares. *Lower panel* short flares with *average flux +  $2\sigma$*  threshold.

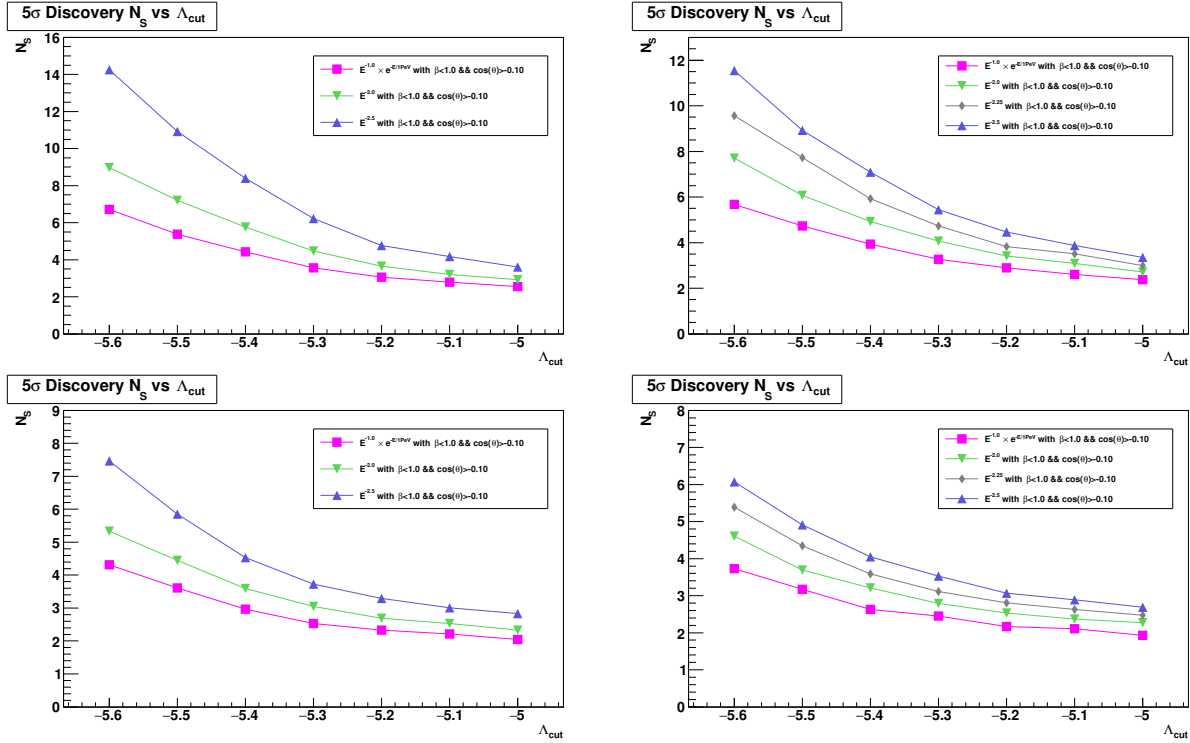


Figure 43: Discovery power at  $5\sigma$  level. *Left panel*: Mrk 421 *Right panel*: Mrk 501. *Upper panel* all flares. *Lower panel* short flares with *average flux +  $2\sigma$*  threshold.

### 10.4.2 Acceptance

The conversion of  $N_S$  into the equivalent source flux is done through the acceptance of the detector. The comparison of acceptances for Mrk 421 and Mrk 501 can be seen in Fig. 44, 45 respectively.

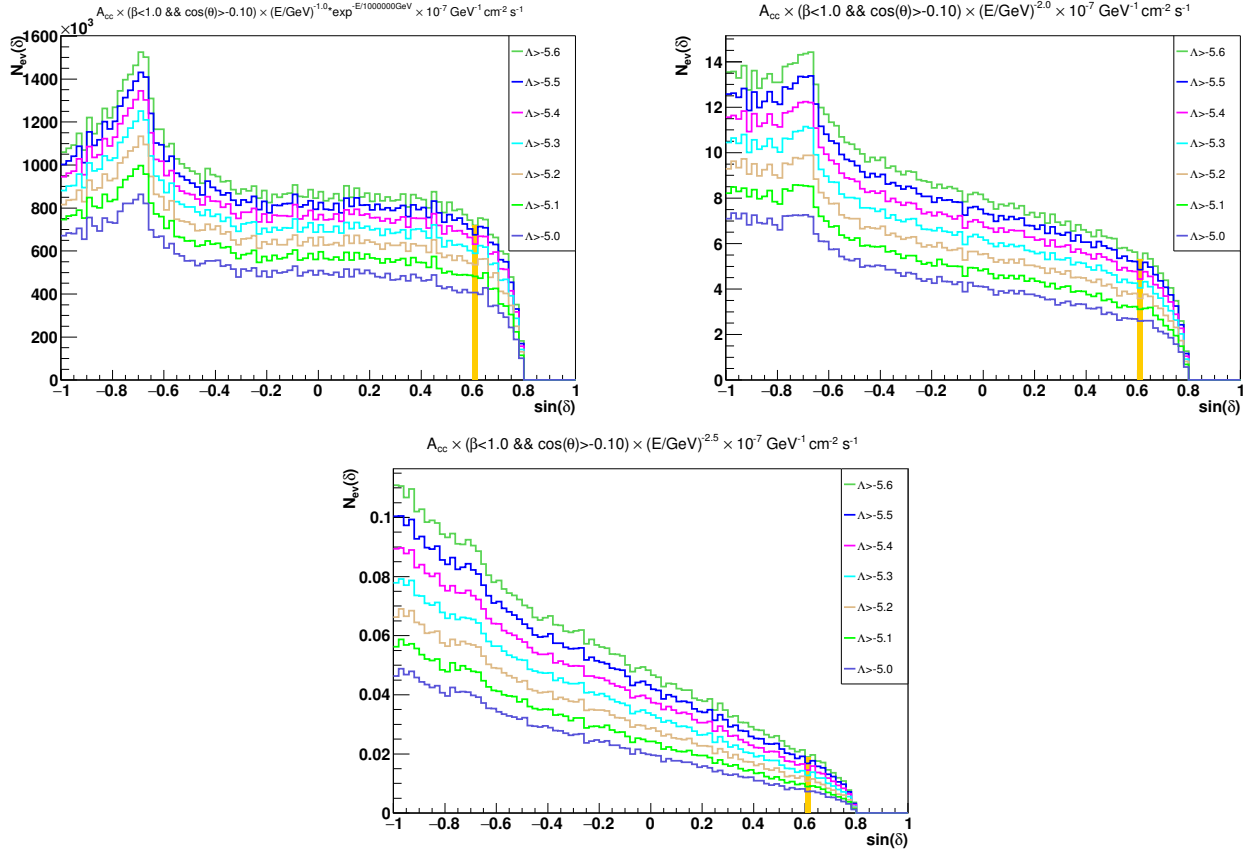


Figure 44: Examples of acceptance for Mrk 421 as a function of the source declination for the several  $\Lambda$  cuts [with  $\beta < 1.0$  and  $\cos(\theta) > -0.1$ ] with a flux normalization factor of  $\Phi_0 = 10^{-7} \text{ GeV}^{-1} \text{ cm}^{-2} \text{ s}^{-1}$  in  $N_{ev} = A_{cc} \times \Phi_0$  magnitudes. The period used: November 27<sup>th</sup>, 2014 - January 1<sup>st</sup>, 2018. *Upper left panel:*  $E^{-1.0} \exp(-E/1\text{PeV})$ . *Upper right panel:*  $E^{-2.0}$ . *Lower panel:*  $E^{-2.5}$ . Orange color represents the bins of the source declination.

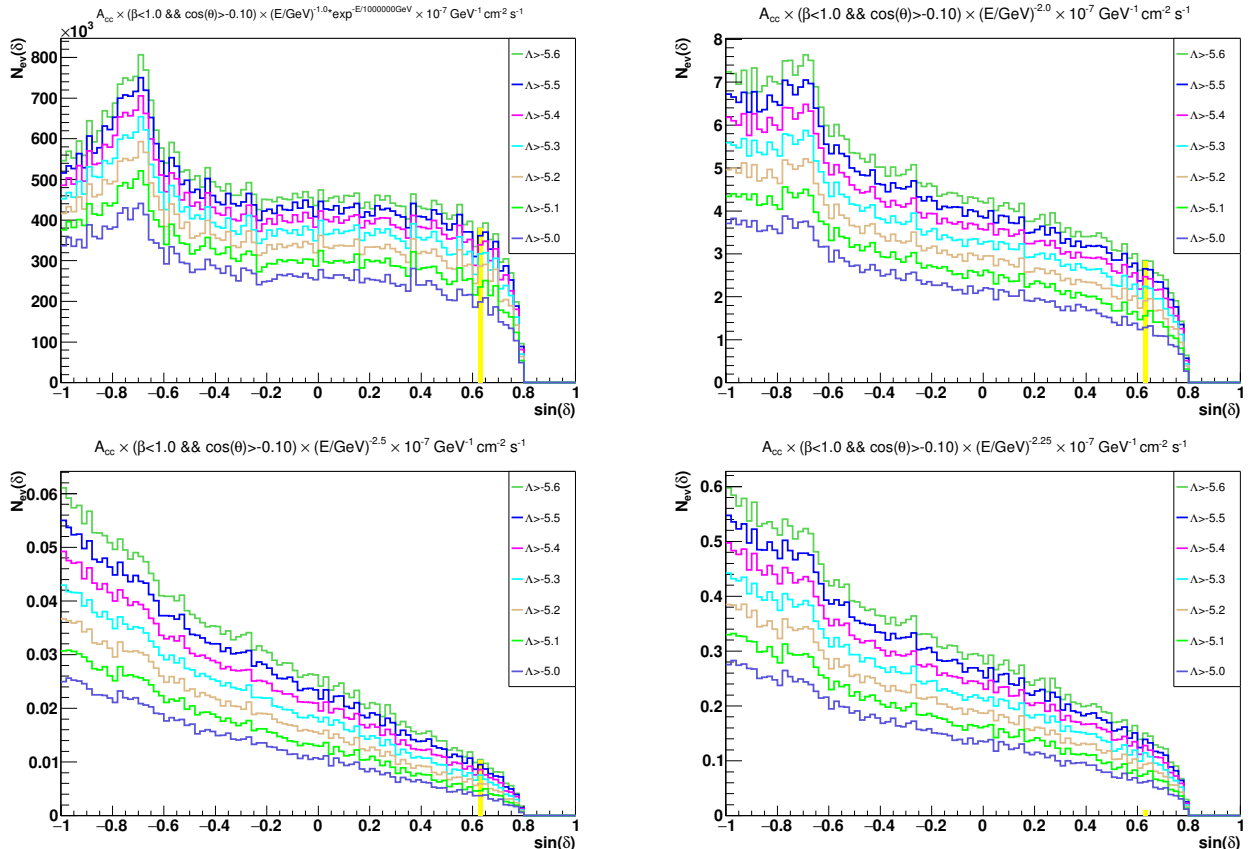


Figure 45: Examples of acceptance for Mrk 501 as a function of the source declination for the several  $\Lambda$  cuts [with  $\beta < 1.0$  and  $\cos(\theta) > -0.1$ ] with a flux normalization factor of  $\Phi_0 = 10^{-7} \text{ GeV}^{-1} \text{cm}^{-2} \text{s}^{-1}$  in  $N_{ev} = A_{cc} \times \Phi_0$  magnitudes. The period used: November 28<sup>th</sup>, 2014 - June 28<sup>th</sup>, 2016. *Upper left panel:*  $E^{-1.0} \exp(-E/1\text{PeV})$ . *Upper right panel:*  $E^{-2.0}$ . *Lower left panel:*  $E^{-2.5}$ . *Lower right panel:*  $E^{-2.25}$ . Yellow color represents the bins of the source declination.

### 10.4.3 Discovery fluxes

In this section the discovery fluxes obtained in analysis for all spectra with all flare states selected (long case) and with only flare states above *average flux* +  $2\sigma$  threshold selected (short case) are discussed.

Discovery flux level  $DF_{5\sigma}^{50\%CL}$  is the flux required to have a test statistic TS over  $TS_{5\sigma}$  in 50% of trials. Discovery fluxes  $DF_{3\sigma}^{50\%CL}$ ,  $DF_{5\sigma}^{50\%CL}$  versus  $\Lambda$  for cut on the reconstructed zenith  $\cos(\theta) > -0.1$  and cases of all flares and only peaks are shown in Fig. 46, 47. Similarly to  $3\sigma/5\sigma$  discovery fluxes, the discovery flux level  $DF_{Median}^{90\%CL}$  is defined as the sensitivity flux required to have a test statistic TS over the median of the background distribution  $TS_{Median}$  in 90% of the trials. The sensitivity flux places the upper limit on fluxes at 90% Confidence Level (C.L.). In the absence of a signal, it is used for 90% C.L. sensitivity calculations.

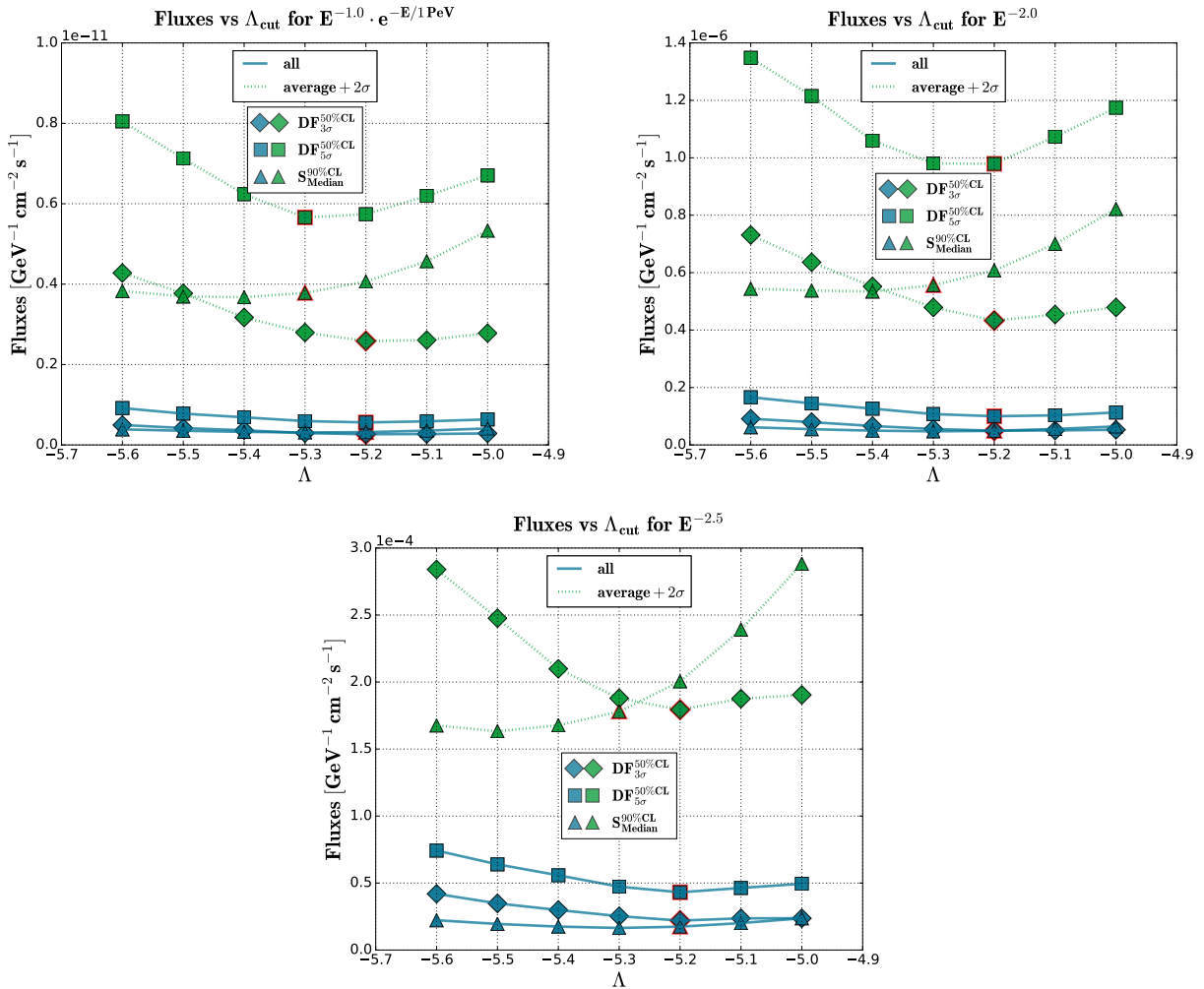


Figure 46: Fluxes vs  $\Lambda$  for Mrk 501. *Upper left panel:*  $E^{-1.0} \exp(-E/1 \text{PeV})$ . *Upper right panel:*  $E^{-2.0}$ . *Lower panel:*  $E^{-2.5}$ . Light red color represents the values with  $\Lambda$  that maximizes  $MDP^{3\sigma}/MDP^{5\sigma}$ .

As have been seen from the previous results based on the 17 months HAWC search [1], the usage of all available flares (long case) is preferable (see comparison plots in Fig. 46, 47 since it requires lower fluxes for discovery. The HAWC detector provides data for almost each day and longer periods have better acceptance, and such long duration flare timing information can significantly improve the efficiency of the search.

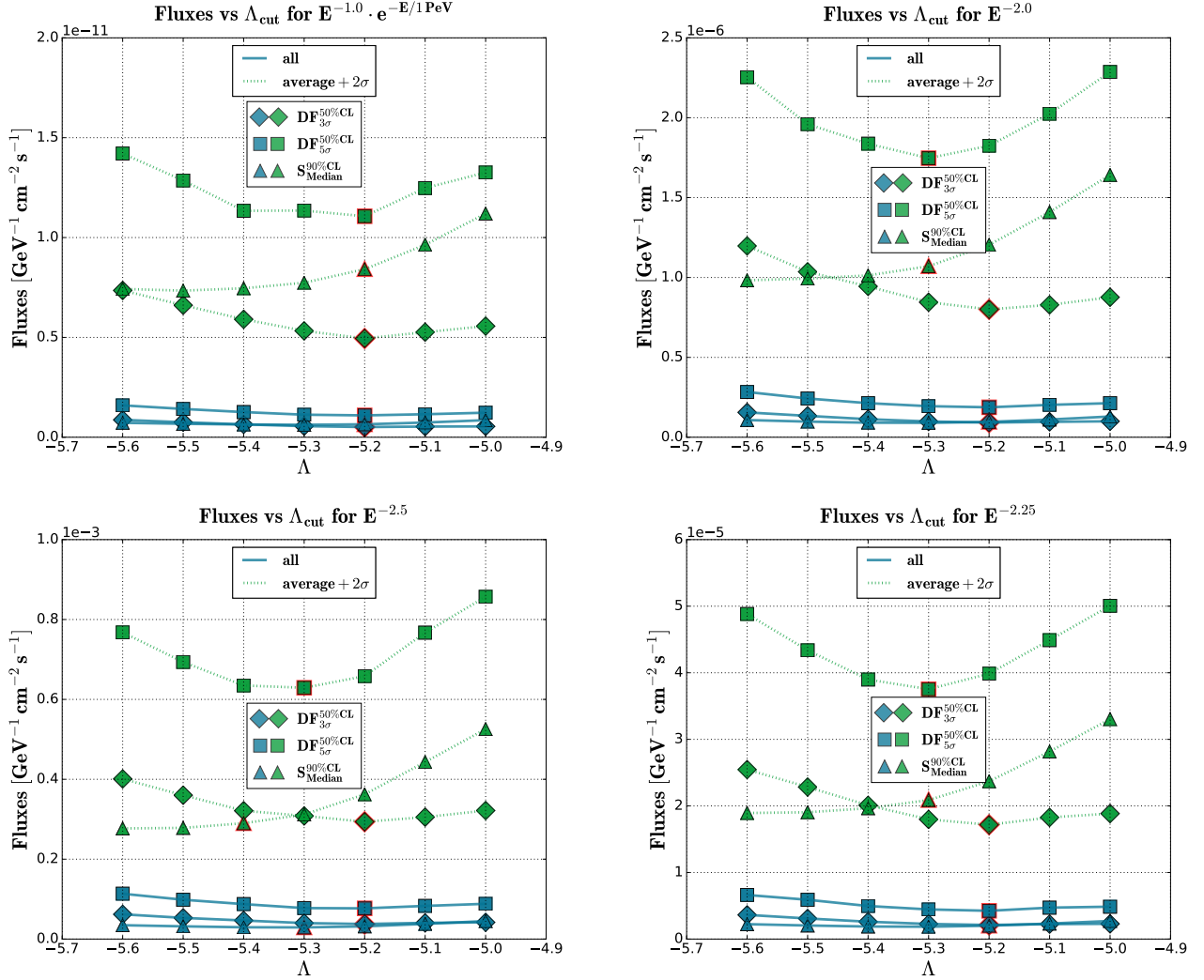


Figure 47: Fluxes vs  $\Lambda$  for Mrk 501. *Upper left panel:*  $E^{-1.0} \exp(-E/1\text{PeV})$ . *Upper right panel:*  $E^{-2.0}$ . *Lower left panel:*  $E^{-2.5}$ . *Lower right panel:*  $E^{-2.25}$ . Light red color represents the values with  $\Lambda$  that maximizes  $\text{MDP}^{5\sigma}$  (or  $\text{MDP}^{3\sigma}$ ).

Results on optimization for Mrk 421 and Mrk 501 are summarized in Table 8, 9.

Table 8: Results on optimization for Mrk 421

	T <sub>flare</sub>	LT	$\Lambda$	$N_S^{3\sigma}$	$\Lambda$	$N_S^{5\sigma}$	$DF_{3\sigma}^{50\%CL}$	$DF_{5\sigma}^{50\%CL}$
$E^{-1.0} \exp(-E/1\text{PeV})$								
L	1130	1099.93	-5.2	1.45	-5.2	3.05	0.27	0.56
S: av. + 2 $\sigma$	85	83.77	-5.2	1.05	-5.3	2.53	2.59	5.66
$\times 10^{-12} \cdot \text{GeV}^{-1} \text{cm}^{-2} \text{s}^{-1}$								
$E^{-2.0}$								
L	1130	1099.93	-5.2	1.81	-5.2	3.65	0.50	1.00
S: av. + 2 $\sigma$	85	83.77	-5.2	1.19	-5.3	3.05	4.33	9.80
$\times 10^{-7} \cdot \text{GeV}^{-1} \text{cm}^{-2} \text{s}^{-1}$								
$E^{-2.5}$								
L	1130	1099.93	-5.2	2.43	-5.2	4.77	0.22	0.43
S: av. + 2 $\sigma$	85	83.77	-5.3	1.89	-5.3	3.73	1.88	3.71
$\times 10^{-4} \cdot \text{GeV}^{-1} \text{cm}^{-2} \text{s}^{-1}$								

Table 9: Results on optimization for Mrk 501

	T <sub>flare</sub>	LT	$\Lambda$	$N_S^{3\sigma}$	$\Lambda$	$N_S^{5\sigma}$	$DF_{3\sigma}^{50\%CL}$	$DF_{5\sigma}^{50\%CL}$
$E^{-1.0} \exp(-E/1\text{PeV})$								
L	578	561.55	-5.2	1.35	-5.2	2.89	0.51	1.10
S: av. + 2 $\sigma$	35	34.6	-5.2	0.97	-5.2	2.17	4.95	11.1
$\times 10^{-12} \cdot \text{GeV}^{-1} \text{cm}^{-2} \text{s}^{-1}$								
$E^{-2.0}$								
L	578	561.55	-5.2	1.67	-5.2	3.41	0.92	1.88
S: av. + 2 $\sigma$	35	34.6	-5.2	1.11	-5.3	2.79	8.01	17.5
$\times 10^{-7} \cdot \text{GeV}^{-1} \text{cm}^{-2} \text{s}^{-1}$								
$E^{-2.25}$								
L	578	561.55	-5.2	1.91	-5.2	3.83	0.21	0.42
S: av. + 2 $\sigma$	35	34.6	-5.3	1.49	-5.3	3.11	1.80	3.75
$\times 10^{-5} \cdot \text{GeV}^{-1} \text{cm}^{-2} \text{s}^{-1}$								
$E^{-2.5}$								
L	578	561.55	-5.2	2.19	-5.3	5.45	3.77	7.76
S: av. + 2 $\sigma$	35	34.6	-5.3	1.73	-5.4	4.05	3.08	6.35
$\times 10^{-5} \cdot \text{GeV}^{-1} \text{cm}^{-2} \text{s}^{-1}$								

#### 10.4.4 MDP

The value of the cut on  $\Lambda$  is optimized for each source on the basis of maximizing the MDP for the  $3\sigma$  or  $5\sigma$  significance levels for each spectrum. MDP sets best limits in case of the no-discovery. Fig. 48, 49 represent the MDP values versus  $\Lambda$  at  $3\sigma/5\sigma$  level for the Mrk 421 and Mrk 501.

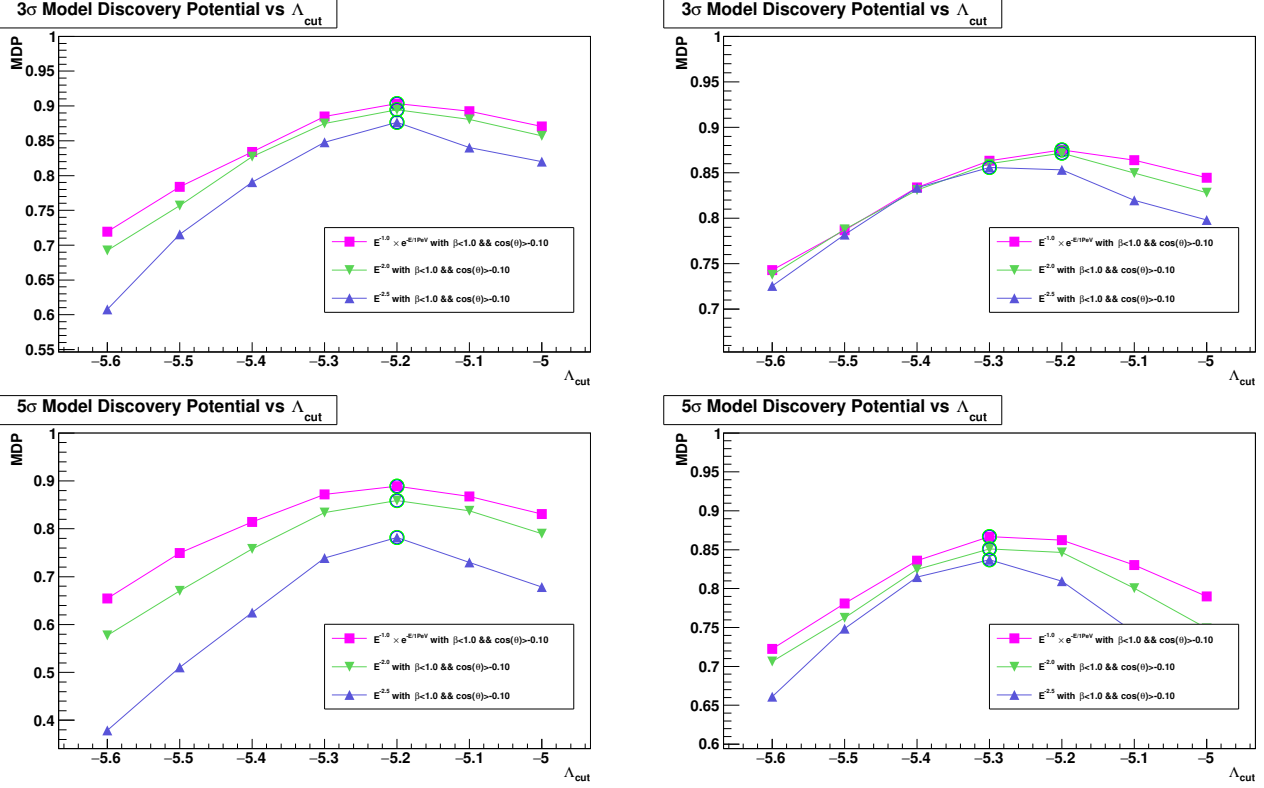


Figure 48: MDP for Mrk 421. *Upper panel* for  $3\sigma$  discovery. *Lower panel* for  $5\sigma$  discovery. *Left panel*: all flares. *Right panel*: flares with average flux +  $2\sigma$  threshold. Light green color circles represent the maximum MDP values.

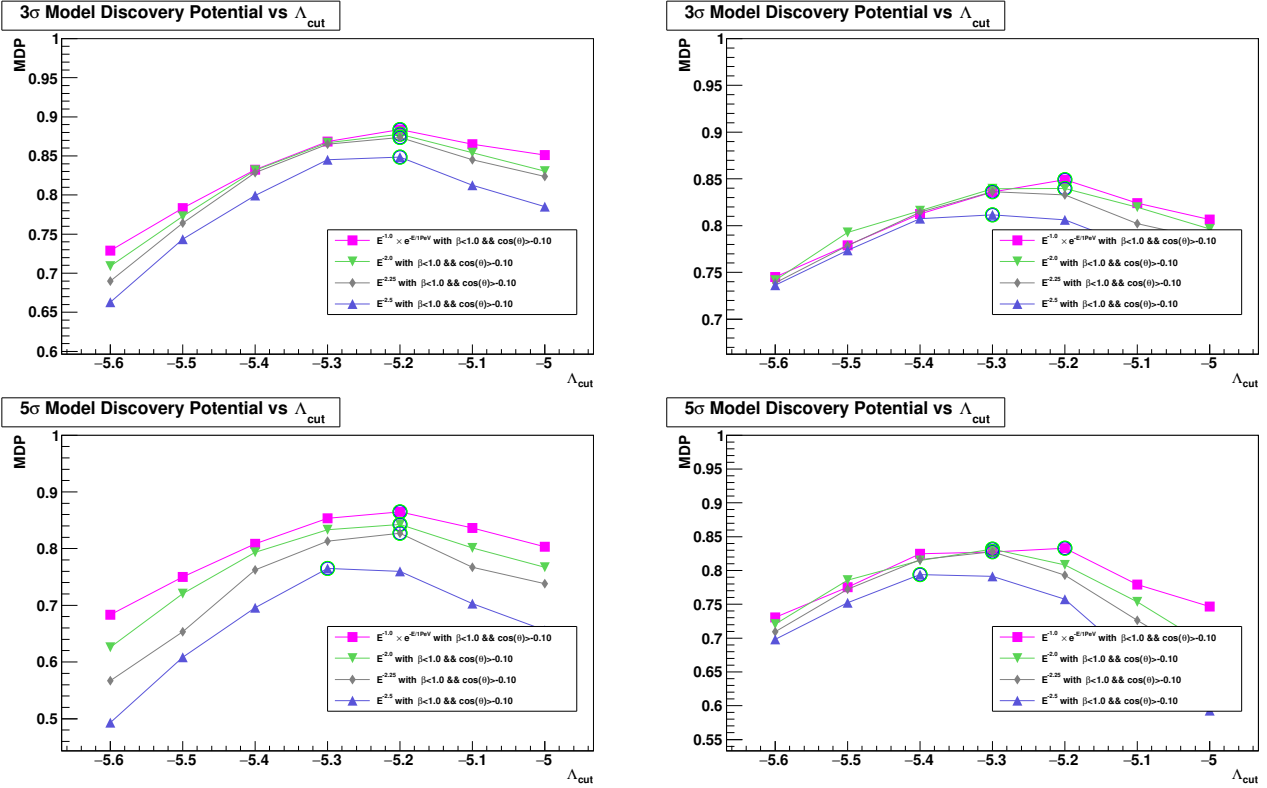


Figure 49: MDP for Mrk 501. *Upper panel* for  $3\sigma$  discovery. *Lower panel* for  $5\sigma$  discovery. *Left panel*: all flares. *Right panel*: flares with *average flux +  $2\sigma$*  threshold. Light green color circles represent the maximum MDP values.

### 10.4.5 Sensitivities

If no discovery is made, the upper limits will be calculated according to the classical (frequentist) approach [16]. The Neyman [16] 90% C.L. upper limits on the fluence, which is the energy per unit area [ $\text{GeV cm}^{-2}$ ], are calculated as follows:

$$\mathcal{F}^{90\%CL} = \int F dt = F \Delta T = \Delta T \cdot \Phi_0^{90\%CL} \int_{E_{min}}^{E_{max}} E S(E) dE \quad (15)$$

Here:

- $\Delta T$  is the livetime of the search [s];
- $\Phi_0^{90\%CL} = DF^{90\%CL}$  is the upper limit on the neutrino flux normalization [ $\text{GeV}^{-1} \text{cm}^{-2} \text{s}^{-1}$ ];
- $S(E)$  is the dimensionless neutrino spectra  $(\frac{E}{\text{GeV}})^{-\gamma}$ , and  $dN/dE = \Phi_0 \cdot S(E)$ ;
- $E_{min}$  and  $E_{max}$  are 5% and 95% energy limits respectively, defined to contain 90% of the spectrum emission. This is the energy range at which ANTARES is sensible for each spectrum  $S(E)$  and source, and computed from the MC neutrino simulation used to calculate the PSF. The MC neutrino simulation extends up to  $10^8$  GeV.

The sensitivities at 90% C.L. on neutrino fluxes and fluences for each source and spectrum for corresponding limits are listed in Table 10. The Fig. 50, 52 summarize the sensitivities on the neutrino fluxes and fluences. The spectral energy distribution (SED) of Mrk 421 obtained during multifrequency campaign between 2009 January 19 to 2009 June 1 [18] and the neutrino energy flux obtained from this analysis are shown on Fig. 51. Additionally, Fig. 54 show the comparison plots of the sensitivities on the neutrino fluxes obtained in HAWC 2014-2016 and HAWC 2014-2017 analyses.

Table 10: Sensitivities at 90% C.L.

	$S(E)$	T <sub>flare</sub>	LT	$\Lambda$	$E_{min}$	$E_{max}$	$\Phi_0^{90\%CL}$	$\mathcal{F}^{90\%CL}$
Mrk 421	$E^{-1.0} \cdot e^{-E/1\text{PeV}}$			-5.2	4.824	6.400	3.177 <sup>*1</sup>	25.8
	$E^{-2.0}$	1130	1099.93	-5.2	4.032	7.040	4.902 <sup>*2</sup>	32.2
	$E^{-2.5}$			-5.2	3.152	5.968	1.744 <sup>*3</sup>	84.7
Mrk 501	$E^{-1.0} \cdot e^{-E/1\text{PeV}}$			-5.2	4.832	6.392	6.484 <sup>*1</sup>	26.7
	$E^{-2.0}$	578	561.551	-5.2	4.000	7.048	9.624 <sup>*2</sup>	32.8
	$E^{-2.25}$			-5.2	3.616	6.480	0.200 <sup>*3</sup>	39.2
	$E^{-2.5}$			-5.3	3.104	5.912	2.917 <sup>*3</sup>	76.6
							$\cdot \text{GeV}^{-1} \text{cm}^{-2} \text{s}^{-1}$	$\cdot \text{GeV cm}^{-2}$

Note:  $E_{min}$  and  $E_{max}$  in log.

<sup>\*1</sup>  $\times 10^{-13}$

<sup>\*2</sup>  $\times 10^{-8}$

<sup>\*3</sup>  $\times 10^{-5}$

[LT] = [T<sub>flare</sub>] = days.

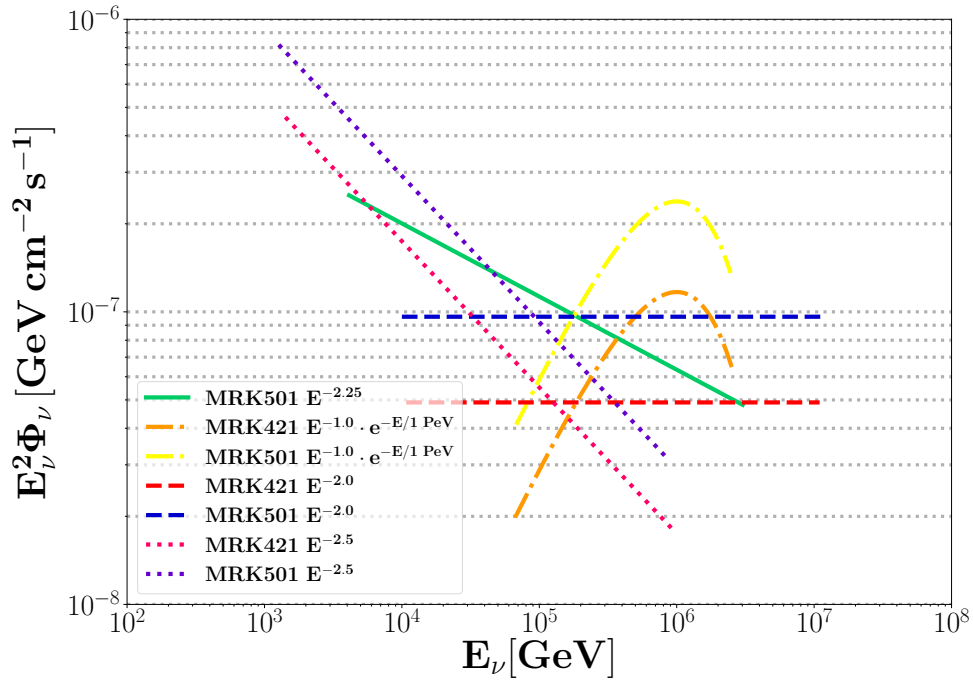


Figure 50: Neutrino energy flux sensitivities at 90% C.L. obtained in the analysis with  $E^{-1.0} \exp(-E/1 \text{ PeV})$ ,  $E^{-2.0}$ ,  $E^{-2.5}$ ,  $E^{-2.25}$  (this for Mrk 501 only) neutrino energy spectra. Obtained for the long case with sensitivity fluxes for optimum  $\Lambda$  values for each spectrum.

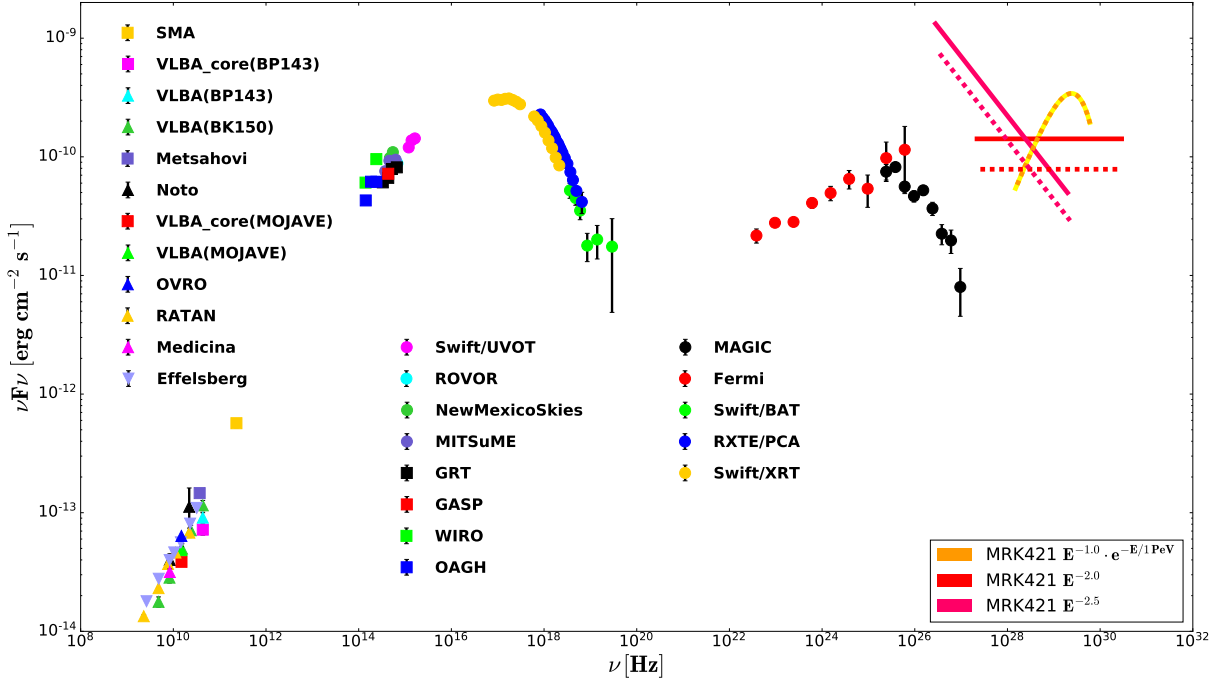


Figure 51: SED of Mrk 421 and the neutrino energy flux sensitivities at 90% C.L. obtained in the analysis. Adapted from [18].

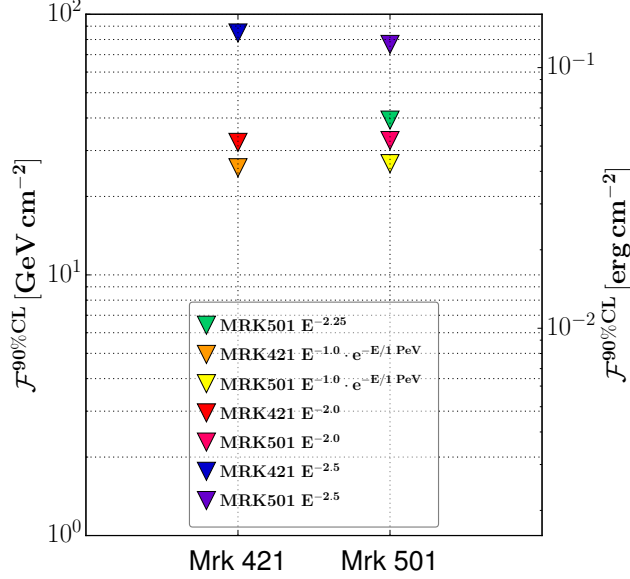


Figure 52: Neutrino fluence sensitivities at 90% C.L. obtained in the analysis with  $E^{-1.0} \exp(-E/1 \text{PeV})$ ,  $E^{-2.0}$ ,  $E^{-2.5}$ ,  $E^{-2.25}$  (this for Mrk 501 only) neutrino energy spectra. Obtained for long case with sensitivity fluxes for optimum  $\Lambda$  values for each spectrum.

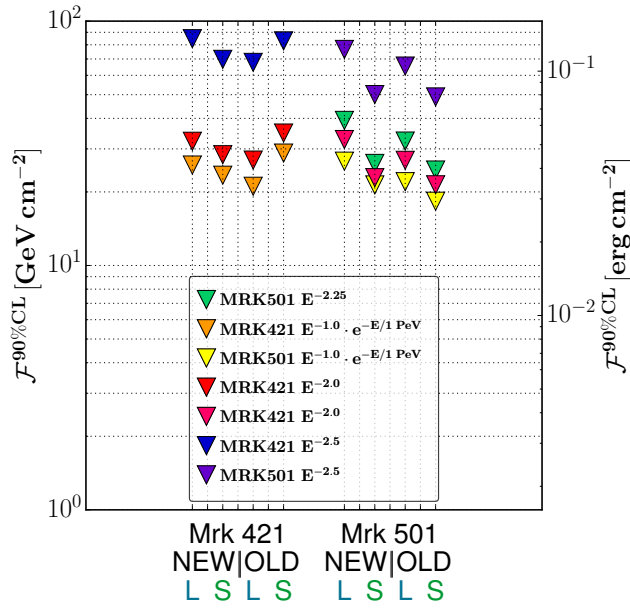


Figure 53: Comparison plots for neutrino fluence sensitivities at 90% C.L. obtained in the analysis with  $E^{-1.0} \exp(-E/1 \text{PeV})$ ,  $E^{-2.0}$ ,  $E^{-2.5}$ ,  $E^{-2.25}$  (this for Mrk 501 only) neutrino energy spectra. Obtained for long case with sensitivity fluxes for optimum  $\Lambda$  values for each spectrum. The HAWC 2014-2017 and HAWC 2014-2016 analyses are denoted by "new" and "old" respectively. "L" (green) and "S" (blue) denote the long case (all flares are selected) and short case (flares with *average flux + 2 $\sigma$*  threshold are selected) respectively.

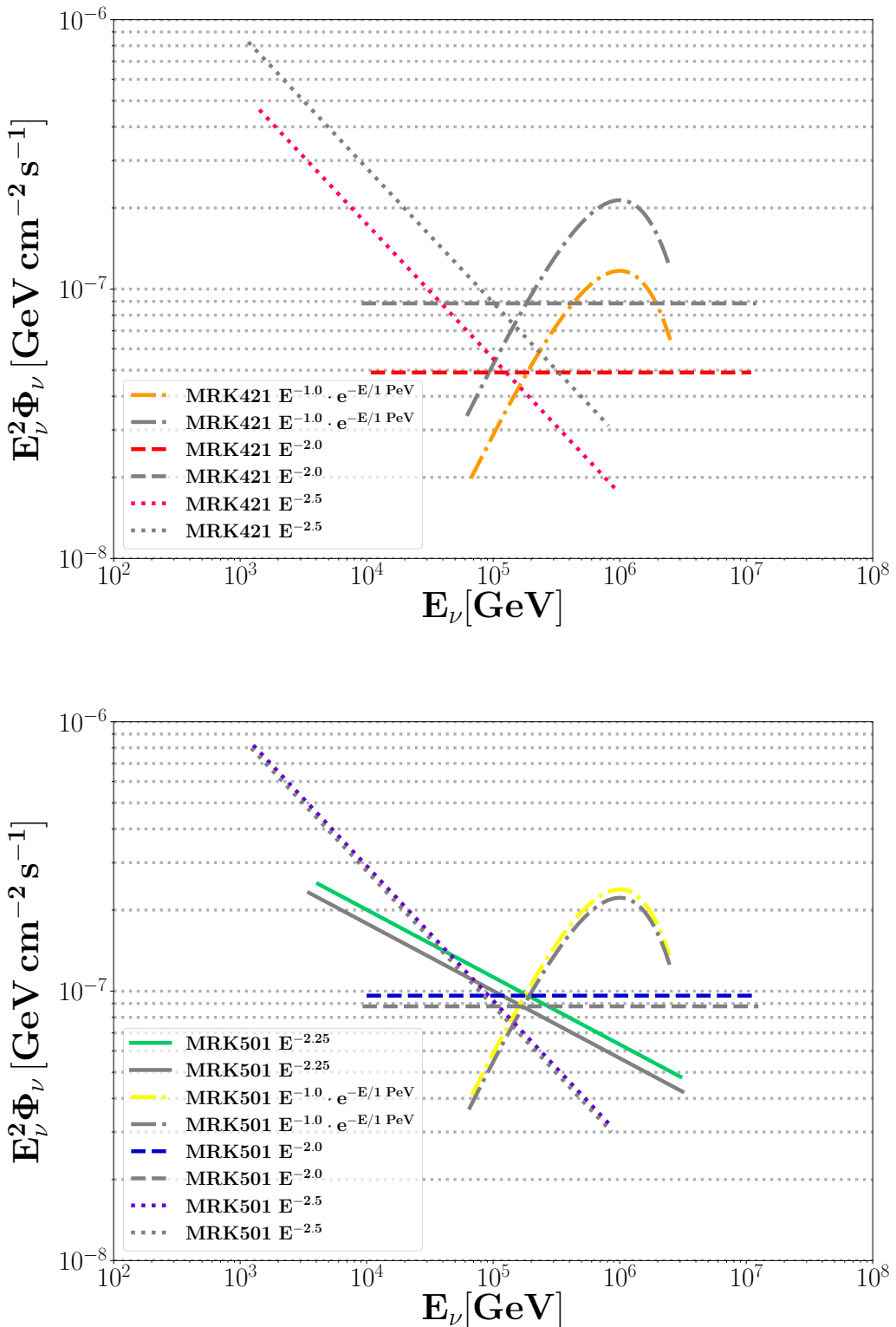


Figure 54: Comparison plots for neutrino energy flux sensitivities at 90% C.L. for Mrk 421 (*Upper panel*) and Mrk 501 (*Lower panel*) obtained for long case. Grey color and colored curves represent HAWC 2014-2016 and HAWC 2014-2017 periods.

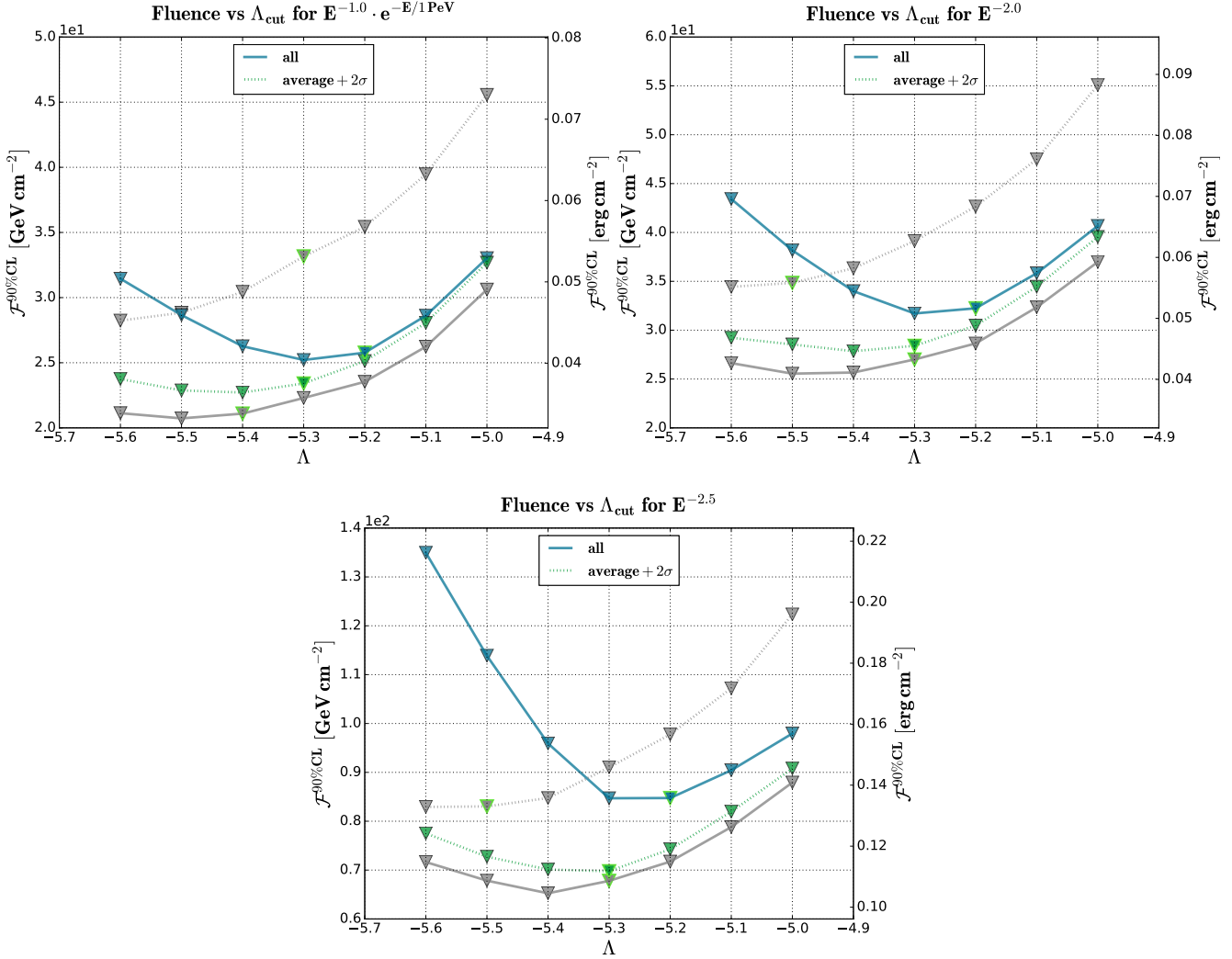


Figure 55: Comparison plots for neutrino fluence sensitivities at 90% C.L. vs  $\Lambda$  for Mrk 421 for different peak selection thresholds. *Upper left panel:*  $E^{-1.0} \exp(-E/1\text{PeV})$ . *Upper right panel:*  $E^{-2.0}$ . *Lower panel:*  $E^{-2.5}$ . Grey color and colored curves represent HAWC 2014-2016 and HAWC 2014-2017 periods respectively. Light green color circles represent the sensitivities derived with  $DF^{90\%CL}$  of optimum  $\Lambda$  values.

The HAWC 2014-2016 and HAWC 2014-2017 comparison plots for fluence 90% C.L. sensitivities vs  $\Lambda$  for long case and short case with *average flux* +  $2\sigma$  are gathered in Fig. 55, 56. The HAWC 2014-2016 and HAWC 2014-2017 comparison plots for fluence 90% C.L. sensitivities obtained for long and short cases for optimum  $\Lambda$  values are shown in Fit. 53. The fluence in the short case is more preferable since as in the last analysis, it getting lower with respect to increase of the threshold (except for the last analysis with Mrk 421). This is contrary to that we previously obtained for discovery fluxes. As a result, the better sensitivities on the neutrino fluxes can be obtained with the long case, but the better sensitivities on the neutrino fluences can be obtained with the short case (if the HAWC 2014-2017 period is considered), especially with the *average flux* +  $2\sigma$  threshold applied as a peak selection criteria. The idea is to use the long case to obtain best sensitivities on the fluxes, but in contrary to use the short case (with the *average flux* +  $2\sigma$  threshold) to obtain best sensitivities on the fluences, because in this case it places a better sensitivity.

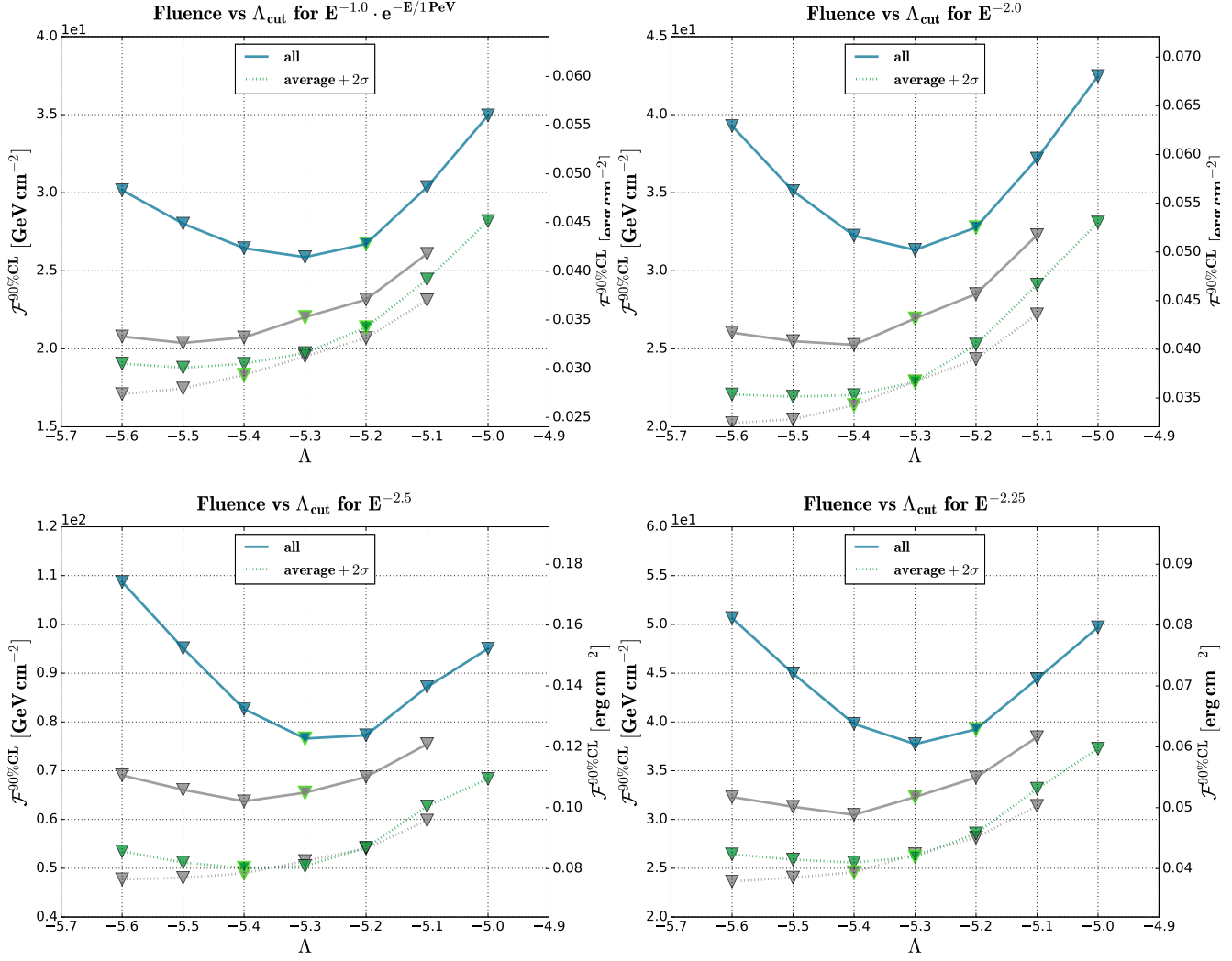


Figure 56: Comparison plots for neutrino fluence sensitivities at 90% C.L. vs  $\Lambda$  for Mrk 501 for different peak selection thresholds. *Upper left panel:*  $E^{-1.0} \exp(-E/1\text{PeV})$ . *Upper right panel:*  $E^{-2.0}$ . *Lower left panel:*  $E^{-2.5}$ . *Lower right panel:*  $E^{-2.25}$ . Grey color and colored curves represent HAWC 2014-2016 and HAWC 2014-2017 periods respectively. Light green color circles represent the sensitivities derived with  $\mathcal{F}^{90\%CL}$  of optimum  $\Lambda$  values.

# Conclusion Final

- Neutrino energy flux sensitivities:
  - For Mrk 421 is getting better by factor  $\sim 1.8$  w.r.t. last analysis  
     $\hookrightarrow$  we used  $\sim 100\%$  longer LC data for the current analysis.
  - For Mrk 501 is getting worse by factor  $\sim 1.1$  w.r.t. last analysis  
     $\hookrightarrow$  we used  $\sim 20\%$  longer LC data for the current analysis.

Many things play a role here like  $\Lambda$  cuts which is selected as optimum (see WiKi). Might be also the Bayesian Blocks not significantly but can affect on it (see WiKi): the shape of blocks are almost identical but not completely if, for example, Bayesian Blocks are made for an identical period of current and last analysis like using first  $\sim 500$  days of data.;

- Neutrino fluence sensitivities:
  - For Mrk 421:
    - \* for long case is getting worse w.r.t. last analysis;
    - \* for short case is getting better w.r.t. last analysis.
  - For Mrk 501:
    - \* for long case is getting worse w.r.t. last analysis;
    - \* for short case is getting worse w.r.t. last analysis.

# Appendix

## A HAWC 2014-2016

### A.1 OFF days

Table 11: List of OFF days

57095	57122	57132	57219	57244	57254	57264	57358	57368	57378
57113	57123	57133	57235	57245	57255	57302	57359	57369	57379
57114	57124	57134	57236	57246	57256	57304	57360	57370	57380
57115	57125	57135	57237	57247	57257	57310	57361	57371	57381
57116	57126	57136	57238	57248	57258	57312	57362	57372	57382
57117	57127	57137	57239	57249	57259	57313	57363	57373	57383
57118	57128	57138	57240	57250	57260	57314	57364	57374	57384
57119	57129	57139	57241	57251	57261	57321	57365	57375	57385
57120	57130	57140	57242	57252	57262	57324	57366	57376	57386
57121	57131	57141	57243	57253	57263	57357	57367	57377	57387

Number of days off: 100.

Total ANTARES OFF period belongs to 2015 (57023-57387) year only.

## A.2 Figures for 3 sigma

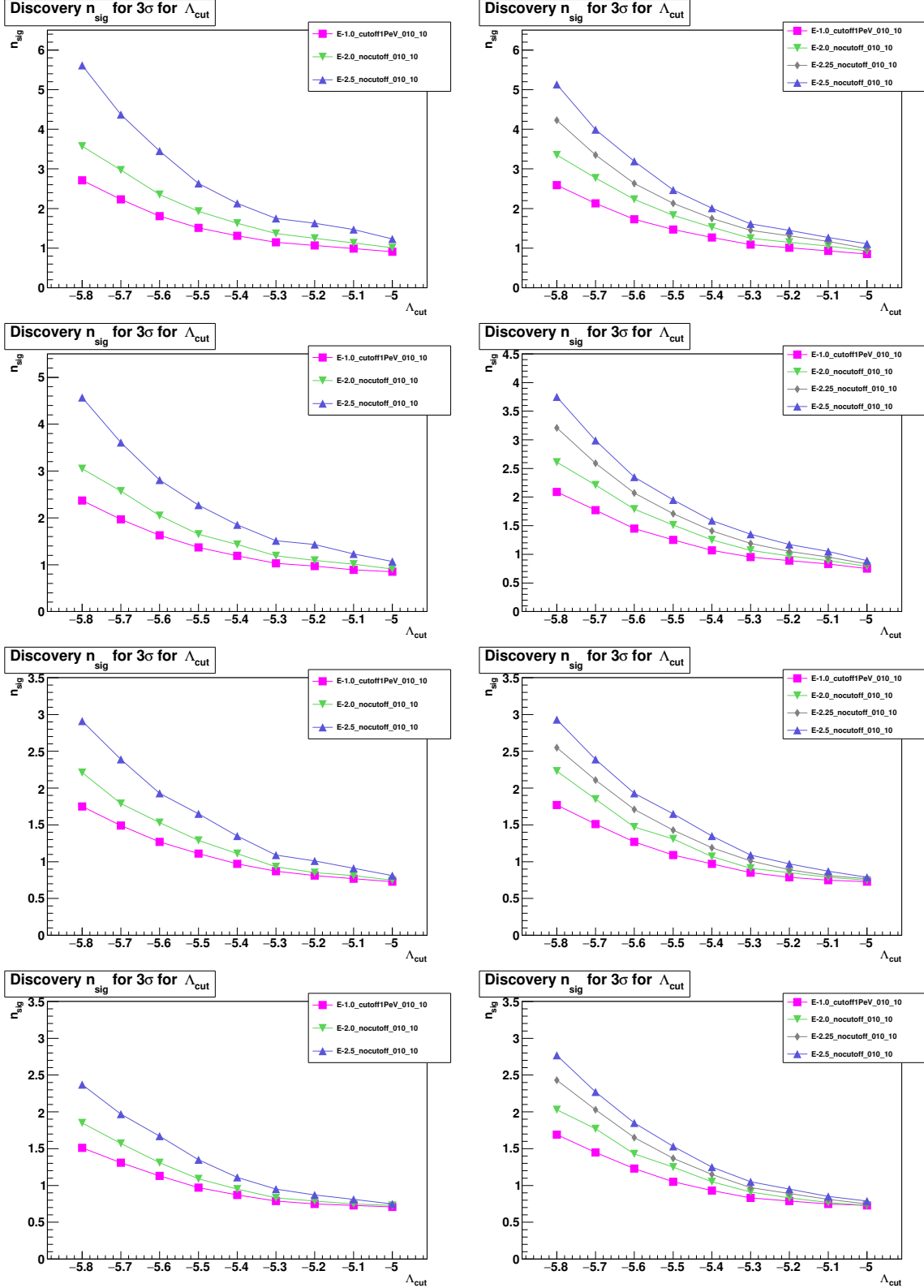


Figure 57: Discovery power at  $3\sigma$  level. *Left panel:* Mrk 421 *Right panel:* Mrk 501. From upper to bottom: all flares, short flares with *average flux*, *average flux + 1 $\sigma$* , *average flux + 2 $\sigma$*  thresholds.

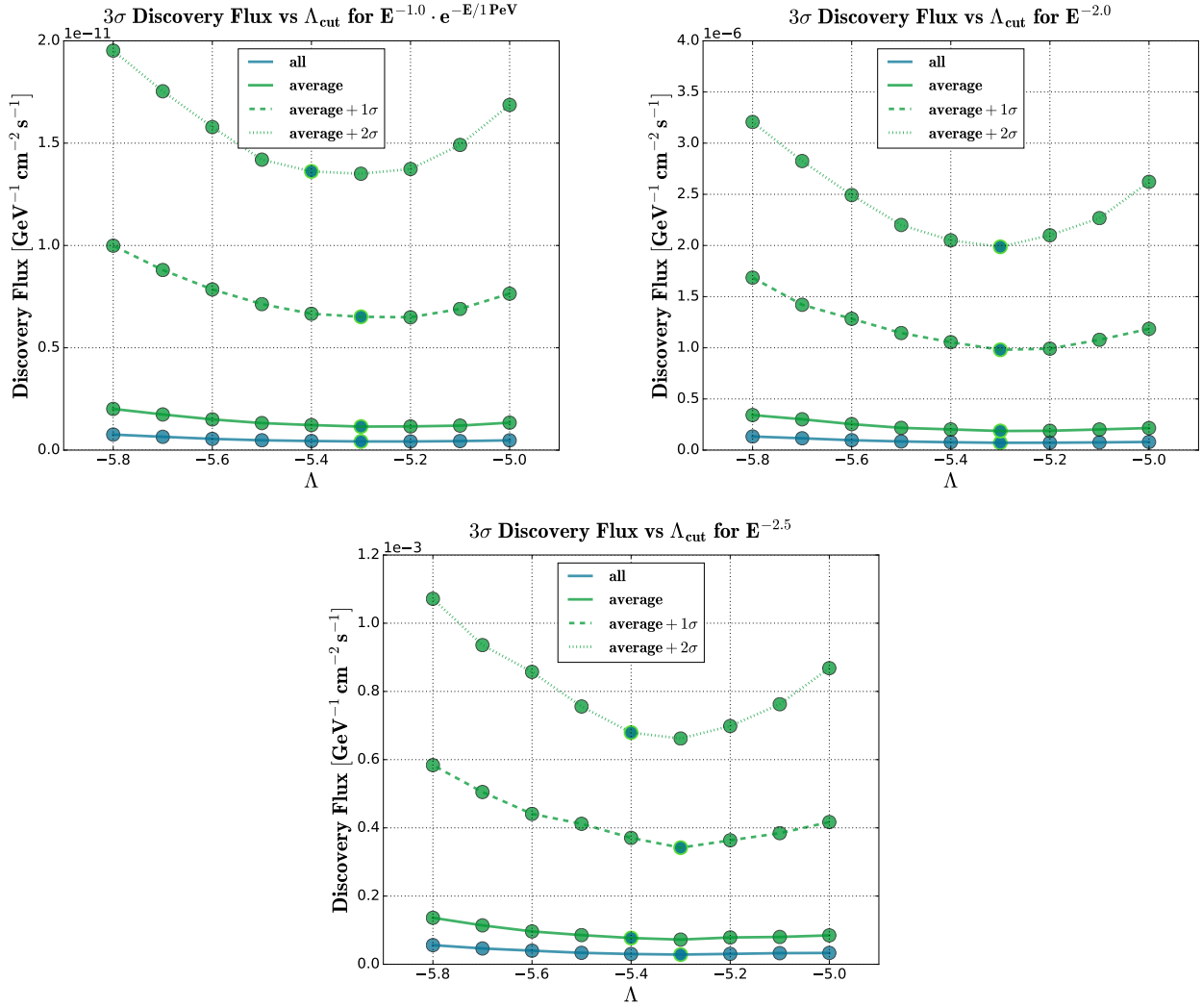


Figure 58: Discovery fluxes comparison at  $3\sigma$  level for Mrk 421 for several thresholds. *Upper left panel:*  $E^{-1.0} \exp(-E/1\text{PeV})$ . *Upper right panel:*  $E^{-2.0}$ . *Lower panel:*  $E^{-2.5}$ . Light green color circles represent the values with  $\Lambda$  that maximizes  $\text{MDP}^{3\sigma}$ .

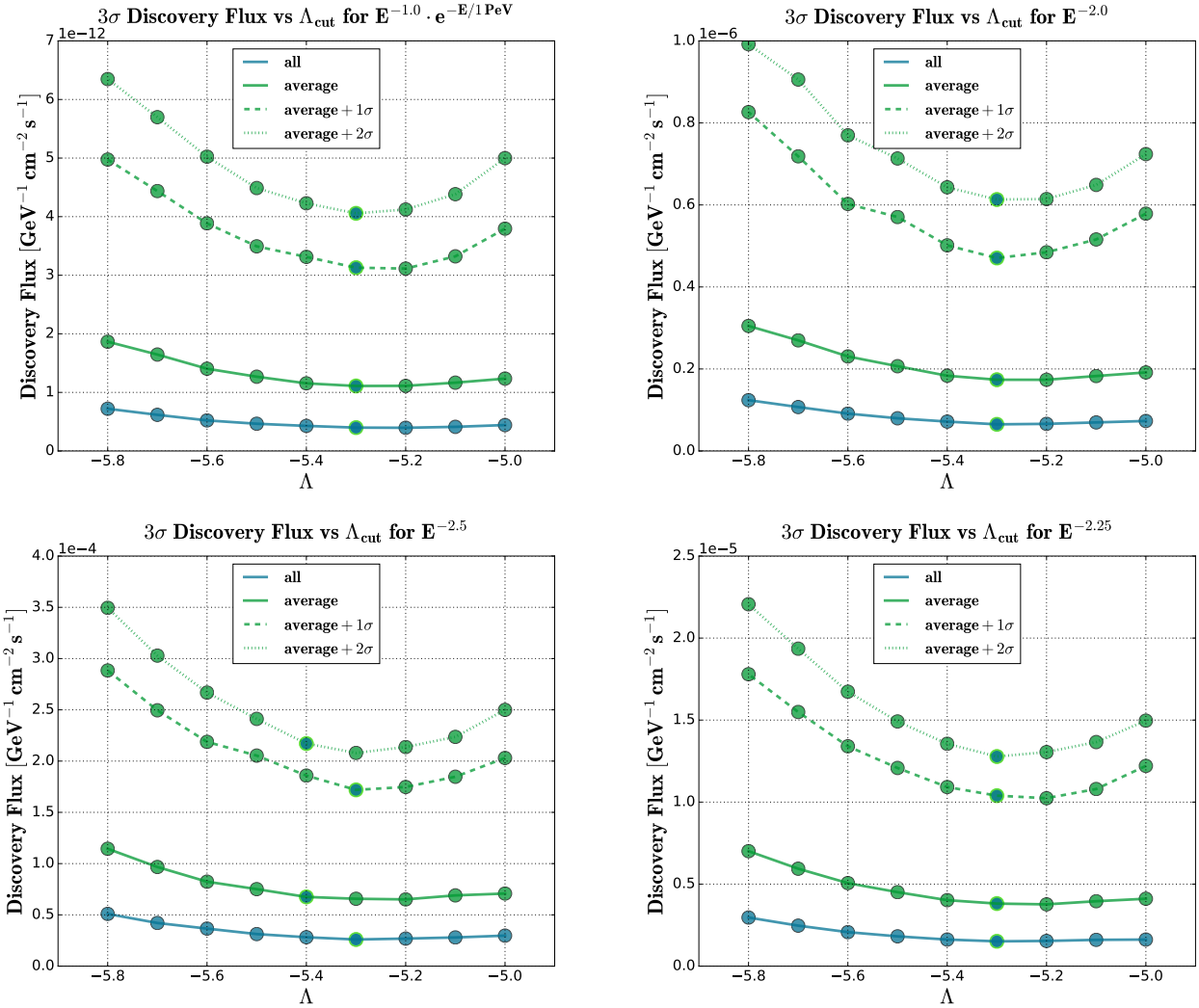


Figure 59: Discovery fluxes comparison at  $3\sigma$  level for Mrk 501 for several thresholds. *Upper left panel:*  $E^{-1.0} \exp(-E/1\text{PeV})$ . *Upper right panel:*  $E^{-2.0}$ . *Lower left panel:*  $E^{-2.5}$ . *Lower right panel:*  $E^{-2.25}$ . Light green color circles represent the values with  $\Lambda$  that maximizes  $\text{MDP}^{3\sigma}$ .

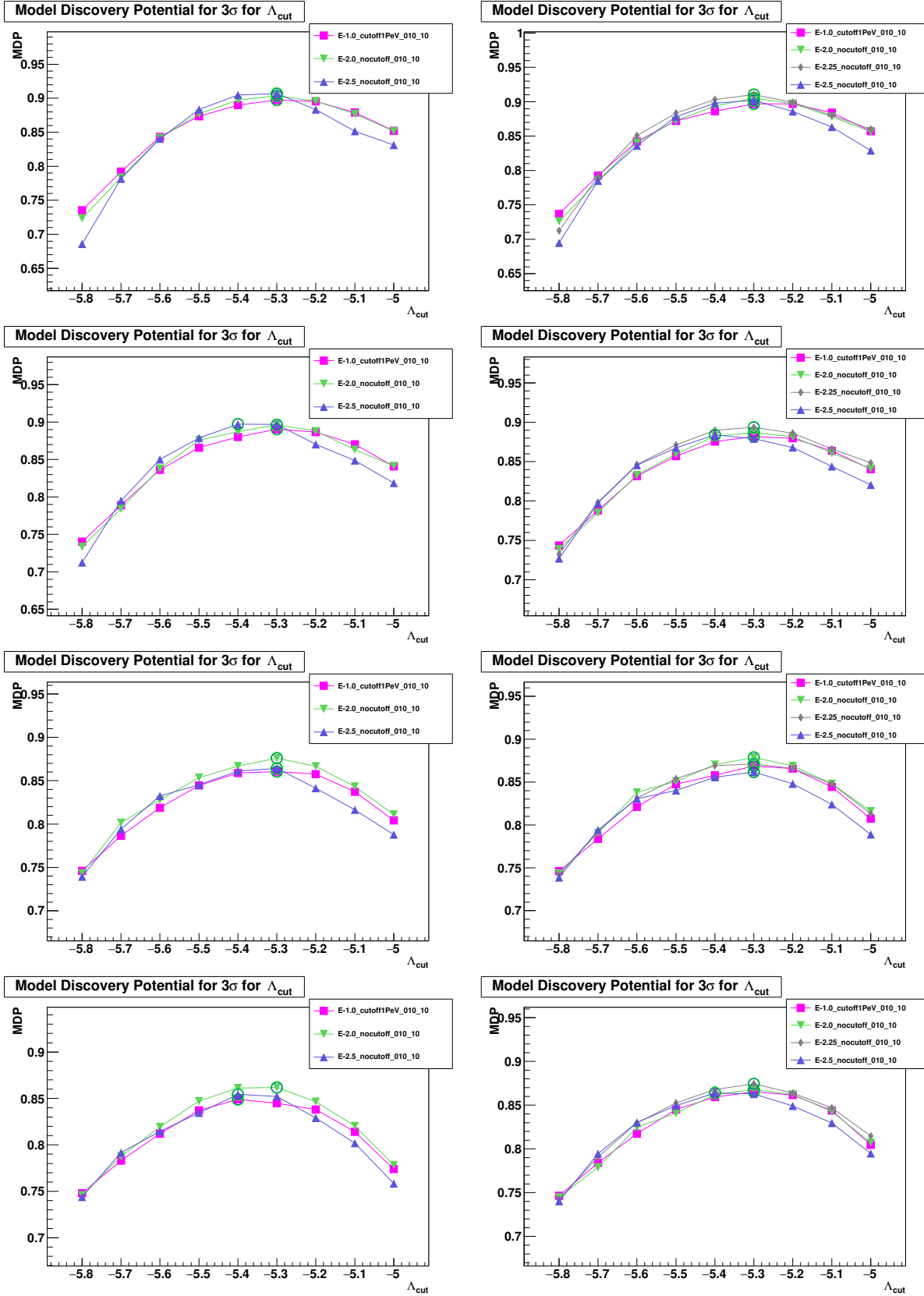


Figure 60: MDP for  $3\sigma$  evidence. *Left panel:* Mrk 421 *Right panel:* Mrk 501. From upper to bottom: all flares, short flares with *average flux*, *average flux + 1 $\sigma$* , *average flux + 2 $\sigma$*  thresholds.. Light green color circles represent the maximum MDP values.

## B HAWC 2014-2017

### B.1 Skymap plots with selected events

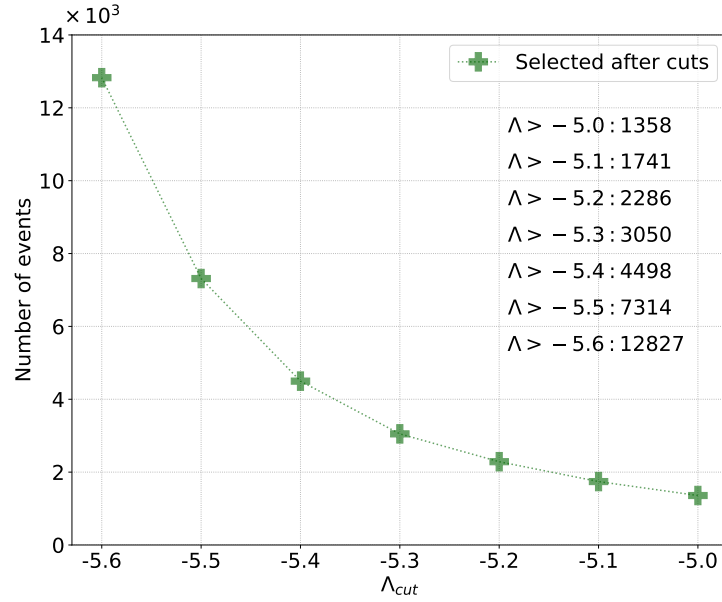


Figure 61: The track-like events passing the selection cuts.

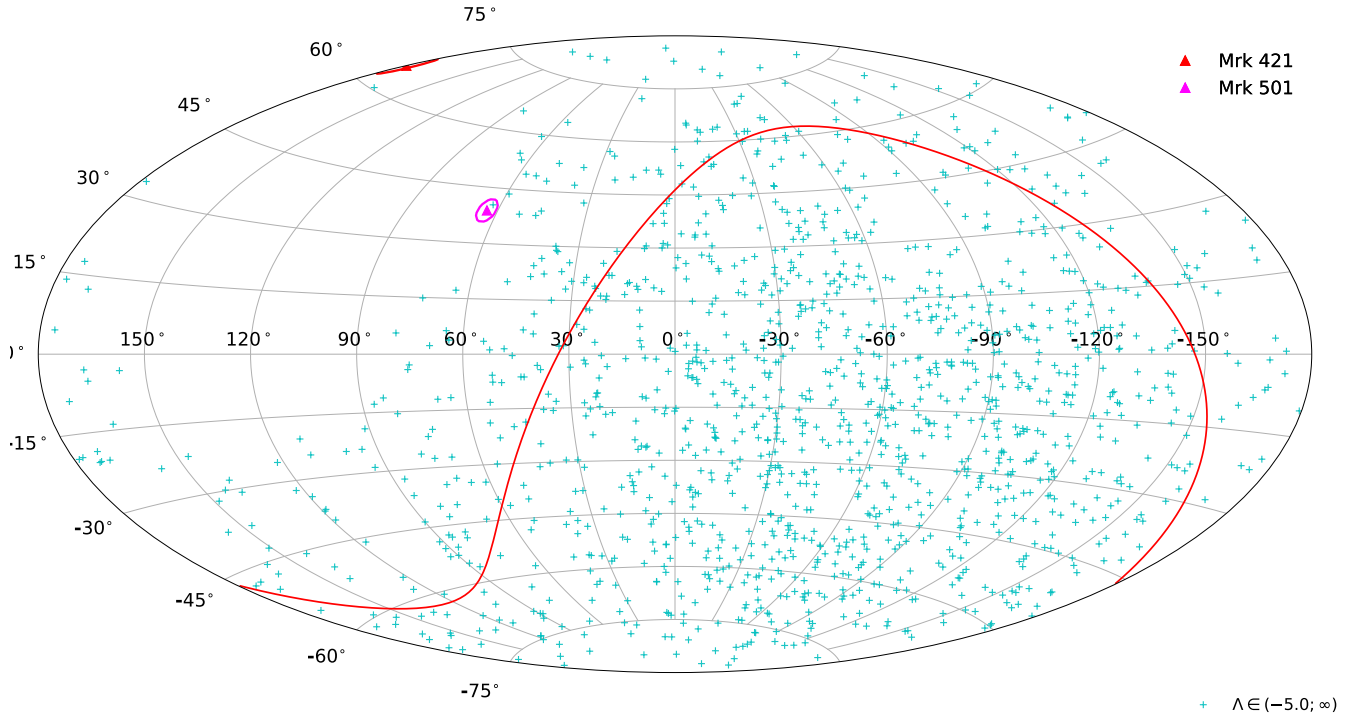


Figure 62: Sky map of the track-like events passing the selection cuts (total 1358 events selected with  $\Lambda > -5.0$ ). In galactic coordinates using Aitoff projection. The red solid curve denotes the equatorial plane. The red circles denote the 3 degree radius region around the sources.

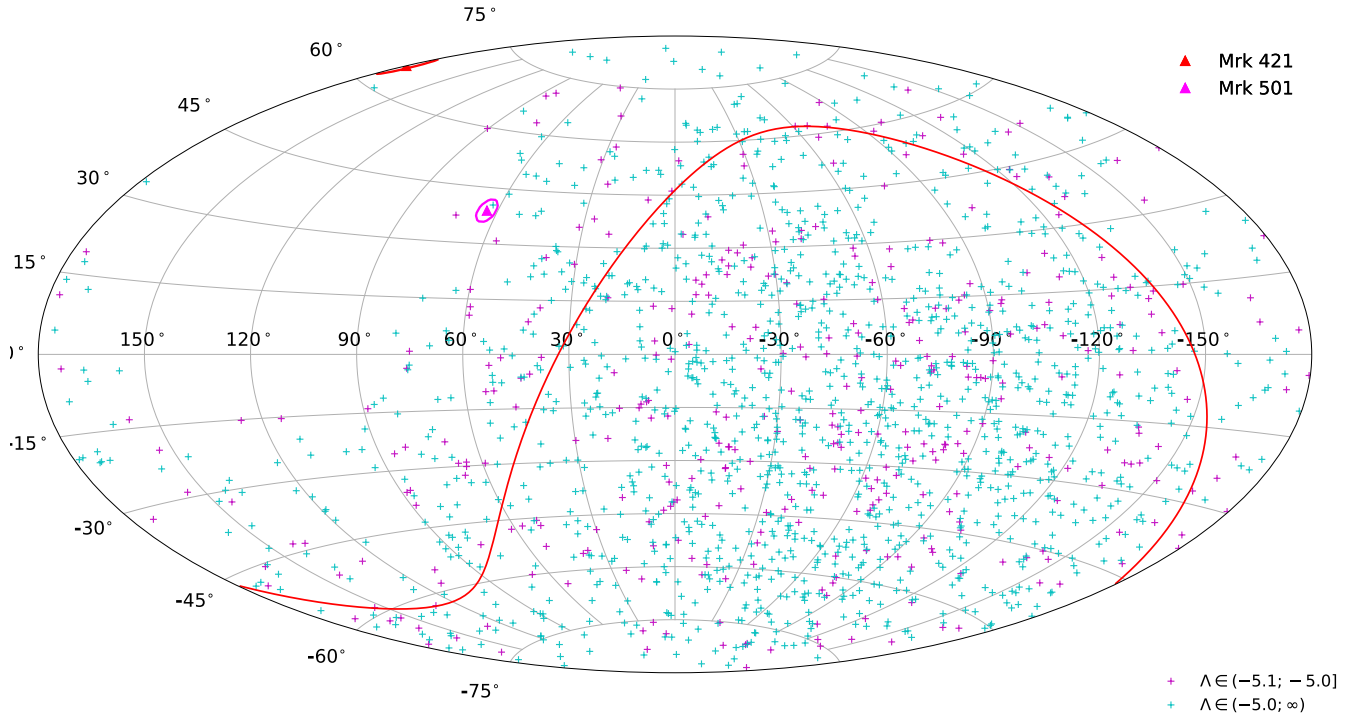


Figure 63: Sky map of the track-like events passing the selection cuts (total 1741 events selected with  $\Lambda > -5.1$ ). In galactic coordinates using Aitoff projection. The red solid curve denotes the equatorial plane. The red circles denote the 3 degree radius region around the sources.

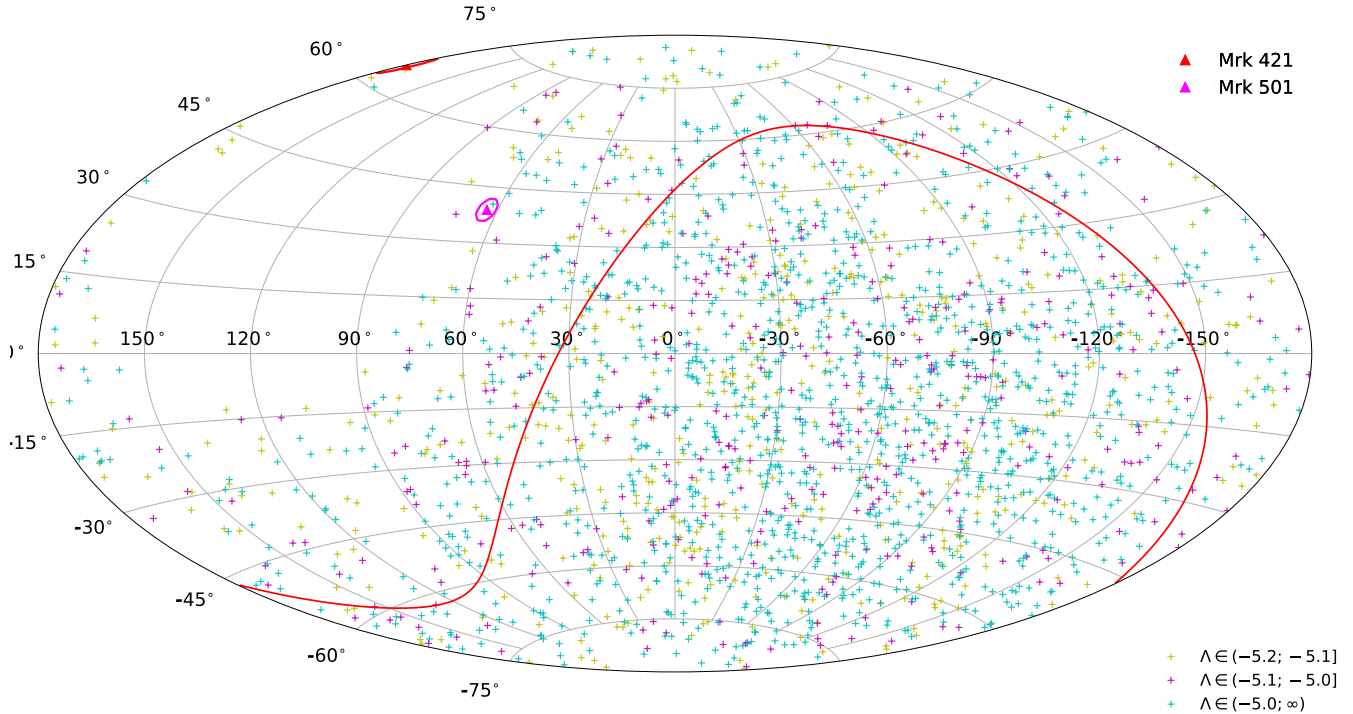


Figure 64: Sky map of the track-like events passing the selection cuts (total 2286 events selected with  $\Lambda > -5.2$ ). In galactic coordinates using Aitoff projection. The red solid curve denotes the equatorial plane. The red circles denote the 3 degree radius region around the sources.

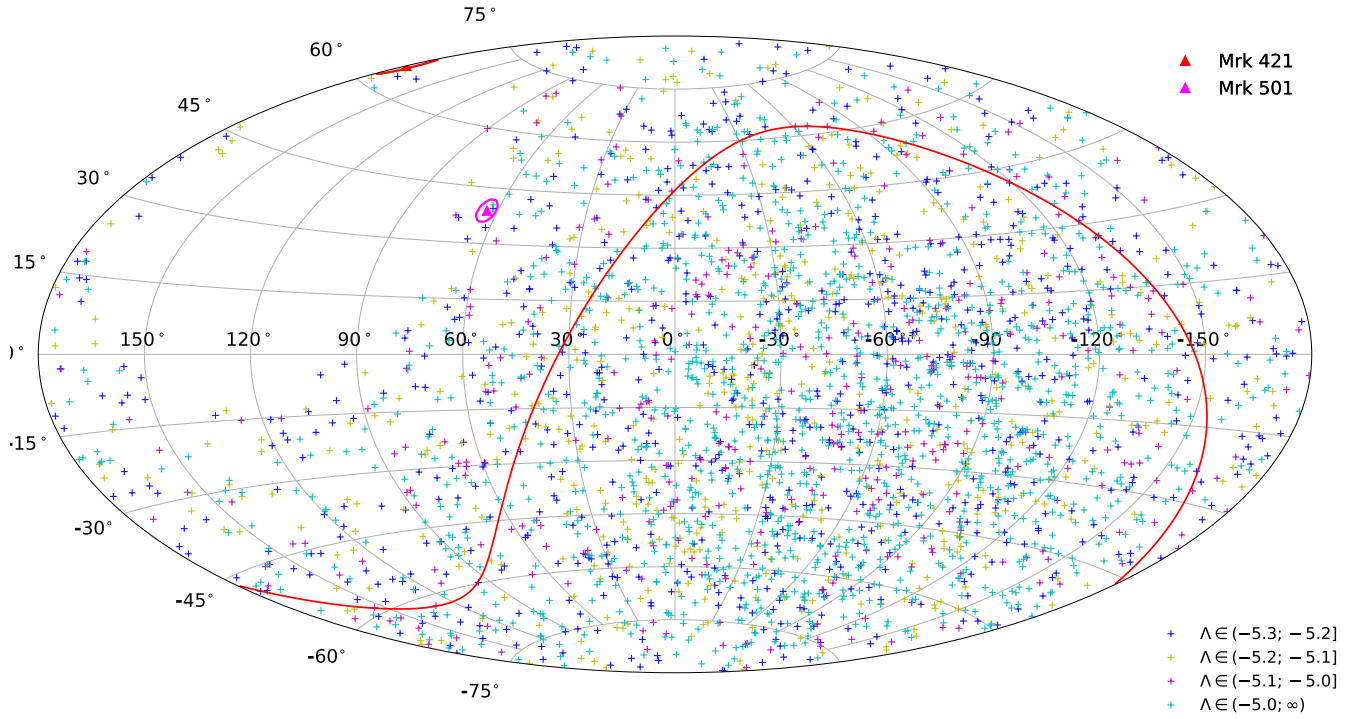


Figure 65: Sky map of the track-like events passing the selection cuts (total 3050 events selected with  $\Lambda > -5.3$ ). In galactic coordinates using Aitoff projection. The red solid curve denotes the equatorial plane. The red circles denote the 3 degree radius region around the sources.

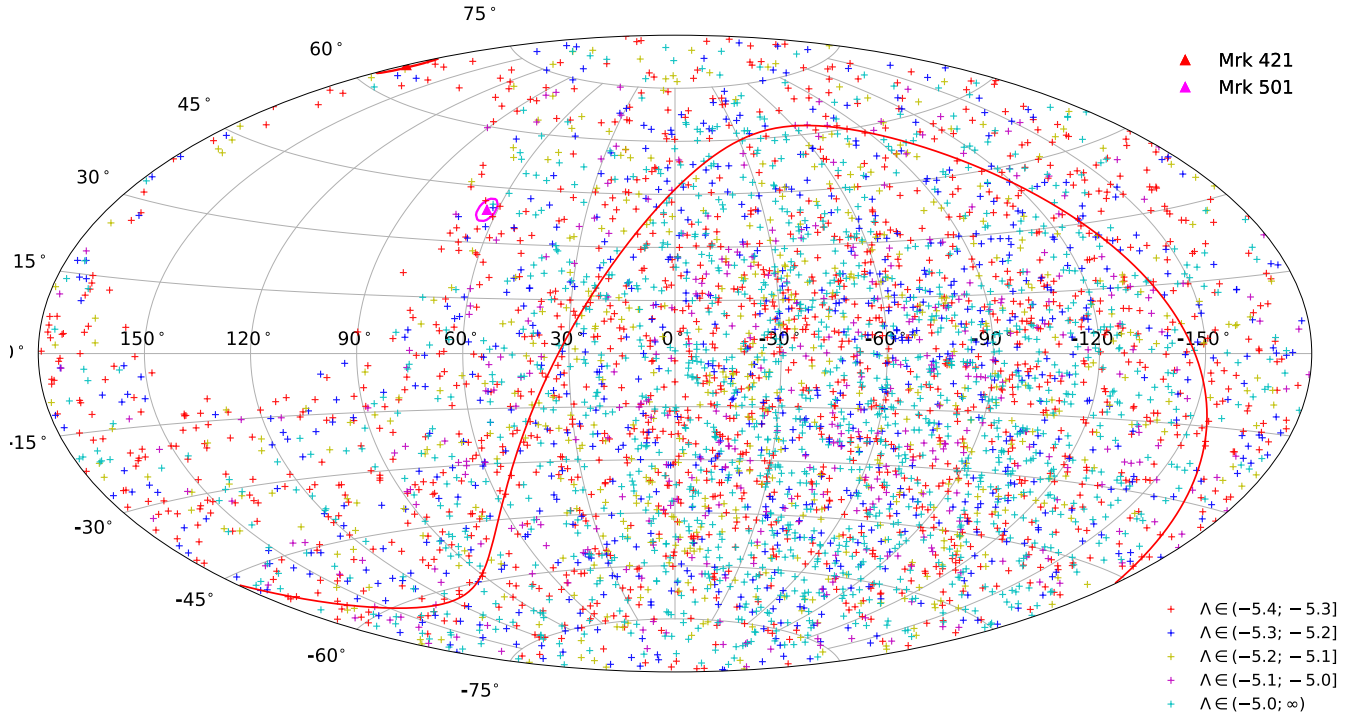


Figure 66: Sky map of the track-like events passing the selection cuts (total 4498 events selected with  $\Lambda > -5.4$ ). In galactic coordinates using Aitoff projection. The red solid curve denotes the equatorial plane. The red circles denote the 3 degree radius region around the sources.

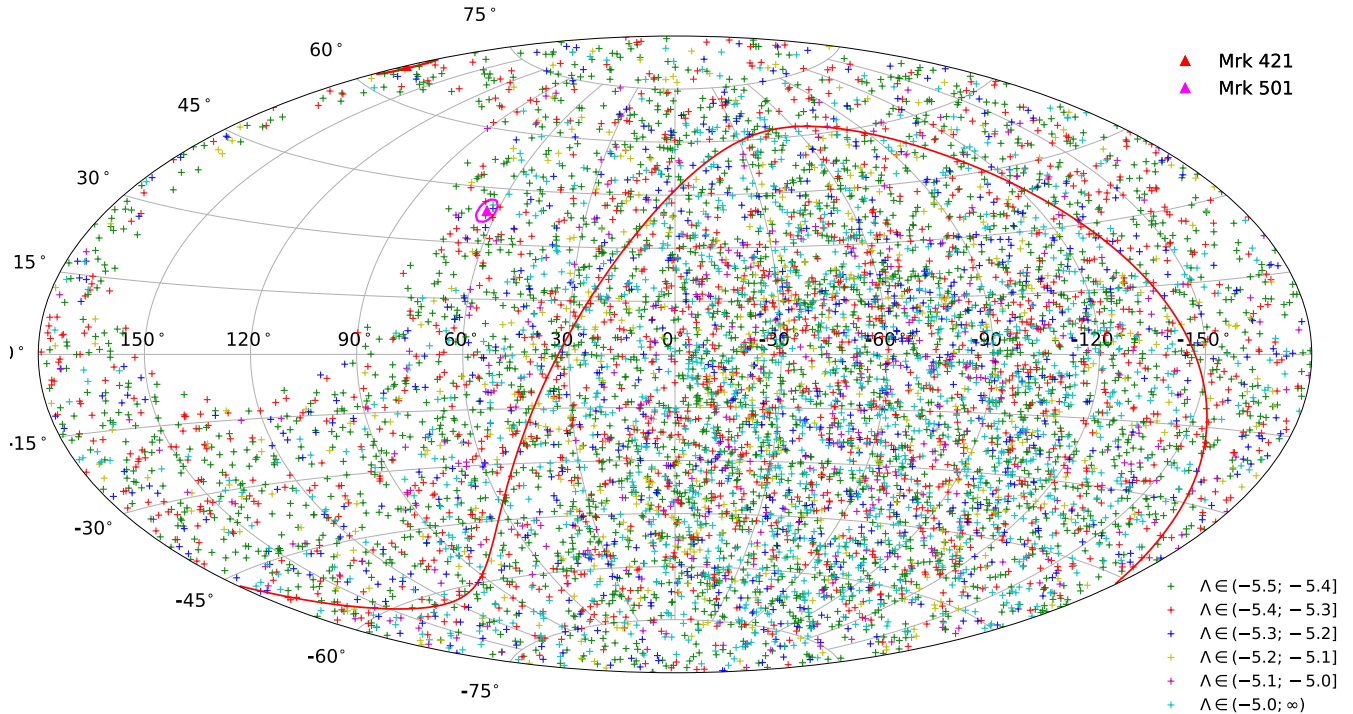


Figure 67: Sky map of the track-like events passing the selection cuts (total 7314 events selected with  $\Lambda > -5.5$ ). In galactic coordinates using Aitoff projection. The red solid curve denotes the equatorial plane. The red circles denote the 3 degree radius region around the sources.

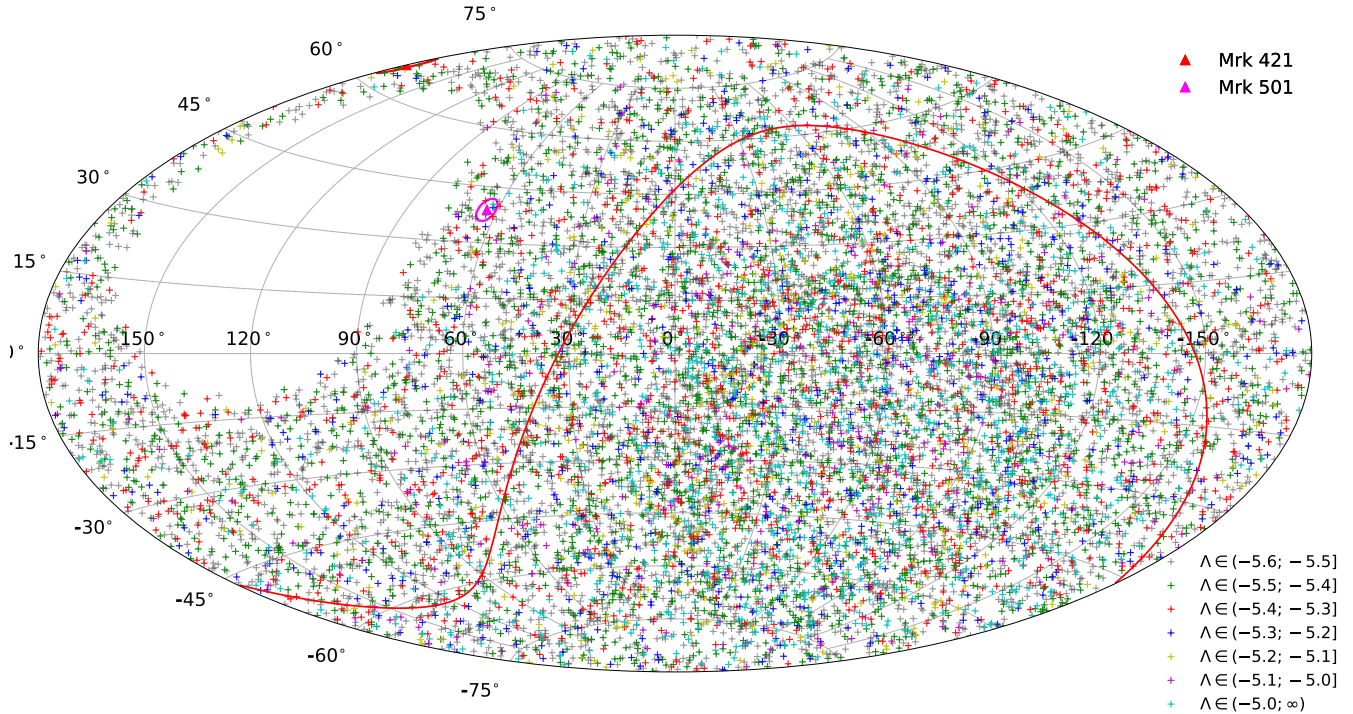


Figure 68: Sky map of the track-like events passing the selection cuts (total 12827 events selected with  $\Lambda > -5.6$ ). In galactic coordinates using Aitoff projection. The red solid curve denotes the equatorial plane. The red circles denote the 3 degree radius region around the sources.

# List of Figures

- 1 Comparison of the data with MC simulations as a function of the number of hits  $nhit$ . The figure corresponds to the energy PDF distribution after applying a cut on the quality parameter  $\Lambda > -5.3$  (the global cuts on  $\beta < 1.0^\circ$ , and  $\cos(\theta) > -0.1$  applied). The blue dots show the simulated up-going atmospheric neutrinos with the errors as a dashed area, the red dots show the mis-reconstructed atmospheric muons with the errors as a dashed are, the green line is the sum of both contributions, and the black crosses show the data. The bottom plot shows the data to MC ratio, where the number of MC events is the sum of neutrinos and atmospheric muons. . . . . 3
- 2 Comparison of the data with MC simulations as a function of the quality parameter of the reconstruction of muon track  $\Lambda$ . The figure corresponds to the event distribution after applying the global cuts on  $\beta < 1.0^\circ$ ,  $\cos(\theta) > -0.1$ , and  $\Lambda > -6.0$ . The blue dots show the simulated up-going atmospheric neutrinos with the errors as a dashed area, the red dots show the mis-reconstructed atmospheric muons with the errors as a dashed are, the green line is the sum of both contributions, and the black crosses show the data. The vertical dotted line with the arrow shows where the optimized selection cuts stand for the various tested spectra of both sources. The bottom plot shows the data to MC ratio, where the number of MC events is the sum of neutrinos and atmospheric muons. . . . . 4
- 3 Comparison of the data with MC simulations as a function of the reconstructed cosine of the zenith angle  $\cos(\theta)$ . The figure corresponds to the event distribution after applying a cut on the quality parameter  $\Lambda > -5.3$  (the global cuts on  $\beta < 1.0^\circ$ , and  $\cos(\theta) > -0.1$  applied). The blue dots show the simulated up-going atmospheric neutrinos with the errors as a dashed area, the red dots show the mis-reconstructed atmospheric muons with the errors as a dashed are, the green line is the sum of both contributions, and the black crosses show the data. The bottom plot shows the data to MC ratio, where the number of MC events is the sum of neutrinos and atmospheric muons. . . . . 5
- 4 Comparison of the data with MC simulations as a function of the estimated error on the direction of the reconstructed muon track  $\beta$ . The figure corresponds to the event distribution after applying a cut on zenith angle  $\cos(\theta) > -0.1$  and a cut on the quality parameter  $\Lambda > -5.3$  (the global cut on  $\beta < 1.0^\circ$  applied). The blue dots show the simulated up-going atmospheric neutrinos with the errors as a dashed area, the red dots show the mis-reconstructed atmospheric muons with the errors as a dashed are, the green line is the sum of both contributions, and the black crosses show the data. The bottom plot shows the data to MC ratio, where the number of MC events is the sum of neutrinos and atmospheric muons. . . . . 6
- 5 Schematic representation of our understanding of the AGN phenomenon in the unified scheme. The type of object we see depends on the viewing angle, whether or not the AGN produces a significant jet emission, and how powerful the central engine is. Note that radio loud objects are generally thought to display symmetric jet emission [3]. . . . . 7
- 6 The distinct flare states for Mrk 421 (top) and Mrk 501 (bottom) for 17 months after 1-day binning applied to the light curve data from [1] (in blue and green); the blue dotted lines represent the average fluxes,  $\sim 0.8$  CU and  $\sim 0.3$  CU respectively; the green dotted lines represent the peaks selection criteria can be applied: *average flux*, *average flux + 1 $\sigma$* , *average flux + 2 $\sigma$* . The left axes represent the units of the fluxes, the right-right axis represent the fluxes in corresponding Crab Units (CU). The right-left axes represent the units of fluences shown as shaded grey areas. . . . . 9

7	The distinct flare states for Mrk 421 (top) and Mrk 501 (bottom) for 17 months after 1-day binning applied to the light curve data from [1]. The shaded red area represent OFF days. The left axes represent the units of the fluxes, the right-right axis represent the fluxes in corresponding Crab Units (CU). The right-left axes represent the units of fluences shown as shaded grey areas. . . . .	10
8	ANTARES visibility of the sky ranging from 0 (white) to 100% (dark blue) with 10% step. <i>Left panel:</i> Up-going with slightly down-going (angle above the horizon below $5.74^\circ$ ) for $\cos(\theta) > -0.1$ ; <i>Right panel:</i> Only Up-going $\cos(\theta) > 0$ . . . . .	11
9	<i>Upper panel:</i> Visibility curves as a function of the declination for cuts on zenith angle used in the analysis $\cos(\theta) > 0.0$ , $\cos(\theta) > -0.1$ , $\cos(\theta) > -0.2$ (colored solid lines) and for possible extension up to $\cos(\theta) > -0.5$ (grey color dotted, dashed and solid lines respectively). <i>Lower panel:</i> Visibility ratio curves as a function of the declination with respect to $\cos(\theta) > 0.0$ . The vertical color lines represent the declination of Mrk 421 (orange) and Mrk 501 (yellow). . . . .	12
10	Elevation of the sources (in degrees). The green and blue dotted lines represent the improvement in the visibility for the $\cos(\theta) > -0.1$ and $\cos(\theta) > -0.2$ cuts and corresponds to $5.74^\circ$ and $11.54^\circ$ elevation levels respectively. . . . .	12
11	Definition of the power and p-value significance of the test statistic. The distributions of the test statistic, TS, for the background-only ( $H_0$ ) and signal plus background ( $H_1$ ) hypotheses are shown. The test statistic required for $H_0$ rejection is shown as a dotted line. Corresponding p-value significance and the power to discriminate $H_0$ from $H_1$ are shown as a dark-shaded and light-shaded areas respectively. . . . .	15
12	<i>Left panel:</i> The optical depth $\tau(z, E_\gamma)$ versus energy of $\gamma$ -ray photons for Mrk 421 and Mrk 501. <i>Right panel:</i> The attenuation $e^{-\tau(z, E_\gamma)}$ of $\gamma$ -rays versus energy for sources. The red and blue color lines represent results from [12] for Mrk 421 at redshift $z=0.031$ and Mrk 501 at redshift $z=0.034$ respectively. Dashed green color region represent results from [14], the range is between $z=0.025$ and $z=0.040$ of which the data table is available. Violet line represent results from [13] at $z=0.030$ of which the data table is available. . . . .	18
13	The normalized to unity ANTARES background time distribution of selected period made for quality parameter $\Lambda > -5.6$ , reconstructed zenith $\cos(\theta) > -0.1$ , and an estimated angular uncertainty on the fitted muon track direction $\beta < 1.0^\circ$ with number of hits in PMTs $n_{hit} > 5$ in more than one line $N_{line} > 1$ . The size of the bin is 1 day. . . . .	19
14	Background time PDF of selected period for several $\Lambda$ values with $\cos(\theta) > -0.1$ , $\beta < 1.0^\circ$ , $n_{hit} > 5$ , $N_{line} > 1$ conditions applied. . . . .	19
15	<i>Upper left panel:</i> The mean value and the errors of distributions of bkg time PDF ratios of $\Lambda > X_i / \Lambda > X_{ref}$ for $X_i = -6.0, -5.8, -5.6, -5.2, -5.0, -4.8$ with the reference to $\Lambda_{ref} > -5.4$ . The pink color line represent the linear fit. <i>Upper right panel and Lower panel:</i> Example of distributions of normalized bkg time PDF ratios $\Lambda > X_i / \Lambda > X_{ref}$ for $X_i = -5.8, -5.6, -5.0$ with the reference to $\Lambda_{ref} > -5.4$ . . . . .	20
16	The distinct flare states for Mrk 421 vs threshold. The blue dotted line represent the average fluxes $\sim 0.8$ CU; the green dotted lines represent the peak selection thresholds: <i>average flux</i> , <i>average flux + 1<math>\sigma</math></i> , <i>average flux + 2<math>\sigma</math></i> . The bottommost plot shows the long case, the three upper plots show short case for <i>average flux</i> , <i>average flux + 1<math>\sigma</math></i> , <i>average flux + 2<math>\sigma</math></i> respectively. The left axes represent the units of the fluxes, the right-right axis represent the fluxes in corresponding Crab Units (CU). The right-left axes represent the units of fluences shown as shaded grey areas. . . . .	22

17	The distinct flare states for Mrk 501 vs threshold. The blue dotted line represent the average fluxes $\sim 0.3$ CU; the green dotted lines represent the peak selection thresholds: <i>average flux</i> , <i>average flux + 1<math>\sigma</math></i> , <i>average flux + 2<math>\sigma</math></i> . The bottommost plot shows the long case, the three upper plots show short case for <i>average flux</i> , <i>average flux + 1<math>\sigma</math></i> , <i>average flux + 2<math>\sigma</math></i> respectively. The left axes represent the units of the fluxes, the right-right axis represent the fluxes in corresponding Crab Units (CU). The right-left axes represent the units of fluences shown as shaded grey areas.	23
18	Probability distribution of the test statistic variable issued from pseudo experiments for background-only $H_0$ (yellow area) and by adding from 1 up to 20 signal neutrinos $N_S$ around the source (red, green, blue, ... etc colors represent $N_S = 1, 3, 5, \dots$ injected signal events) for Mrk 421 with the energy spectrum $E^{-2.0}$ and cut on zenith angle $\cos(\theta) > -0.1$ for optimum lambda cut $\Lambda > -5.3$ . The mean background events $\mu_B = 5.37 \cdot 10^{-5}$ . Dotted vertical lines indicate the threshold values for the $3\sigma$ and $5\sigma$ significances for the rejection of the background-only hypothesis. The dotted horizontal line marks the point below which the lack of statistics (one over the total amount of PEXs simulated) and implies an extrapolation by an exponential fit (broad black line) to estimate $Q^{5\sigma}$ .	25
19	Discovery power at $3\sigma$ (top) and $5\sigma$ (bottom) levels for Mrk 421 with the energy spectrum $E^{-2.0}$ for optimum lambda cut $\Lambda > -5.3$ and $\cos(\theta) > -0.1$ . Blue circles represent signals selected at $3\sigma, 5\sigma$ levels in 50% of the trials.	26
20	Discovery power at $5\sigma$ level. <i>Left panel:</i> Mrk 421 <i>Right panel:</i> Mrk 501. From upper to bottom: all flares, short flares with <i>average flux</i> , <i>average flux + 1<math>\sigma</math></i> , <i>average flux + 2<math>\sigma</math></i> thresholds.	27
21	Examples of acceptance for Mrk 421 as a function of the source declination for the several $\Lambda$ cuts [with $\beta < 1.0$ and $\cos(\theta) > -0.1$ ] with a flux normalization factor of $\Phi_0 = 10^{-7} \text{ GeV}^{-1} \text{ cm}^{-2} \text{ s}^{-1}$ in $N_{ev} = A_{cc} \times \Phi_0$ magnitudes. The period used: November 26 <sup>th</sup> , 2014 - April 20 <sup>th</sup> , 2016. <i>Upper left panel:</i> $E^{-1.0} \exp(-E/1 \text{ PeV})$ . <i>Upper right panel:</i> $E^{-2.0}$ . <i>Lower panel:</i> $E^{-2.5}$ . Orange color represents the bins of the source declination.	28
22	Examples of acceptance for Mrk 501 as a function of the source declination for the several $\Lambda$ cuts [with $\beta < 1.0$ and $\cos(\theta) > -0.1$ ] with a flux normalization factor of $\Phi_0 = 10^{-7} \text{ GeV}^{-1} \text{ cm}^{-2} \text{ s}^{-1}$ in $N_{ev} = A_{cc} \times \Phi_0$ magnitudes. The period used: November 26 <sup>th</sup> , 2014 - April 20 <sup>th</sup> , 2016. <i>Upper left panel:</i> $E^{-1.0} \exp(-E/1 \text{ PeV})$ . <i>Upper right panel:</i> $E^{-2.0}$ . <i>Lower left panel:</i> $E^{-2.5}$ . <i>Lower right panel:</i> $E^{-2.25}$ . Yellow color represents the bins of the source declination.	29
23	Discovery fluxes comparison at $5\sigma$ level for Mrk 421 for several thresholds. <i>Upper left panel:</i> $E^{-1.0} \exp(-E/1 \text{ PeV})$ . <i>Upper right panel:</i> $E^{-2.0}$ . <i>Lower panel:</i> $E^{-2.5}$ . Light green color circles represent the values with $\Lambda$ that maximizes $MDP^{5\sigma}$ .	30
24	Discovery fluxes comparison at $5\sigma$ level for Mrk 501 for several thresholds. <i>Upper left panel:</i> $E^{-1.0} \exp(-E/1 \text{ PeV})$ . <i>Upper right panel:</i> $E^{-2.0}$ . <i>Lower left panel:</i> $E^{-2.5}$ . <i>Lower right panel:</i> $E^{-2.25}$ . Light green color circles represent the values with $\Lambda$ that maximizes $MDP^{5\sigma}$ .	31
25	MDP for $5\sigma$ discovery. <i>Left panel:</i> Mrk 421 <i>Right panel:</i> Mrk 501. From upper to bottom: all flares, short flares with <i>average flux</i> , <i>average flux + 1<math>\sigma</math></i> , <i>average flux + 2<math>\sigma</math></i> thresholds.. Light green color circles represent the maximum MDP values.	34

26	Sensitivity fluxes comparison for Mrk 421 for several thresholds. <i>Upper left panel:</i> $E^{-1.0} \exp(-E/1\text{PeV})$ . <i>Upper right panel:</i> $E^{-2.0}$ . <i>Lower panel:</i> $E^{-2.5}$ . Light green color circles represent the values with $\Lambda$ that maximizes $\text{MDP}^{5\sigma}$ .	35
27	Sensitivity fluxes comparison for Mrk 501 for several thresholds. <i>Upper left panel:</i> $E^{-1.0} \exp(-E/1\text{PeV})$ . <i>Upper right panel:</i> $E^{-2.0}$ . <i>Lower left panel:</i> $E^{-2.5}$ . <i>Lower right panel:</i> $E^{-2.25}$ . Light green color circles represent the values with $\Lambda$ that maximizes $\text{MDP}^{5\sigma}$ .	36
28	Distribution of the MC neutrinos $\nu_\mu + \bar{\nu}_\mu$ for each spectrum and source for the optimum $\Lambda$ cuts (with the optimum $\cos(\theta) > -0.1$ and $\beta < 1.0$ considered) obtained for the long case. The dotted vertical lines represent the corresponding 5% and 95% energy limits.	38
29	Neutrino energy flux sensitivities at 90% C.L. obtained in the analysis with $E^{-1.0} \exp(-E/1\text{PeV})$ , $E^{-2.0}$ , $E^{-2.5}$ , $E^{-2.25}$ (this for Mrk 501 only) neutrino energy spectra. Obtained for the long case with sensitivity fluxes for optimum $\Lambda$ values for each spectrum.	39
30	Neutrino fluence sensitivities for long case at 90% C.L. obtained in the analysis with $E^{-1.0} \exp(-E/1\text{PeV})$ , $E^{-2.0}$ , $E^{-2.5}$ , $E^{-2.25}$ (this for Mrk 501 only) neutrino energy spectra. Obtained for the long case with sensitivity fluxes for optimum $\Lambda$ values for each spectrum.	39
31	Neutrino fluence sensitivities at 90% C.L. vs $\Lambda$ for Mrk 421 for different peak selection thresholds. <i>Upper left panel:</i> $E^{-1.0} \exp(-E/1\text{PeV})$ . <i>Upper right panel:</i> $E^{-2.0}$ . <i>Lower panel:</i> $E^{-2.5}$ . Light green color circles represent the sensitivities derived with $DF^{90\%CL}$ of optimum $\Lambda$ values.	40
32	Neutrino fluence sensitivities at 90% C.L. vs $\Lambda$ for Mrk 501 for different peak selection thresholds. <i>Upper left panel:</i> $E^{-1.0} \exp(-E/1\text{PeV})$ . <i>Upper right panel:</i> $E^{-2.0}$ . <i>Lower left panel:</i> $E^{-2.5}$ . <i>Lower right panel:</i> $E^{-2.25}$ . Light green color circles represent the sensitivities derived with $DF^{90\%CL}$ of optimum $\Lambda$ values.	41
33	Bayesian blocks vs $\text{ncp}_{\text{prior}}$ . <i>Upper plot:</i> Mrk 421. <i>Lower plot:</i> Mrk 501. The 1026 and 1034 blocks for $\text{ncp}_{\text{prior}} = 0$ are the total number of data points (or days of search) available for Mrk 421 and Mrk 501 respectively.	44
34	The HAWC daily flux light curve for Mrk 421 for 1026 transits between November 27 <sup>th</sup> , 2014 and January 1 <sup>st</sup> , 2018. The orange lines show the distinct flux states between change points identified via the Bayesian blocks analysis with a 5% false positive probability and $\text{ncp}_{\text{prior}} = 6$ . The orange shaded regions represent the statistical uncertainty of $1\sigma$ of the flux amplitudes for the periods between two change points. The bottom plot shows the distinct flux states in a separate plot.	45
35	The HAWC daily flux light curve for Mrk 501 for 1034 transits between November 28 <sup>th</sup> , 2014 and January 1 <sup>st</sup> , 2018. The orange lines show the distinct flux states between change points identified via the Bayesian blocks analysis with a 5% false positive probability and $\text{ncp}_{\text{prior}} = 6$ . The orange shaded regions represent the statistical uncertainty of $1\sigma$ of the flux amplitudes for the periods between two change points. The bottom plot shows the distinct flux states in a separate plot.	46
36	Obtained distinct flare states for Mrk 421 vs threshold. <i>Upper plot</i> The long case. <i>Lower plot</i> The short case for <i>average flux + 2<math>\sigma</math></i> . The blue dotted line represents the average flux; the green dotted line represents the <i>average flux + 2<math>\sigma</math></i> peak selection threshold. The left axis represents the units of the flux, the right axis represents the units of the fluences shown as shaded grey areas. The red line represents the edge of the period of interests in the analysis based on HAWC 17 months search [1].	47

37	Obtained distinct flare states for Mrk 501 vs threshold. <i>Upper plot</i> The long case. <i>Lower plot</i> The short case for <i>average flux + 2<math>\sigma</math></i> . The blue dotted line represents the average flux; the green dotted line represents the <i>average flux + 2<math>\sigma</math></i> peak selection threshold. The left axis represents the units of the flux, the right axis represents the units of the fluences shown as shaded grey areas. The red line represents the edge of the period of interests in the analysis based on HAWC 17 months search [1]. . . . .	48
38	Comparison of the data with MC simulations as a function of the number of hits nhit. The figure corresponds to the energy PDF distribution after applying the cut on the quality parameter $\Lambda > -5.4$ . The blue dots show the simulated up-going atmospheric neutrinos with the errors as a dashed area, the red dots show the mis-reconstructed atmospheric muons with the errors as a dashed area, the green line is the sum of both contributions, and the black crosses show the data. The bottom plot shows the data to MC ratio, where the number of MC events is the sum of neutrinos and atmospheric muons. . . . .	50
39	Comparison of the data with MC simulations as a function of the quality parameter of the reconstruction of muon track $\Lambda$ . The figure corresponds to the event distribution after applying the cut on the reconstructed cosine of the zenith angle $\cos(\theta) > -0.1$ and the cut on the error on the direction of the reconstructed muon track $\beta < 1.0^\circ$ . The blue dots show the simulated up-going atmospheric neutrinos with the errors as a dashed area, the red dots show the mis-reconstructed atmospheric muons with the errors as a dashed area, the green line is the sum of both contributions, and the black crosses show the data. The vertical dotted line with the arrow shows where the optimized selection cuts stand for the various tested spectra of both sources. The bottom plot shows the data to MC ratio, where the number of MC events is the sum of neutrinos and atmospheric muons. . . . .	51
40	Comparison of the data with MC simulations as a function of the reconstructed cosine of the zenith angle $\cos(\theta)$ . The figure corresponds to the event distribution after applying the cut on the quality parameter $\Lambda > -5.4$ and the cut on the error on the direction of the reconstructed muon track $\beta < 1.0^\circ$ . The blue dots show the simulated up-going atmospheric neutrinos with the errors as a dashed area, the red dots show the mis-reconstructed atmospheric muons with the errors as a dashed area, the green line is the sum of both contributions, and the black crosses show the data. The vertical dotted line with the arrow shows the selected $\cos(\theta) > -0.1$ cut. The bottom plot shows the data to MC ratio, where the number of MC events is the sum of neutrinos and atmospheric muons. . . . .	52
41	Comparison of the data with MC simulations as a function of the estimated error on the direction of the reconstructed muon track $\beta$ . The figure corresponds to the event distribution after applying the cut on zenith angle $\cos(\theta) > -0.1$ and the cut on the quality parameter $\Lambda > -5.4$ . The blue dots show the simulated up-going atmospheric neutrinos with the errors as a dashed area, the red dots show the mis-reconstructed atmospheric muons with the errors as a dashed area, the green line is the sum of both contributions, and the black crosses show the data. The vertical dotted line with the arrow shows the selected $\beta < 1.0^\circ$ cut. The bottom plot shows the data to MC ratio, where the number of MC events is the sum of neutrinos and atmospheric muons. . . . .	53
42	Discovery power at $3\sigma$ level. <i>Left panel:</i> Mrk 421 <i>Right panel:</i> Mrk 501. <i>Upper panel</i> all flares. <i>Lower panel</i> short flares with <i>average flux + 2<math>\sigma</math></i> threshold. . . . .	55
43	Discovery power at $5\sigma$ level. <i>Left panel:</i> Mrk 421 <i>Right panel:</i> Mrk 501. <i>Upper panel</i> all flares. <i>Lower panel</i> short flares with <i>average flux + 2<math>\sigma</math></i> threshold. . . . .	55

44	Examples of acceptance for Mrk 421 as a function of the source declination for the several $\Lambda$ cuts [with $\beta < 1.0$ and $\cos(\theta) > -0.1$ ] with a flux normalization factor of $\Phi_0 = 10^{-7} \text{ GeV}^{-1} \text{ cm}^{-2} \text{ s}^{-1}$ in $N_{ev} = A_{cc} \times \Phi_0$ magnitudes. The period used: November 27 <sup>th</sup> , 2014 - January 1 <sup>st</sup> , 2018. <i>Upper left panel:</i> $E^{-1.0} \exp(-E/1\text{PeV})$ . <i>Upper right panel:</i> $E^{-2.0}$ . <i>Lower panel:</i> $E^{-2.5}$ . Orange color represents the bins of the source declination. . . . .	56
45	Examples of acceptance for Mrk 501 as a function of the source declination for the several $\Lambda$ cuts [with $\beta < 1.0$ and $\cos(\theta) > -0.1$ ] with a flux normalization factor of $\Phi_0 = 10^{-7} \text{ GeV}^{-1} \text{ cm}^{-2} \text{ s}^{-1}$ in $N_{ev} = A_{cc} \times \Phi_0$ magnitudes. The period used: November 28 <sup>th</sup> , 2014 - June 28 <sup>th</sup> , 2016. <i>Upper left panel:</i> $E^{-1.0} \exp(-E/1\text{PeV})$ . <i>Upper right panel:</i> $E^{-2.0}$ . <i>Lower left panel:</i> $E^{-2.5}$ . <i>Lower right panel:</i> $E^{-2.25}$ . Yellow color represents the bins of the source declination. . . . .	57
46	Fluxes vs $\Lambda$ for Mrk 501. <i>Upper left panel:</i> $E^{-1.0} \exp(-E/1\text{PeV})$ . <i>Upper right panel:</i> $E^{-2.0}$ . <i>Lower panel:</i> $E^{-2.5}$ . Light red color represents the values with $\Lambda$ that maximizes $\text{MDP}^{3\sigma}/\text{MDP}^{5\sigma}$ . . . . .	58
47	Fluxes vs $\Lambda$ for Mrk 501. <i>Upper left panel:</i> $E^{-1.0} \exp(-E/1\text{PeV})$ . <i>Upper right panel:</i> $E^{-2.0}$ . <i>Lower left panel:</i> $E^{-2.5}$ . <i>Lower right panel:</i> $E^{-2.25}$ . Light red color represents the values with $\Lambda$ that maximizes $\text{MDP}^{5\sigma}$ (or $\text{MDP}^{3\sigma}$ ). . . . .	59
48	MDP for Mrk 421. <i>Upper panel</i> for $3\sigma$ discovery. <i>Lower panel</i> for $5\sigma$ discovery. <i>Left panel:</i> all flares. <i>Right panel:</i> flares with <i>average flux + <math>2\sigma</math></i> threshold. Light green color circles represent the maximum MDP values. . . . .	62
49	MDP for Mrk 501. <i>Upper panel</i> for $3\sigma$ discovery. <i>Lower panel</i> for $5\sigma$ discovery. <i>Left panel:</i> all flares. <i>Right panel:</i> flares with <i>average flux + <math>2\sigma</math></i> threshold. Light green color circles represent the maximum MDP values. . . . .	63
50	Neutrino energy flux sensitivities at 90% C.L. obtained in the analysis with $E^{-1.0} \exp(-E/1\text{PeV})$ , $E^{-2.0}$ , $E^{-2.5}$ , $E^{-2.25}$ (this for Mrk 501 only) neutrino energy spectra. Obtained for the long case with sensitivity fluxes for optimum $\Lambda$ values for each spectrum. . . . .	65
51	SED of Mrk 421 and the neutrino energy flux sensitivities at 90% C.L. obtained in the analysis. Adapted from [18]. . . . .	65
52	Neutrino fluence sensitivities at 90% C.L. obtained in the analysis with $E^{-1.0} \exp(-E/1\text{PeV})$ , $E^{-2.0}$ , $E^{-2.5}$ , $E^{-2.25}$ (this for Mrk 501 only) neutrino energy spectra. Obtained for long case with sensitivity fluxes for optimum $\Lambda$ values for each spectrum. . . . .	66
53	Comparison plots for neutrino fluence sensitivities at 90% C.L. obtained in the analysis with $E^{-1.0} \exp(-E/1\text{PeV})$ , $E^{-2.0}$ , $E^{-2.5}$ , $E^{-2.25}$ (this for Mrk 501 only) neutrino energy spectra. Obtained for long case with sensitivity fluxes for optimum $\Lambda$ values for each spectrum. The HAWC 2014-2017 and HAWC 2014-2016 analyses are denoted by "new" and "old" respectively. "L" (green) and "S" (blue) denote the long case (all flares are selected) and short case (flares with <i>average flux + <math>2\sigma</math></i> threshold are selected) respectively. . . . .	66
54	Comparison plots for neutrino energy flux sensitivities at 90% C.L. for Mrk 421 ( <i>Upper panel</i> ) and Mrk 501 ( <i>Lower panel</i> ) obtained for long case. Grey color and colored curves represent HAWC 2014-2016 and HAWC 2014-2017 periods respectively. . . . .	67
55	Comparison plots for neutrino fluence sensitivities at 90% C.L. vs $\Lambda$ for Mrk 421 for different peak selection thresholds. <i>Upper left panel:</i> $E^{-1.0} \exp(-E/1\text{PeV})$ . <i>Upper right panel:</i> $E^{-2.0}$ . <i>Lower panel:</i> $E^{-2.5}$ . Grey color and colored curves represent HAWC 2014-2016 and HAWC 2014-2017 periods respectively. Light green color circles represent the sensitivities derived with $\text{DF}^{90\% \text{CL}}$ of optimum $\Lambda$ values. . . . .	68

56	Comparison plots for neutrino fluence sensitivities at 90% C.L. vs $\Lambda$ for Mrk 501 for different peak selection thresholds. <i>Upper left panel:</i> $E^{-1.0} \exp(-E/1\text{PeV})$ . <i>Upper right panel:</i> $E^{-2.0}$ . <i>Lower left panel:</i> $E^{-2.5}$ . <i>Lower right panel:</i> $E^{-2.25}$ . Grey color and colored curves represent HAWC 2014-2016 and HAWC 2014-2017 periods respectively. Light green color circles represent the sensitivities derived with DF <sup>90%CL</sup> of optimum $\Lambda$ values.	69
57	Discovery power at $3\sigma$ level. <i>Left panel:</i> Mrk 421 <i>Right panel:</i> Mrk 501. From upper to bottom: all flares, short flares with <i>average flux</i> , <i>average flux + 1<math>\sigma</math></i> , <i>average flux + 2<math>\sigma</math></i> thresholds.	72
58	Discovery fluxes comparison at $3\sigma$ level for Mrk 421 for several thresholds. <i>Upper left panel:</i> $E^{-1.0} \exp(-E/1\text{PeV})$ . <i>Upper right panel:</i> $E^{-2.0}$ . <i>Lower panel:</i> $E^{-2.5}$ . Light green color circles represent the values with $\Lambda$ that maximizes MDP <sup><math>3\sigma</math></sup> .	73
59	Discovery fluxes comparison at $3\sigma$ level for Mrk 501 for several thresholds. <i>Upper left panel:</i> $E^{-1.0} \exp(-E/1\text{PeV})$ . <i>Upper right panel:</i> $E^{-2.0}$ . <i>Lower left panel:</i> $E^{-2.5}$ . <i>Lower right panel:</i> $E^{-2.25}$ . Light green color circles represent the values with $\Lambda$ that maximizes MDP <sup><math>3\sigma</math></sup> .	74
60	MDP for $3\sigma$ evidence. <i>Left panel:</i> Mrk 421 <i>Right panel:</i> Mrk 501. From upper to bottom: all flares, short flares with <i>average flux</i> , <i>average flux + 1<math>\sigma</math></i> , <i>average flux + 2<math>\sigma</math></i> thresholds.. Light green color circles represent the maximum MDP values.	75
61	The track-like events passing the selection cuts.	76
62	Sky map of the track-like events passing the selection cuts (total 1358 events selected with $\Lambda > -5.0$ ). In galactic coordinates using Aitoff projection. The red solid curve denotes the equatorial plane. The red circles denote the 3 degree radius region around the sources.	76
63	Sky map of the track-like events passing the selection cuts (total 1741 events selected with $\Lambda > -5.1$ ). In galactic coordinates using Aitoff projection. The red solid curve denotes the equatorial plane. The red circles denote the 3 degree radius region around the sources.	77
64	Sky map of the track-like events passing the selection cuts (total 2286 events selected with $\Lambda > -5.2$ ). In galactic coordinates using Aitoff projection. The red solid curve denotes the equatorial plane. The red circles denote the 3 degree radius region around the sources.	77
65	Sky map of the track-like events passing the selection cuts (total 3050 events selected with $\Lambda > -5.3$ ). In galactic coordinates using Aitoff projection. The red solid curve denotes the equatorial plane. The red circles denote the 3 degree radius region around the sources.	78
66	Sky map of the track-like events passing the selection cuts (total 4498 events selected with $\Lambda > -5.4$ ). In galactic coordinates using Aitoff projection. The red solid curve denotes the equatorial plane. The red circles denote the 3 degree radius region around the sources.	78
67	Sky map of the track-like events passing the selection cuts (total 7314 events selected with $\Lambda > -5.5$ ). In galactic coordinates using Aitoff projection. The red solid curve denotes the equatorial plane. The red circles denote the 3 degree radius region around the sources.	79
68	Sky map of the track-like events passing the selection cuts (total 12827 events selected with $\Lambda > -5.6$ ). In galactic coordinates using Aitoff projection. The red solid curve denotes the equatorial plane. The red circles denote the 3 degree radius region around the sources.	79

## List of Tables

1	Some parameters from [1]	8
2	Visibility and Ratio	11
3	Spectra and cutoff	18
4	Results on optimization for Mrk 421	32
5	Results on optimization for Mrk 501	33
6	Sensitivities at 90% C.L.	38
7	Effective livetime vs MC complete period	49
8	Results on optimization for Mrk 421	60
9	Results on optimization for Mrk 501	61
10	Sensitivities at 90% C.L.	64
11	List of OFF days	71

## References

- [1] A. Abeysekara et al. [HAWC Collaboration], "Daily monitoring of TeV gamma-ray emission from Mrk 421, Mrk 501, and the Crab Nebula with HAWC", *Astrophys.J.*, 841 (2017) no.2, 100 [DOI:10.3847/1538-4357/aa729e](https://doi.org/10.3847/1538-4357/aa729e) [[arXiv:1703.06968](https://arxiv.org/abs/1703.06968)][astro-ph.HE]
- [2] A. Albert et al. [ANTARES Collaboration], "Contributions to ICRC 2017 Part II: The multi-messenger program", PoS ICRC2017 (2017) [[arXiv:1711.01486](https://arxiv.org/abs/1711.01486)][astro-ph.HE]
- [3] V. Beckmann and C.R. Shrader. "The AGN phenomenon: open issues", PoS INTEGRAL2012 (2012) [[arXiv:1302.1397](https://arxiv.org/abs/1302.1397)][astro-ph.HE]
- [4] S. Adrian-Martinez. et al. [ANTARES Collaboration], "Search for muon-neutrino emission from GeV and TeV gamma-ray flaring blazars using five years of data of the ANTARES telescope", *JCAP* 1512 (2015) no.12, 014 [DOI:10.1088/1475-7516/2015/12/014](https://doi.org/10.1088/1475-7516/2015/12/014) [[arXiv:1506.07354](https://arxiv.org/abs/1506.07354)][astro-ph.HE]
- [5] A. Albert et al. [ANTARES Collaboration], "Time-dependent search for neutrino emission from x-ray binaries with the ANTARES telescope", *JCAP* 1704 (2017) no.04, 019 [DOI:10.1088/1475-7516/2017/04/019](https://doi.org/10.1088/1475-7516/2017/04/019) [[arXiv:1609.07372](https://arxiv.org/abs/1609.07372)][astro-ph.HE]
- [6] J. F. Beacom. "Supernova Neutrinos and the Neutrino Masses", Invited talk at the 22nd Symposium on Nuclear Physics, Oaxtepec, Morelos, Mexico, 5-8 Jan. 1999 [[arXiv:hep-ph/9901300](https://arxiv.org/abs/hep-ph/9901300)][hep-ph]
- [7] F. James and M. Roos, "Minuit - a system for function minimization and analysis of the parameter errors and correlations", *Comput.Phys.Commun.* 10 (1975) 343-367 [DOI:10.1016/0010-4655\(75\)90039-9](https://doi.org/10.1016/0010-4655(75)90039-9)
- [8] S. Adrian-Martinez. et al. [ANTARES Collaboration], "The Positioning System of the ANTARES Neutrino Telescope", *JINST* 7 (2012) T08002, [DOI:10.1088/1748-0221/7/08/T08002](https://doi.org/10.1088/1748-0221/7/08/T08002) [[arXiv:1202.3894](https://arxiv.org/abs/1202.3894)][astro-ph.IM]
- [9] A. Albert et al. [ANTARES Collaboration], "First all-flavour Neutrino Point-like Source Search with the ANTARES Neutrino Telescope", *Phys.Rev.* D96 (2017) no.8, 082001. [DOI: 10.1103/PhysRevD.96.082001](https://doi.org/10.1103/PhysRevD.96.082001) [[arXiv:1706.01857](https://arxiv.org/abs/1706.01857)][astro-ph.HE]
- [10] S. Adrian-Martinez. et al. [ANTARES Collaboration], "Search for Cosmic Neutrino Point Sources with Four Year Data of the ANTARES Telescope", *Astrophys.J.* 760 (2012) 53, [DOI:10.1088/0004-637X/760/1/53](https://doi.org/10.1088/0004-637X/760/1/53) [[arXiv:1207.3105](https://arxiv.org/abs/1207.3105)][hep-ex]
- [11] Coutiño de León, Sara et al. [HAWC Collaboration], "Spectral analysis of Markarian 421 and Markarian 501 with HAWC", PoS ICRC2017 (2017) [[arXiv:1708.04637](https://arxiv.org/abs/1708.04637)][astro-ph.HE]
- [12] A. Franceschini, G. Rodighiero and M. Vaccari, "Extragalactic optical-infrared background radiation, its time evolution and the cosmic photon-photon opacity", *AAP* 487 (Sept., 2008) 837-852 [DOI:10.1051/0004-6361:200809691](https://doi.org/10.1051/0004-6361:200809691) [[arXiv:0805.1841](https://arxiv.org/abs/0805.1841)][astro-ph]
- [13] R. C. Gilmore, R. S. Somerville, J. R. Primack and A. Domínguez, "Semi-analytic modelling of the extragalactic background light and consequences for extragalactic gamma-ray spectra", *MNRAS* 422 (June, 2012) 3189-3207 [DOI:10.1111/j.1365-2966.2012.20841.x](https://doi.org/10.1111/j.1365-2966.2012.20841.x) [[arXiv:1104.0671](https://arxiv.org/abs/1104.0671)][astro-ph.CO]

- [14] Domínguez, A., Primack, J. R., Rosario, D. J., et al. "Extragalactic Background Light Inferred from AEGIS Galaxy SED-type Fractions", MNRAS 410 (February, 2011) 2556-2578 DOI:[10.1111/j.1365-2966.2010.17631.x](https://doi.org/10.1111/j.1365-2966.2010.17631.x) [[arXiv:1007.1459](https://arxiv.org/abs/1007.1459)][astro-ph.CO]
- [15] S. Adrian-Martinez. et al. [ANTARES Collaboration], "Search for muon neutrinos from gamma-ray bursts with the ANTARES neutrino telescope using 2008 to 2011 data", Astron.Astrophys. 559 (2013) A9 DOI:[10.1051/0004-6361/201322169](https://doi.org/10.1051/0004-6361/201322169) [[arXiv:1307.0304](https://arxiv.org/abs/1307.0304)][astro-ph.HE]
- [16] J. Neyman. "Outline of a Theory of Statistical Estimation Based on the Classical Theory of Probability", Philosophical Transactions of the Royal Society of London. Series A, Mathematical and Physical Sciences, A236 (1937) no.767, 333-380 DOI:[10.1098/rsta.1937.0005](https://doi.org/10.1098/rsta.1937.0005)
- [17] J.D. Scargle. "Studies in Astronomical Time Series Analysis. VI. Bayesian Block Representations", Astrophys.J. 764 (2013) 167 DOI:[10.1088/0004-637X/764/2/167](https://doi.org/10.1088/0004-637X/764/2/167)
- [18] A.A. Abdo, M. Ackermann, M. Ajello, et al. "Fermi-LAT Observations of Markarian 421: the Missing Piece of its Spectral Energy Distribution", Astrophys. J. 736 (2011), 131 DOI:[10.1088/0004-637X/736/2/131](https://doi.org/10.1088/0004-637X/736/2/131)